Clemson University
TigerPrints

All Dissertations Dissertations

8-2011

MODELING OF STRAIN EFFECT ON THERMAL AND ELECTRICAL TRANSPORT PROPERTIES OF SI/GE NANOCOMPOSITES AND ITS APPLICATIONS

Yaoyao Xu
Clemson University, yxu@g.clemson.edu

Follow this and additional works at: https://tigerprints.clemson.edu/all_dissertations

Part of the Nanoscience and Nanotechnology Commons

Recommended Citation
Xu, Yaoyao, "MODELING OF STRAIN EFFECT ON THERMAL AND ELECTRICAL TRANSPORT PROPERTIES OF SI/GE NANOCOMPOSITES AND ITS APPLICATIONS" (2011). *All Dissertations*. 778.
https://tigerprints.clemson.edu/all_dissertations/778

This Dissertation is brought to you for free and open access by the Dissertations at TigerPrints. It has been accepted for inclusion in All Dissertations by an authorized administrator of TigerPrints. For more information, please contact kokeefe@clemson.edu.

MODELING OF STRAIN EFFECT ON THERMAL AND ELECTRICAL TRANSPORT PROPERTIES OF SI/GE NANOCOMPOSITES AND ITS APPLICATIONS

A Thesis
Presented to
the Graduate School of
Clemson University

In Partial Fulfillment
of the Requirements for the Degree
Doctor of Philosophy
Mechanical Engineering

---

by
Yaoyao Xu
August 2011

Accepted by
Dr. Gang Li, Committee Chair
Dr. Sherrill B. Biggers
Dr. Paul F. Joseph
Dr. Lonny L. Thompson

ABSTRACT

Nanocomposites are composite materials which incorporate nanosized particles, platelets or fibers. The addition of nanosized phases into the bulk matrix can lead to significantly improved material properties compared to their macrocomposite counterparts. Due to their extraordinary properties, nanocomposites promise new applications in many fields such as ultra-high strength and ultra-light automotive parts, nonlinear optics, biomedical applications, sensors and actuators, and thermoelectric devices. The design and fabrication of nanocomposite structures, devices and systems can be accelerated by developing accurate and efficient computational tools that can describe the properties and behavior of the nanocomposites. However, the development of such tools is challenging due to the multi-scale nature of the materials. In addition, many devices where nanocomposites are employed are multi-physics systems with interactions of the mechanical, thermal and electrical energy domains. In such systems, while mechanical deformation is dependent on the temperature change, the thermal and electrical transport properties are functions of mechanical strain. In this work, we develop theoretical and computational models to address these issues and investigate the strain effect on the thermal and electrical transport properties in Si/Ge nanocomposites.

We model strain effect on the phonon thermal conductivities in the Si/Ge nanocomposite materials by combining the strain dependent lattice dynamics and the ballistic phonon Boltzmann transport equation (BTE). The Seebeck coefficient and electrical conductivity of the Si/Ge nanocomposites are calculated by using an analytical model derived from the BTE under the relaxation time approximation. The effect of strain is incorporated into the analytical model through strain induced energy shift and effective mass variation calculated from the deformation potential theory and a degenerate $\mathbf{k} \cdot \mathbf{p}$ method at the zone-boundary X point. By using the models, strain effect on the thermoelectric figure of merit is investigated for n-type Si/Ge nanocomposite materials. Our calculations reveal that in the 300-800 K temperature range, uniaxial tensile strain along $\langle 100 \rangle$ direction increases dimensionless figure of merit parallel to the tension, and biaxial tensile strain along [100] and [010] directions decreases it at low temperatures and increases it at high temperatures in the tension directions. Shear strain and compressive uniaxial and biaxial strains decrease the figure of merit. At 800 K with an electron concentration of $10^{19}/cm^3$, 1% uniaxial tensile strain can increase the figure of merit of $Si_{0.8}Ge_{0.2}$ nanocomposites by as much as 14%.

In light of nanocomposites' high electrical to thermal conductivity ratio, we propose to use Si/Ge nanocomposite materials to improve the performance of micro thermal actuators. The high electrical to thermal conductivity ratio of Si/Ge nanocomposites is utilized to facilitate a rapid temperature change within a short distance, enabling a high temperature increase in a large region of the actuator beams. The total structural thermal expansion and consequently the actuation distance can be increased significantly. A top-down quasicontinuum multi-scale model is presented for computational analysis of the nanocomposite based thermal

actuators. Numerical results indicate that incorporating Si/Ge nanocomposites in thermal actuators can significantly increase their energy efficiency and mechanical performance. In addition, parametric studies show that the size of the nanocomposite region and atomic percentage of the material components have significant effects on the overall performance of the actuators.

ACKNOWLEDGMENTS

With great respect I would like to express my sincere gratitude to all those who made it possible for me to complete this thesis.

Foremost, I am deeply indebted to my advisor, Dr. Gang Li for his invaluable guidance, and stimulating encouragement during my Ph.D. study and research at Clemson University. He has always been diligent, responsible, supportive and considerate. He continually motivated me when I was down, closely supervised me when I struggled in my research, and was always there for me when I encountered any problem. Without his insight, thoughtfulness, motivation, enthusiasm and knowledge, this thesis would not have been possible. His methods, attitude and enthusiasm have taught me a great deal, and not only lead to the success of this thesis, but will benefit me in all aspects of my life.

I would also like to extend my true appreciation to Dr. Sherrill B. Biggers, Dr. Paul F. Joseph and Dr. Lonny L. Thompson for serving on my dissertation committee, reading my thesis and commenting on my work. It was always a great honor to be able to meet with them and discuss ideas face-to-face. Dr. Biggers provided a wealth of structural mechanics expertise and was an exceptional motivator. He was often able to guide me to find the answers to difficult new questions using the knowledge I had already acquired. This demonstrated not only that knowledge is greater than

the sum of its parts, but also that it is often useless without the proper insight and context. Dr. Joseph is a talented educator and researcher. He has always conveyed his knowledge, ideas, and insights with clarity and substance; I was highly impressed by the organization, depth, and accessibility he was able to simultaneously achieve in his Theory of Elasticity course. By demonstrating how to effectively teach, I believe he has made me a better learner and I will use what I have learned from him in all my future endeavors. Dr. Thompson has an amazing understanding of the fundamentals, applications, and complexities of the finite element method. I had a great time in his Advanced Finite Element Analysis course and I hope to one day share his intuitive and comprehensive understanding of the method itself and of applied mathematics in general. He has given me a lofty goal for which to strive.

Furthermore, I would like to thank Lin Li, Ran He, Junjie Zhu and several others for their friendship and support. I also truly appreciate Matt McNeill and David Stowe for their grammatical help on my papers and thesis. Finally, thanks to all my fellow members in Dr. Gang Li's research group, especially Hua Li for the useful discussions.

In addition, I am grateful for the financial support from Clemson University and NSF.

My special acknowledgment goes to my parents and brother for their continuous support and encouragement throughout my life. They are always there for me whenever I need them and have made it possible for me to walk through all the hard times and be who I am today. There is no way that I can thank them enough.

TABLE OF CONTENTS

Page

TITLE PAGE . . . . **i**

ABSTRACT . . . . **ii**

ACKNOWLEDGMENTS . . . . **v**

LIST OF TABLES . . . . **ix**

LIST OF FIGURES . . . . **x**

1 INTRODUCTION **1**

2 STRAIN EFFECT ANALYSIS ON PHONON THERMAL CONDUCTIVITY OF SI/GE NANOCOMPOSITES **11**

2.1 Introduction 11

2.2 Theoretical Model and Computational Procedure 14

2.3 Results and Discussion 34

2.4 Summary 58

3 STRAIN EFFECT ON ELECTRON TRANSPORT PROPERTIES AND ENERGY CONVERSION EFFICIENCY OF SI/GE NANOCOMPOSITES **60**

3.1 Introduction 60

3.2 Theory 63

3.3 Results and Discussion 80

3.4 Summary 92

4 COMPUTATIONAL ANALYSIS OF NANOCOMPOSITE BASED THERMAL ACTUATORS 95
4.1 Introduction 95
4.2 Conceptual Development 97
4.3 Computational Modeling 101
4.4 Results and Discussion 111
4.5 Summary 127

5 CONCLUSIONS 128

BIBLIOGRAPHY 131

LIST OF TABLES

Table **Page**

2.1 Room temperature thermodynamic properties of bulk Si 35

3.1 Parameters used to calculate electron transport properties for n-type Si and $Si_{1-x}Ge_x$ nanocomposites. 76

4.1 Geometry parameters used for the calculation of V-shaped and U-shaped thermal actuators. 117

LIST OF FIGURES

Figure		Page
1.1	A diagram of nanocomposite materials: (a) the nanocomposite with nanoparticles embedded in a host material. (b) The nanocomposite with nanowires embedded in a host.	2
1.2	Application of nanocomposites in automotive parts: (a) M-Van step Assist: 1st commercial launch. (b) Impala: 2nd nanocomposite application.	3
1.3	A test configuration of a multi-layered nanocomposite actuator	4
1.4	Multiple length scales in the analysis of polymer matrix nanocomposites	5
1.5	The Cassini spacecraft of NASA uses thermoelectric devices to generate power.	8
1.6	BMW's thermoelectric generators for its next-generation efficient dynamics system.	8
1.7	Thermal actuators: (a) U-shaped thermal actuator. (b) V-shaped thermal actuator. (c) Contoured V-shaped thermal actuator.	9
2.1	$Si_{0.2}Ge_{0.8}$ nanocomposite material with applied strain.	14
2.2	Theoretical model for the analysis of strain effect on the phonon thermal conductivity of Si/Ge nanocomposites.	15
2.3	Atom configuration and deformation for a diamond lattice.	19
2.4	Directional phonon intensity.	24
2.5	Unit cell of the Si/Ge nanocomposite material.	26
2.6	Spatial and angular discretization.	30
2.7	Step scheme for the facial intensity.	32
2.8	Strains considered: (1) hydrostatic compressive. (2) Hydrostatic tensile. (3) Uniaxial compressive. (4) Uniaxial tensile.	36

2.9 Dispersion relation of Si at 0 K for different strain conditions: (1) unstrained (dots are experimental data). (2) Hydrostatic compressive strain. (3) Hydrostatic tensile strain. (4) Uniaxial tensile strain. . . . 37
2.10 Strain dependent phonon density of state of Si at 300 K. 38
2.11 Strain dependent Grüneisen parameter of Si with respect to temperature. 39
2.12 Strain dependent Debye temperature of Si between 200-500 K. 40
2.13 Strain dependent bulk thermal conductivity of Si between 200-500 K. 41
2.14 Specific heat of Si between 50-1000 K. 42
2.15 Strain effect on acoustic specific heat of Si between 200-500 K. 42
2.16 Average group velocity of Si as a function of strain in one direction (L_0 is the undeformed length). 43
2.17 Strain dependent phonon mean free path of Si between 200-500 K. . . 44
2.18 Unit cells with different cross-section shapes for $Si_{0.2}Ge_{0.8}$ nanocomposites: square, circular and diamond-shaped. L_{Si} is the characteristic length of the Si nanowire. 45
2.19 Phonon thermal conductivity of $Si_{0.2}Ge_{0.8}$ nanocomposites with respect to size and temperature (square Si nanowire cross-section). 46
2.20 Heat flux profile of unstrained $Si_{0.2}Ge_{0.8}$ at 300 K (Si nanowire with 10 nm × 10 nm square cross-section). 47
2.21 Phonon thermal conductivity of $Si_{0.2}Ge_{0.8}$ under hydrostatic strain at 300 K (square Si nanowire cross-section). 48
2.22 Phonon thermal conductivity of $Si_{0.2}Ge_{0.8}$ under uniaxial strain at 300 K (square Si nanowire cross-section). 48
2.23 Content effect on phonon thermal conductivity of Si_xGe_{1-x} at 300 K (square Si nanowire cross-section). 49
2.24 Heat flux profile of unstrained $Si_{0.2}Ge_{0.8}$ at 300 K (diamond-shaped Si nanowire cross-section with the characteristic length of 10 nm). . . . 50
2.25 Heat flux profile of unstrained $Si_{0.2}Ge_{0.8}$ at 300 K (circular Si nanowire cross-section with the characteristic length of 10 nm). 50
2.26 Effective temperature distribution of unstrained $Si_{0.2}Ge_{0.8}$ at 300 K ($L_{Si} = 10nm$). From top to bottom: square cross-section, diamond-shaped cross-section and circular cross-section for Si nanowire. 51
2.27 Phonon thermal conductivity of $Si_{0.2}Ge_{0.8}$ with different cross-section shapes of Si nanowire under hydrostatic strains at 300 K. 52

2.28 Difference in phonon thermal conductivity between diamond-shaped and square cross-sections as a function of characteristic length. 53
2.29 Unit cells with square and diamond cross-section shapes of Si nanowires. 54
2.30 Phonon thermal conductivity of unstrained SiGe nanocomposites with square and diamond cross-section shapes of Si nanowire at 300 K. . . 54
2.31 Mesh of the unit cell of a porous material. 55
2.32 Heat flux and effective temperature distribution profiles of unstrained porous Ge at 300 K (square cross-section with the characteristic length of the cavity being 10 nm). 56
2.33 Phonon thermal conductivity of nano-porous Ge with respect to size and temperature. 57
2.34 Phonon thermal conductivity of nano-porous Si and Ge compared to that of Si/Ge nanocomposites at 300 K. 58

3.1 Miller indices for a cubic crystal. 65
3.2 First Brillouin zone for Si and Ge. 66
3.3 Simplified band structure change under uniaxial strain for bulk n-type Si: (a) unstrained. (b) Uniaxial $\langle 100 \rangle$ tension. (3) Uniaxial $\langle 110 \rangle$ tension. 68
3.4 Coordinate systems: ellipsoidal coordinate system (ECS), crystal coordinate system at undeformed configuration (CCSU) and crystal coordinate system at deformed configuration (CCSD). 69
3.5 Energy contour of the Si out-of-plane subbands with 1% of shear strain (solid line) and no strain (dashed line). 73
3.6 Conduction band constant energy ellipsoids along Δ for Si. 77
3.7 $Si_{1-x}Ge_x$ unit cell. 80
3.8 Temperature dependent electrical conductivity of $Si_{0.7}Ge_{0.3}$ alloy and $Si_{0.8}Ge_{0.2}$ nanocomposites. 81
3.9 Bulk electron mobility of intrinsic Si as a function of strain for stress direction along [100]. 82
3.10 Electron mobility enhancement of intrinsic Si as a function of strain for stress direction along [100]. 82
3.11 Electron mobility enhancement as a function of $\langle 100 \rangle$ tension. 83
3.12 Seebeck coefficient of Si. 84

3.13 Thermoelectric properties of $Si_{0.8}Ge_{0.2}$ under uniaxial strain when $L_{Ge} = 10nm$. 85
3.14 Thermoelectric properties of $Si_{0.8}Ge_{0.2}$ under shear strain when $L_{Ge} = 10nm$. 86
3.15 Thermoelectric properties of $Si_{0.8}Ge_{0.2}$ under biaxial strain when $L_{Ge} = 10nm$. 87
3.16 Thermoelectric properties of $Si_{0.8}Ge_{0.2}$ under uniaxial strain when $L_{Ge} = 15nm$. 88
3.17 Thermoelectric properties of $Si_{0.8}Ge_{0.2}$ under shear strain when $L_{Ge} = 15nm$. 89
3.18 Thermoelectric properties of $Si_{0.8}Ge_{0.2}$ under biaxial strain when $L_{Ge} = 15nm$. 90
3.19 Thermoelectric properties of $Si_{0.8}Ge_{0.2}$ under uniaxial strain when $L_{Ge} = 20nm$. 91
3.20 Thermoelectric properties of $Si_{0.8}Ge_{0.2}$ under shear strain when $L_{Ge} = 20nm$. 92
3.21 Thermoelectric properties of $Si_{0.8}Ge_{0.2}$ under biaxial strain when $L_{Ge} = 20nm$. 93

4.1 Si/Ge nanocomposite-based thermal actuators: (a) V-shaped actuator. (b) U-shaped actuator. (c) Si/Ge nanocomposite material. 98
4.2 Computational procedure for the electro-thermo-mechanical analysis of the thermal actuators. 110
4.3 Elastic constants of $Si_{1-x}Ge_x$. 112
4.4 Linear thermal expansion coefficient of $Si_{1-x}Ge_x$ between 300-800 K. . 112
4.5 Strain and temperature dependent phonon thermal conductivity of bulk Si between 300-800 K. 113
4.6 Strain and temperature dependent phonon thermal conductivity of $Si_{0.8}Ge_{0.2}$ nanocomposite between 300-800 K. 114
4.7 Variation of phonon thermal conductivity of $Si_{1-x}Ge_x$ nanocomposites at 300 K with respect to the atomic percentage of Ge. 114
4.8 Temperature dependent electrical conductivity of $Si_{1-x}Ge_x$ nanocomposites for different atomic percentage of Ge. 115

4.9 Temperature distribution variation of V-shaped thermal actuator with respect to the length of the nanocomposite part and the atomic percentage of Ge in $Si_{1-x}Ge_x$. 118
4.10 Tip displacement of V-shaped thermal actuator as a function of the length of the nanocomposite part and the atomic percentage of Ge in $Si_{1-x}Ge_x$. 118
4.11 Variation in temperature distribution along V-shaped thermal actuator beam with respect to the length of $Si_{0.8}Ge_{0.2}$ nanocomposite. 119
4.12 Maximum displacement of V-shaped thermal actuator for different length of $Si_{0.8}Ge_{0.2}$ nanocomposite. 120
4.13 Temperature distribution along V-shaped thermal actuator beam for different atomic percentage of Ge in $Si_{1-x}Ge_x$ ($L_c = 200\mu m$). 121
4.14 Maximum displacement of V-shaped thermal actuator for different atomic percentage of Ge in $Si_{1-x}Ge_x$. 122
4.15 Deformed and undeformed beams of V-shaped thermal actuator (deformation has been scaled up by a factor of 50). 123
4.16 Variation of the temperature distribution along the upper beam of U-shaped thermal actuator with the length of Si/Ge nanocomposite and Ge atomic percentage. 125
4.17 Maximum vertical displacement of U-shaped thermal actuator as a function of the length of Si/Ge nanocomposite for different Ge atomic percentages. 125
4.18 Deformed and undeformed beams of U-shaped thermal actuator (deformation has been scaled up by a factor of 50). 126

CHAPTER 1

INTRODUCTION

In the past decade, synthesis and processing techniques have been developed to create nanostructured materials with highly controlled material composition, structures and related physical properties [1, 2, 3, 4]. Examples of the engineered nanostructures include nanotubes, quantum dots, superlattices, thin films and nanocomposites. Nanocomposites are composite materials which incorporate nanosized particles [5] or contain fibers with at least one dimension in the nano-scale [6]. Figure 1.1 shows a diagram of the above two different nanocomposites, of which (a) is the nanocomposite with nanoparticles embedded in a host material and (b) is the nanocomposite with nanowires embedded in a host. In general, a nanocomposite can be regarded as a solid combining a bulk matrix and nano-scale phases. The phases can be nanoparticles, nanowires, nanoplatelets, fibers and etc.

The addition of nanosized phases into the bulk matrix causes the exceptionally high surface to volume ratio, leading to significantly different material properties compared to their macrocomposite counterparts, which include mechanical

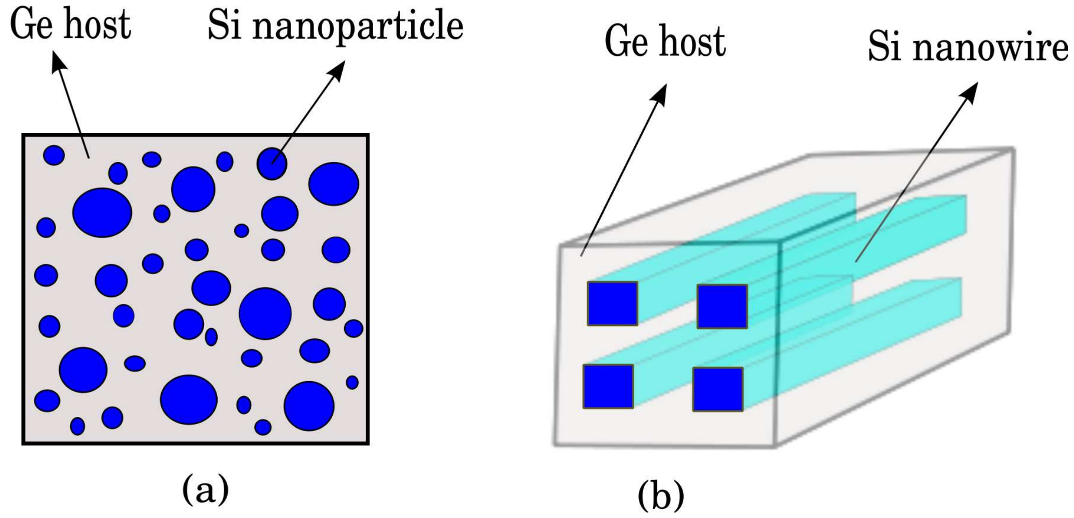

Figure 1.1: A diagram of nanocomposite materials: (a) the nanocomposite with nanoparticles embedded in a host material. (b) The nanocomposite with nanowires embedded in a host.

strength [7, 8], toughness, optical properties, electrical conductivity and thermal conductivity [9]. For example, Haque et al. showed that by dispersing 1% by weight nanosilicates, S2-glass/epoxy-clay nanocomposites exhibit about 44%, 24% and 23% improvement in interlaminar shear strength, flexural strength and fracture toughness, respectively, in comparison to conventional S2-glass/epoxy composites. These improvements of mechanical properties are attributed to increased interfacial surface areas, improved bond characteristics and intercalated/exfoliated morphology of the epoxyclay nanocomposites [10]. Kim and Jeong discovered that polylactide/exfoliated graphite nanocomposites had enhanced thermal stability, mechanical modulus, and electrical conductivity compared to microsized polylactide/natural graphite [11]. Poudel et al. measured a p-type nanocrystalline bismuth antimony telluride bulk alloy and found that it had a significantly lower thermal conductivity than the state of the art p-type BiSbTe alloy ingot due to increased phonon scattering by grain boundaries and defects [12].

Figure 1.2: Application of nanocomposites in automotive parts [13]: (a) M-Van step Assist: 1st commercial launch. (b) Impala: 2nd nanocomposite application.

Because of these extraordinary properties, nanocomposites promise new applications in many fields such as ultra-high strength and ultra-light automotive parts [13], nonlinear optics, biomedical applications [14, 15], sensors and actuators [16], and thermoelectric devices [17]. For example, Figure 1.2 shows an application of nanocomposites in the construction of high-strength lightweight automotive parts [13]. Figure 1.3 illustrates a schematic test configuration of a multi-layered nanocomposite electrochemical actuator [18]. The ply actuator uses a carbon nanotube epoxy composite material to enhance the elastic modulus and strength of the actuator structure.

The design and fabrication of nanocomposite structures, devices and systems can be accelerated by developing accurate and efficient computational tools. Such design and analysis tools require theoretical and computational models that can describe the properties and behavior of the nanocomposite materials. However, there are two major challenges in the modeling and simulation of nanocomposites.

First, nanocomposites are inherently multi-scale systems. Figure 1.4 shows the

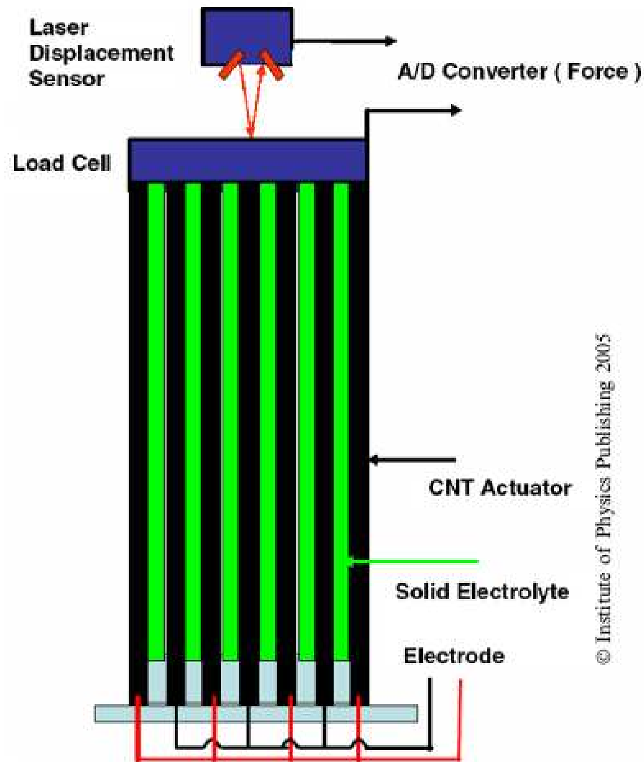

Figure 1.3: A test configuration of a multi-layered nanocomposite actuator [18].

hierarchy of key length scales in a polymer matrix nanocomposite [19]. Due to the small size of the nanoparticles (a few to tens of nanometers), nano-scale effects, such as size effects, material defects, surface effects and carrier transport scattering effects become significant. Classical theories based on continuum assumptions may not be directly applicable. On the other hand, although the characteristic length of the nanoparticles is on the order of nanometers, the entire structure could still be on the order of micrometers or larger and contain a huge number of atoms, as shown in Fig. 1.4. In this case, molecular dynamics and ab initio calculations, which can be employed for accurate analysis of systems comprising of several hundreds of atoms, are computationally impractical for real nanocomposites.

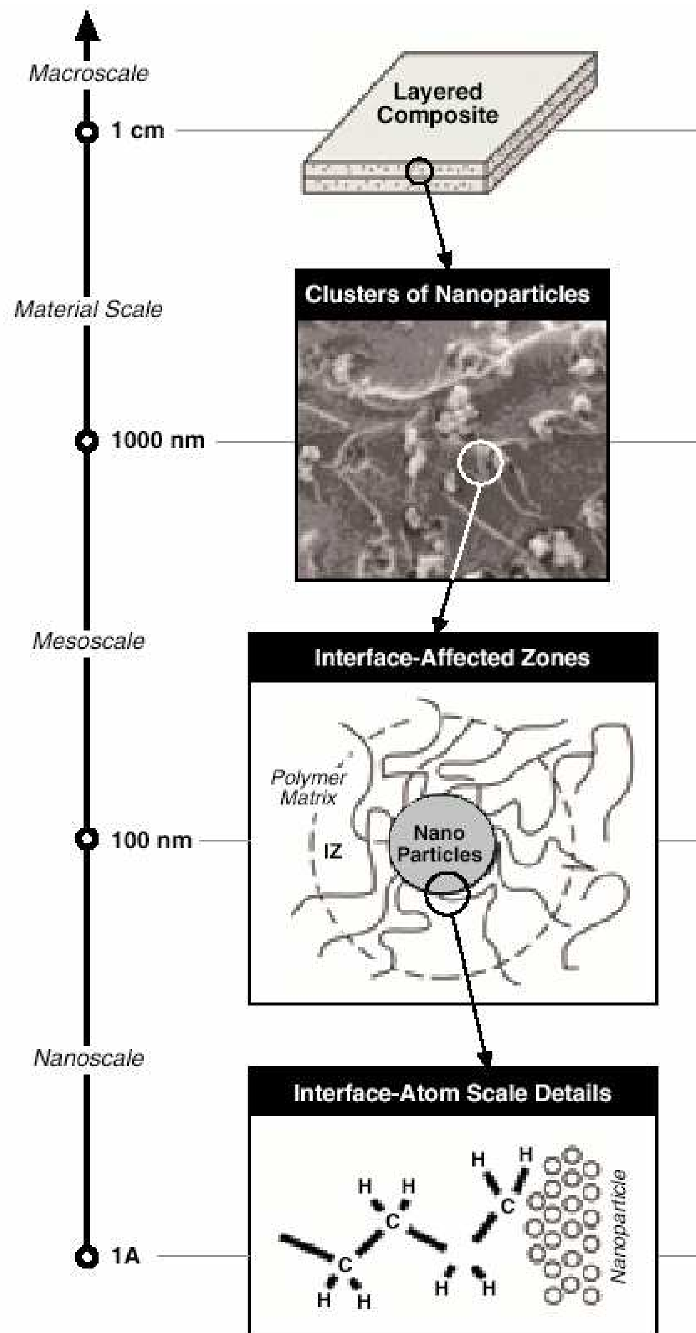

Figure 1.4: Multiple length scales in the analysis of polymer matrix nanocomposites [19].

Second, many devices where nanocomposites can be employed are multi-physics systems with interactions of the mechanical, thermal and electrical energy domains. Taking thermal actuators as an example: actuator beams are heated by electric current causing a thermal expansion induced mechanical deformation. While the mechanical deformation is dependent on the temperature change, the beam's thermal conductivity and electrical conductivity are both functions of mechanical strain and the temperature. Design and analysis of such multi-physics nanocomposite material systems requires theoretical and computational models that can describe the interactions between these different energy domains.

The objectives of this research are to: (1) model strain effect on thermal and electrical transport properties in Si/Ge nanocomposite materials; (2) study strain effect on the performance of Si/Ge nanocomposite materials, devices and systems (in particular, Si/Ge nanocomposite thermoelectric materials); (3) perform computational analysis and design of nanocomposite based multi-physics devices and systems (in particular, nanocomposite-based thermal actuators). The research work can be divided as the following four parts.

1. Modeling phonon thermal transport in Si/Ge nanocomposites under deformation. In this part, we present a model that combines lattice dynamics and the phonon Boltzmann transport equation to analyze strain effect on the cross-plane phonon thermal conductivity of Si wire-Ge host nanocomposites. For a given strain condition, mechanical strain is translated to crystal lattice deformation by using the Cauchy-Born rule. Strain dependent phonon thermal properties of Si and Ge obtained from lattice dynamics with Tersoff empirical interatomic potential are then incorporated into the BTE, in which ballistic transport within one material and diffuse scattering between Si-Ge interface

are employed. The strain dependent BTE is solved numerically on an unstructured triangular mesh by using a finite volume method. Nanocomposites with different Si nanowire cross-sections are also investigated.

2. Modeling electrical transport properties in Si/Ge nanocomposites under deformation. We again utilize the Cauchy-Born rule to calculate the variation of the electronic band structure on deformed crystal lattices. The energy shift and effective masses variation can be obtained as functions of externally applied strains by the deformation potential theory and a degenerate $\mathbf{k} \cdot \mathbf{p}$ method at the zone-boundary X point. By using the obtained energy gap and effective masses, the electrical conductivity and Seebeck coefficient can be calculated from an analytical formula based on the BTE under relaxation time approximation. For doped bulk Si and Ge, ionized impurity and phonon deformation potential scatterings have been included in the model. For Si/Ge nanocomposites, in addition to ionized impurity and phonon deformation potential scatterings, grain boundary scattering (interface scattering) is also included. Matthiessen's rule is used to obtain the total relaxation time accounting for all the scattering mechanisms.

3. Investigating the strain effect on the performance of nanocomposite thermoelectric materials and devices based on previous results. Thermoelectric materials and devices have promising applications in power generation, cooling systems and waste heat recovery [22, 23, 24, 25, 26]. For example, as shown in Fig. 1.5, the Cassini spacecraft of NASA carries 12 instruments powered by three radioisotope thermoelectric generators and has run successfully for more than 10 years. BMW tried to make use of wasted heat from cars to generate electrical energy, as shown in Fig. 1.6. The efficiency of thermoelectric devices

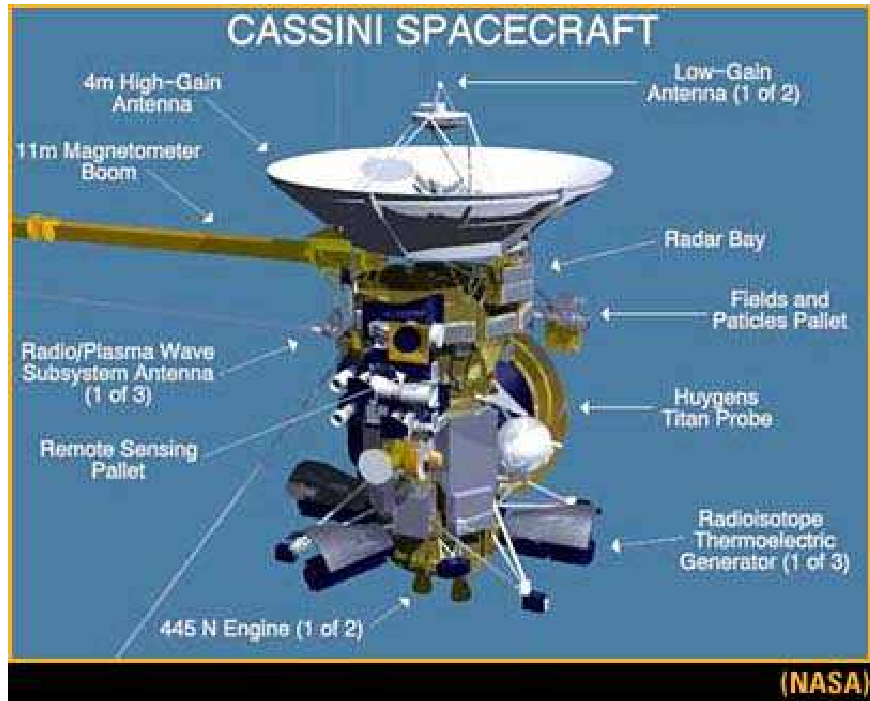

Figure 1.5: The Cassini spacecraft of NASA uses thermoelectric devices to generate power [20].

Figure 1.6: BMW's thermoelectric generators for its next-generation efficient dynamics system [21].

are determined by the dimensionless figure of merit $ZT = S^2\sigma T/k_t$, where T is the temperature, S is the Seebeck coefficient, σ is the electrical conductivity, $S^2\sigma$ is called power factor and k_t is the thermal conductivity, which includes the contribution of phonon thermal conductivity k_p and electron thermal conductivity k_e [27]. Increasing ZT is the key but challenging point in thermoelectrics research [28]. It has been shown recently that the phonon thermal conductivity can be reduced significantly in nanocomposites due to the increase of phonon interface scattering, while the electron performance can be maintained or improved [29, 30]. Significant increases in ZT values with nanocomposites have been reported [31, 32]. In this part, we study the influence of uniaxial strain, biaxial strain and shear strain on ZT of nanocomposite thermoelectric materials.

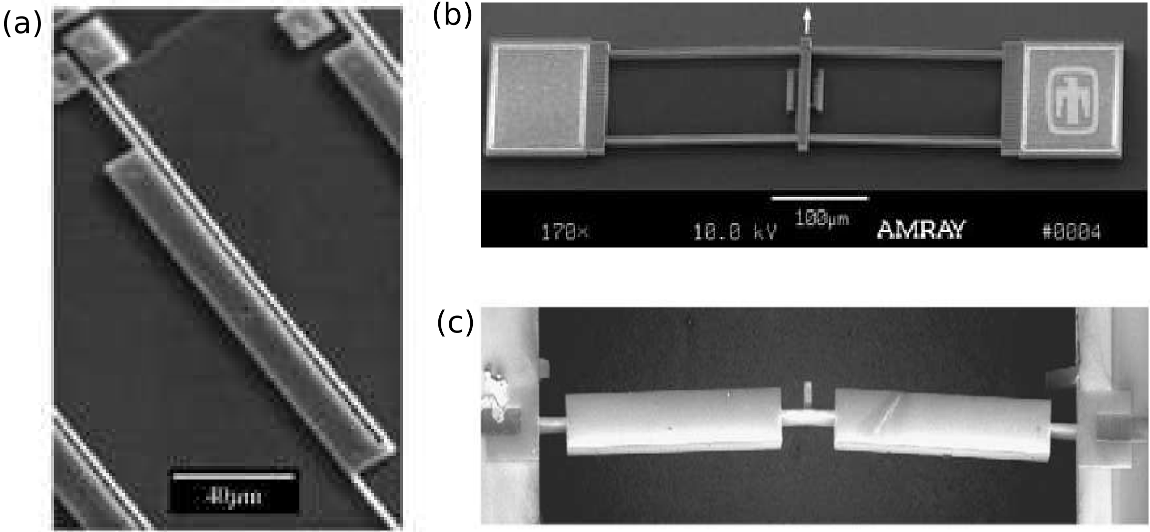

Figure 1.7: Thermal actuators: (a) U-shaped thermal actuator [33]. (b) V-shaped thermal actuator [34]. (c) Contoured V-shaped thermal actuator [35].

4. In this part, we propose to use Si/Ge nanocomposite materials to improve the performance of micro thermal actuators (TAs) as shown in Fig. 1.7. We show that nanocomposites with a high electrical to thermal conductivity ratio can facilitate a rapid temperature change within a short distance, enabling a high temperature increase in a large region of the actuator beams. The total structural thermal expansion and consequently the actuation distance can be increased significantly. Combining the above multi-scale model for computing the thermal conductivity of nanocomposites, the analytical model for calculating the electrical conductivity of the material and the continuum theory of thermomechanics, we perform computational analysis of this multi-physics system.

The rest of this thesis is organized as follows: strain effect on the phonon thermal conductivity of Si/Ge nanocomposites is investigated in Chap. 2. Chapter 3 discusses the model studying strain effect on electron transport properties of nanocomposites and explores strain effect on the figure of merit of nanocomposite thermoelectric materials based on the above models. Chapter 4 describes the computational analysis of nanocomposite-based thermal actuators. Chapter 5 summaries the whole work.

CHAPTER 2

STRAIN EFFECT ANALYSIS ON PHONON THERMAL CONDUCTIVITY OF SI/GE NANOCOMPOSITES

2.1 Introduction

Thermal conductivity measures a material's ability to conduct heat. In macro and micro-scale, thermal conductivity is usually used in Fourier's Law to describe heat conduction. However, nano-scale heat transfer may differ significantly from that in macro and micro-scales. Mean free path and wavelength of heat carriers (electrons, photons, phonons, and molecules) are usually on the order of tens or hundreds of nano-meters. In nano-scale devices or structures, their characteristic length scales are comparable to mean free path of heat carriers. Size effects become important and

the classical Fourier law is no longer valid to predict the heat conduction process or the effective thermal conductivity of nano-scale structures. In metals, freely moving electrons are the main carrier for heat energy. However, in non-metals such as Si and Ge, elastic vibrations of the lattice (phonons) play a major role in heat transfer process.

Recently various models, such as molecular dynamics (MD), Monte Carlo (MC) method, analytical formula and BTE, have been proposed to predict the phonon thermal conductivity of nanocomposites [36, 9, 37, 38]. It has been shown that the phonon thermal conductivity can be reduced significantly in nanocomposites due to the increased phonon interface scattering [29, 30]. A few other applications utilizing nanocomposites to enhance thermal conductivity have been reported, such as packaging materials of microelectronic circuits and chips [39] and conducting polymer nanocomposites [40]. While the size and volume fraction effects on the thermal conductivity of nanocomposites have been extensively investigated using computational analysis techniques, strain effect which falls in a broader category of mechanical effects, has not attracted much attention in the design of nanocomposite materials. Computational analysis of strain effect on the phonon thermal conductivity could introduce additional dimensions to the design space of nanocomposites for various applications.

Thermal conductivity of doped semiconductors under uniaxial stress at low temperatures is relatively well understood [41, 42, 43, 44]. Recently, residual strain in nanocomposite materials has been studied by several groups. Borca-Tasciuc et al. measured thermal conductivity in the cross-plane direction of symmetrically strained Si/Ge superlattices [45]. Abramson et al. studied interfacial strain on phonon transport and thermal conductivity of heterostructures around Debye

temperature by MD study [36]. Picu et al. have also employed MD to study the residual strain effect on heat transport in nanostructures by using a Lennard-Jones solid at low temperatures and concluded that tensile (or compressive) strain led to a reduction (or enhancement) of the lattice thermal conductivity [46]. While these studies have shown the significance of strain on the nano-scale thermal transport, they are limited to single crystal materials or the residual strain effect at the interface of two different materials. Thermal conductivity variation of nanocomposite materials due to externally applied mechanical strain has not been studied. In addition, either analytical or pure atomistic methods such as MD were employed in previous studies of strain effect. In strained nanocomposites, it is difficult to study the strain effect by using analytical approaches due to multiple material phases and complex geometry of the inclusion phase. Although lattice strain can be accommodated in MD calculations, the size of the system is limited due to the computational cost. For nanocomposites with characteristic length larger than a few nanometers, MD simulations would become very inefficient. Another nano-scale thermal transport analysis approach is based on the BTE [47]. This approach provides greater computational flexibility and efficiency. It has been successfully applied to compute the effective thermal conductivity of complex materials including nanocomposites [9]. However, this approach does not include mechanical variables such as strain in the model.

In this chapter, we present an approach that enables the calculation of thermal conductivity of strained nanocomposite materials. The main idea is combining the lattice dynamics for phonon dispersion change (i.e. wave effects) due to strain with the BTE for interface scattering of phonons (i.e. particle effects). Several strain dependent phonon scattering properties of the materials are used to link the lattice

dynamics and the BTE. In this approach, there is no fitting parameter in the calculation. In addition, the finite volume solution of BTE over unstructured meshes allows thermal transport analysis of nanocomposites with complex geometries. In this work, we focus on the calculation of the cross-plane thermal conductivity of a $Si_{0.2}Ge_{0.8}$ composite with Si wires embedded in Ge host under tensile and compressive hydrostatic and uniaxial strain conditions, as depicted in Fig. 2.1. For comparison, the thermal conductivity variation of Si/Ge composites corresponding to square, circular and diamond-shaped Si wire cross-sections is also calculated.

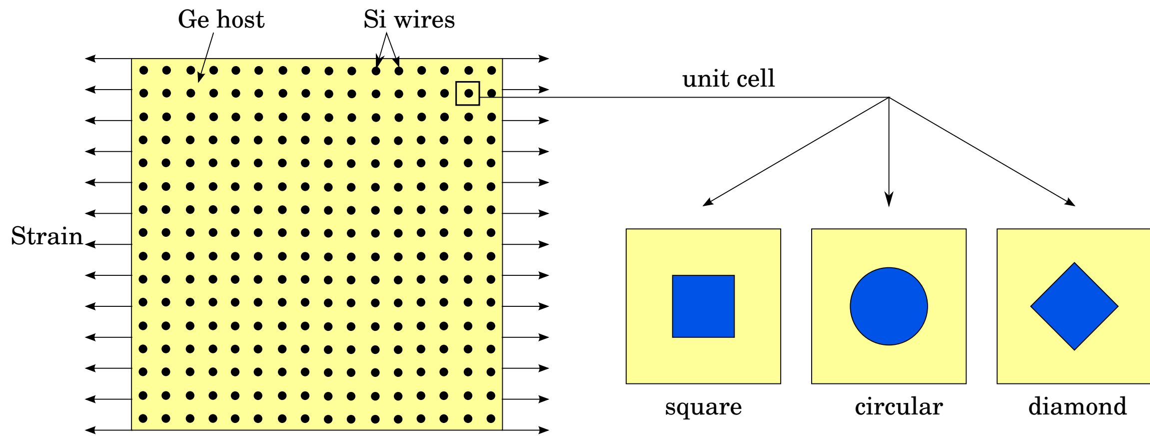

Figure 2.1: $Si_{0.2}Ge_{0.8}$ nanocomposite material with applied strain.

2.2 Theoretical Model and Computational Procedure

Figure 2.2 illustrates the theoretical model of the analysis. In this approach, atomic interactions are described by using interatomic potentials. Mechanical strains are translated to crystal lattice deformation by applying the Cauchy-Born

rule. For the deformed crystal lattice, we employ the lattice dynamics theory to compute the strain dependent phonon scattering properties for both Si and Ge, including the group velocity, specific heat and phonon mean free path. The strain dependent phonon scattering properties are then incorporated into the BTE to describe the thermal transport with interface scattering in the strained nanocomposites. Along with the BTE, a diffuse mismatch model is adopted for the Si-Ge interface. In the numerical solution of BTE, a unit cell of the nanocomposite material is taken as the computational domain with a periodic boundary condition. The unit cell is discretized into unstructured triangular volumes. The BTE is solved over the unstructured mesh by using a finite volume formulation. Heat flux and effective temperature are calculated for the volumes and faces from the intensity solution of the BTE. The strain dependent effective thermal conductivity can then be obtained.

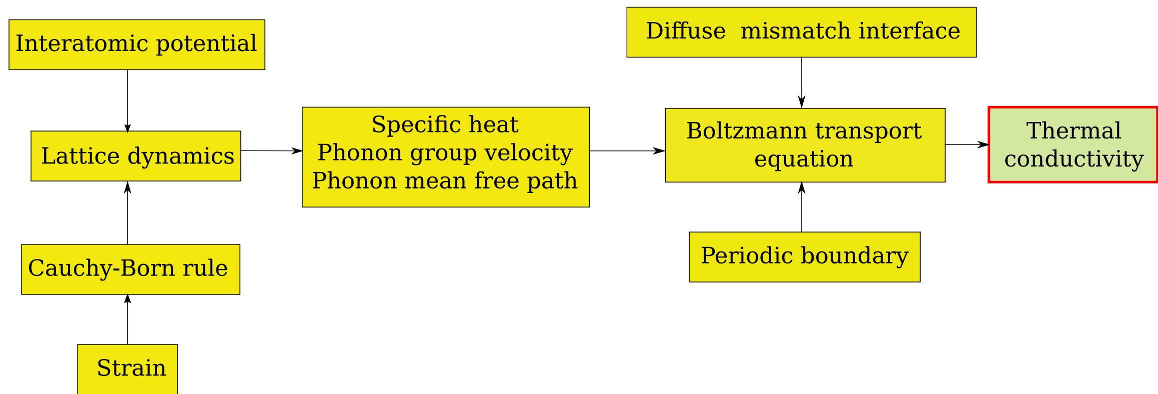

Figure 2.2: Theoretical model for the analysis of strain effect on the phonon thermal conductivity of Si/Ge nanocomposites.

Several assumptions are implied in the theoretical model described above: (1) Strain is assumed to be uniformly distributed throughout the nanocomposites, and residual strain is not considered between Si-Ge interfaces; (2) the BTE model employs

a “gray” assumption with a single group velocity and single relaxation time [48]; (3) three phonon scattering dominates the thermal transport within each material, and phonon scattering due to defects and/or impurities is neglected; (4) the scattering between Si-Ge interface is assumed to be diffuse.

2.2.1 Strain dependent lattice dynamics

At the atomistic level, interaction between atoms in diamond crystal lattices can be described by empirical interatomic potentials such as the Tersoff [49], Brenner [50] and Stillinger-Weber [51] potentials. Tersoff empirical interatomic potential is employed in this work for Si and Ge. Typically, the total potential energy U of a N-atom system is given by

$$U = \sum_{\alpha} U_{\alpha} = \frac{1}{2} \sum_{\alpha \neq \beta} V_{\alpha\beta} \tag{2.1}$$

where α and β are the atoms of the system and $V_{\alpha\beta}$ is the bond energy between atoms α and β given by

$$V_{\alpha\beta} = f_C(r_{\alpha\beta}) \left[a_{\alpha\beta} f_R(r_{\alpha\beta}) + b_{\alpha\beta} f_A(r_{\alpha\beta}) \right] \tag{2.2}$$

where $r_{\alpha\beta}$ is the distance between α and β, f_R and f_A denote the repulsive and attractive pair potentials defined as

$$f_R(r) = A e^{-\lambda_1 r} \tag{2.3}$$

$$f_A(r) = -B e^{-\lambda_2 r} \tag{2.4}$$

respectively, and $f_C(r_{\alpha\beta})$ is a smooth cutoff function going from 1 to 0 in a small range around the cutoff distance R_c, which is chosen to include only the first-neighbor shell for most structures of interest. $f_C(r)$ is defined as

$$f_C(r) = \begin{cases} 1 & r < R_c - D \\ \frac{1}{2} - \frac{1}{2}\sin\left(\frac{\pi(r-R_c)}{2D}\right) & R_c - D \leq r \leq R_c + D \\ 0 & r > R_c + D \end{cases} \tag{2.5}$$

In Eq. (2.2), $a_{\alpha\beta}$ is taken to be 1.0 for both Si and Ge, $b_{\alpha\beta}$ is a measure of the bond order given by

$$b_{\alpha\beta} = \left(1 + \mu^n \zeta_{\alpha\beta}^n\right)^{-1/2n}, \tag{2.6}$$

$$\zeta_{\alpha\beta} = \sum_{\kappa \neq \alpha,\beta} f_C(r_{\alpha\kappa}) g(\theta_{\alpha\beta\kappa}) \exp\left(\lambda_3^3 (r_{\alpha\beta} - r_{\alpha\kappa})^3\right), \tag{2.7}$$

$$g(\theta_{\alpha\beta\kappa}) = 1 + c^2/d^2 - c^2/\left[d^2 + (h - \cos\theta_{\alpha\beta\kappa})^2\right] \tag{2.8}$$

where κ denotes an atom, and $\theta_{\alpha\beta\kappa}$ is the bond angle between the bonds $\alpha\beta$ and $\alpha\kappa$. All remaining variables are constant parameters. For Si, the constants are summarized in the 3rd column of Table I in Ref. [49]. For Ge, the constants are adopted from Table I in Ref. [52].

In the classical lattice dynamics, by using the periodicity of the crystal structure, the phonon frequency spectrum can be obtained by computing the eigenvalues of the dynamical matrix $\mathbf{D}(\mathbf{k})$ for each wave vector $\mathbf{k}$ in the first Brillouin zone, i.e. [53],

$$\mathbf{D}(\mathbf{k}) = \frac{1}{M} \begin{bmatrix} \sum_\beta \Phi_{j,k}^{11}(\alpha,\beta) e^{i\mathbf{k}\cdot(\mathbf{x}_\beta^0 - \mathbf{x}_\alpha^0)} & \sum_\beta \Phi_{j,k}^{12}(\alpha,\beta) e^{i\mathbf{k}\cdot(\mathbf{x}_\beta^0 - \mathbf{x}_\alpha^0)} \\ \sum_\beta \Phi_{j,k}^{21}(\alpha,\beta) e^{i\mathbf{k}\cdot(\mathbf{x}_\beta^0 - \mathbf{x}_\alpha^0)} & \sum_\beta \Phi_{j,k}^{22}(\alpha,\beta) e^{i\mathbf{k}\cdot(\mathbf{x}_\beta^0 - \mathbf{x}_\alpha^0)} \end{bmatrix} \quad j,k = 1,2,3 \tag{2.9}$$

where α and β denote the atoms in the unit cell, M is the mass of atom, $\mathbf{k}$ is wave vector, $\mathbf{x}_\alpha^0$ and $\mathbf{x}_\beta^0$ are the equilibrium positions of atom α and β, respectively, and $\Phi_{j,k}^{pq}(\alpha, \beta)$ is force constant defined by

$$\Phi_{j,k}^{pq}(\alpha, \beta) = \left. \frac{\partial^2 U(\mathbf{x})}{\partial \mathbf{x}_{\alpha j} \partial \mathbf{x}_{\beta k}} \right|_{\mathbf{x}=\mathbf{x}^0, \alpha \in B_p, \beta \in B_q}$$
$$j, k = 1, 2, 3 \qquad p, q = 1, 2, \tag{2.10}$$

where $\mathbf{x}_{\alpha j}$ and $\mathbf{x}_{\beta k}$ are the jth and the kth component of the position of atoms α and β, respectively. B_p and B_q are Bravais lattices p and q, respectively. Note that we choose α to be the center atom and loop atom β over all the atoms in the crystal lattice. The phonon frequencies can be calculated by $\omega_{s\mathbf{k}} = \sqrt{\lambda_{s\mathbf{k}}}$, where $\lambda_{s\mathbf{k}}$ are the eigenvalues of the 6×6 dynamical matrix $\mathbf{D}(\mathbf{k})$ and s is the index of the polarization.

When there is an applied strain, to relate the continuum level description of deformation to displacements of the atoms in the crystal lattice as shown in Fig. 2.3, we employ the hypotheses of the Cauchy-Born rule [54] which states that the crystal lattice is homogeneously distorted according to the deformation gradient. For Si/Ge crystal, there exist additional inner displacements between the two Bravais lattices. The Cauchy-Born rule gives

$$\mathbf{x}_\beta^0 - \mathbf{x}_\alpha^0 = \mathbf{F}\left(\mathbf{X}_\beta^0 - \mathbf{X}_\alpha^0\right) + \boldsymbol{\xi} \tag{2.11}$$

where $\mathbf{F}$ is the deformation gradient of the Bravais lattice, $\mathbf{X}_\alpha^0$ and $\mathbf{X}_\beta^0$ are the equilibrium positions of atom α and β in the undeformed configuration, respectively, and $\boldsymbol{\xi}$ is the inner displacement of the two FCC Bravais lattices. In the reciprocal lattice of a Bravais lattice, from Eq. (2.11), it is easy to show that, a given wave vector $\mathbf{k}^0$ in the undeformed configuration of the lattice deforms to $\mathbf{k}$ in the

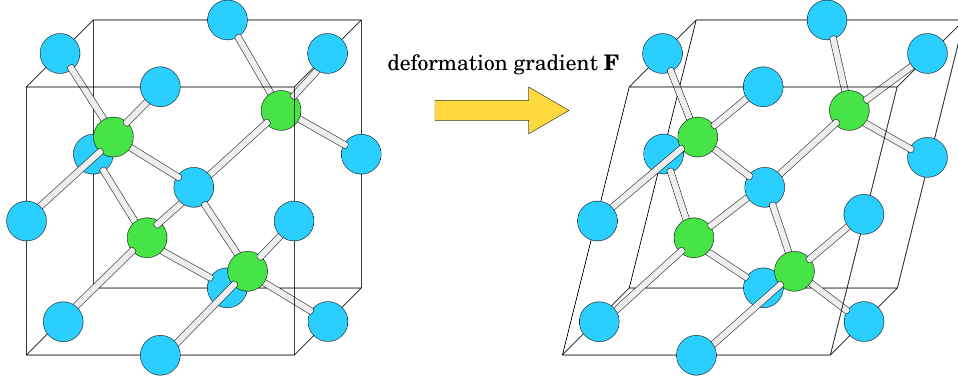

Figure 2.3: Atom configuration and deformation for a diamond lattice.

deformed configuration with the relation

$$\mathbf{k} = \mathbf{F}^{-T}\mathbf{k}^0 \tag{2.12}$$

Substituting Eqs. (2.11, 2.12) into Eq. (2.9), the strain dependent dynamical matrix can then be written as [53]

$$\mathbf{D}(\mathbf{k}) = \frac{1}{M}\begin{bmatrix} \sum_{\beta}\overline{\Phi}^{11}_{jk}(\alpha,\beta)e^{i\mathbf{k}^0\cdot(\mathbf{X}^0_\beta-\mathbf{X}^0_\alpha)} & \sum_{\beta}\overline{\Phi}^{12}_{jk}(\alpha,\beta)e^{i\mathbf{k}^0\cdot(\mathbf{X}^0_\beta-\mathbf{X}^0_\alpha-\mathbf{F}^{-1}\boldsymbol{\xi})} \\ \sum_{\beta}\overline{\Phi}^{21}_{jk}(\alpha,\beta)e^{i\mathbf{k}^0\cdot(\mathbf{X}^0_\beta-\mathbf{X}^0_\alpha+\mathbf{F}^{-1}\boldsymbol{\xi})} & \sum_{\beta}\overline{\Phi}^{22}_{jk}(\alpha,\beta)e^{i\mathbf{k}^0\cdot(\mathbf{X}^0_\beta-\mathbf{X}^0_\alpha)} \end{bmatrix}$$

$$\alpha = 1, \quad j,k = 1,2,3 \tag{2.13}$$

where

$$\overline{\Phi}^{pq}_{j,k}(\alpha,\beta) = \frac{\partial^2 U(\mathbf{x})}{\partial \mathbf{x}_{\alpha j}\partial \mathbf{x}_{\beta k}}\Bigg|_{\mathbf{x}=\mathbf{x}^0(\mathbf{X}^0,\mathbf{F},\boldsymbol{\xi}),\alpha\in B_p,\beta\in B_q}$$

$$j,k = 1,2,3 \qquad p,q = 1,2 \tag{2.14}$$

and $\mathbf{F}^{-1}$ is the inverse of $\mathbf{F}$. The phonon frequencies of the strained bulk crystal Si and Ge, $\omega_{s\mathbf{k}}(\mathbf{F}, \boldsymbol{\xi})$, can be obtained by computing the eigenvalues of Eq. (2.13). After the phonon frequency spectrum is obtained, the Helmholtz free energy A of the system can be calculated by

$$\begin{aligned} A = U(\mathbf{X}^0, \mathbf{F}, \boldsymbol{\xi}) + \frac{1}{2} \sum_{\mathbf{k}} \sum_{s=1}^{6} \hbar\omega_{s\mathbf{k}}(\mathbf{F}, \boldsymbol{\xi}) \\ + k_B T \sum_{\mathbf{k}} \sum_{s=1}^{6} \ln \left(1 - e^{-\frac{\hbar\omega_{s\mathbf{k}}(\mathbf{F}, \boldsymbol{\xi})}{k_B T}} \right) \end{aligned} \tag{2.15}$$

where $U(\mathbf{X}^0, \mathbf{F}, \boldsymbol{\xi})$ is the total potential energy of the system at the deformed equilibrium position, $\hbar$ is the reduced Planck's constant, k_B is the Boltzmann constant and T is temperature. For a given deformation gradient $\mathbf{F}$, the inner displacement $\boldsymbol{\xi}$ can be determined by minimizing the Helmholtz free energy, i.e.,

$$\frac{\partial A}{\partial \boldsymbol{\xi}} = 0 \tag{2.16}$$

In this work, we impose uniaxial strains from -2% (compressive) to 2% (tensile) in the x-direction, which gives a maximum of 2% change of the crystal volume. This range of the strain are achievable with moderate external loadings. In terms of the deformation gradient, the uniaxial strains are corresponding to $F_{11} = [0.98, 1.02]$, $F_{22} = F_{33} = 1.0$ and $F_{ij} = 0$, $i \neq j$. With the maximum strain in one direction fixed, hydrostatic strains are applied. For the hydrostatic strains, $F_{ii} = [0.98, 1.02]$, $i = 1, 2, 3$ and $F_{ij} = 0$, $i \neq j$. Note that, for hydrostatic and uniaxial deformations, $\boldsymbol{\xi} = 0$ due to the symmetry of the lattice deformation.

2.2.2 Strain dependent thermodynamic and phonon scattering properties

For a given deformation gradient **F**, we compute the phonon frequency spectrum of Si and Ge lattices by sampling the **k** points in the first Brillouin zone. Once the phonon frequency spectrum is obtained, the bulk thermodynamic and phonon scattering properties of Si and Ge can be calculated. Of particular interest are the specific heat, the average phonon group velocity and the average phonon mean free path. As will be described in Chap. 2.2.3, they are the physical variables used in the BTE for the analysis of thermal transport in the Si/Ge nanocomposites. To compute these thermodynamic and phonon scattering properties, we first compute the bulk thermal conductivity of Si and Ge as a function of **F** by using the Slack relation [55, 56]. The Slack relation is suitable for calculating the thermal conductivity of nonmetallic crystals at high temperatures (above 1/5 of the Debye temperature) where heat is mainly carried by acoustic phonons and the scattering is mainly intrinsic three phonon process. The bulk thermal conductivity is given by [55, 56]

$$k_b = \frac{3.1 \times 10^7 \langle M \rangle \delta T_D^3}{T \langle \gamma^2 \rangle N_c^{2/3}} \tag{2.17}$$

where $\langle M \rangle$ is the average atomic mass of the crystal, δ^3 is the average volume per atom, N_c is the number of atoms in a primitive cell and T_D is high temperature limit of the Debye temperature defined by

$$T_D^2 = \frac{5h^2 \int_0^\infty \omega^2 D_p(\omega) \mathrm{d}\omega}{3k_B^2 \int_0^\infty D_p(\omega) \mathrm{d}\omega} \tag{2.18}$$

where h is Planck's constant, ω is the frequency and $D_p(\omega)$ is phonon density of states. $\langle\gamma^2\rangle$ is mode averaged square of the Grüneisen parameter given by

$$\langle\gamma^2\rangle = \frac{1}{C}\sum_{\mathbf{k}}\sum_{s=1}^{6}(\gamma_{s\mathbf{k}})^2 C_{s\mathbf{k}} \tag{2.19}$$

where the Grüneisen parameter $\gamma_{s\mathbf{k}}$ for the s-th mode of a given wave vector $\mathbf{k}$ is defined as

$$\gamma_{s\mathbf{k}} = -\frac{\partial \ln \omega_{s\mathbf{k}}}{\partial \ln V}, \tag{2.20}$$

where V is the volume per atom, $C_{s\mathbf{k}}$ is the phonon specific heat given by

$$C_{s\mathbf{k}} = k_B \frac{(\frac{\hbar\omega_{s\mathbf{k}}}{k_B T})^2 e^{\frac{\hbar\omega_{s\mathbf{k}}}{k_B T}}}{(e^{\frac{\hbar\omega_{s\mathbf{k}}}{k_B T}} - 1)^2}, \tag{2.21}$$

and C is the total specific heat given by

$$C = \sum_{\mathbf{k}}\sum_{s=1}^{6} C_{s\mathbf{k}}. \tag{2.22}$$

Note that, since the phonon frequencies $\omega_{s\mathbf{k}}(\mathbf{F}, \boldsymbol{\xi})$ depend on the applied strain, thermodynamic properties such as T_D, γ, C and k_b are all functions of strain. For the simplicity of notation, "$(\mathbf{F}, \boldsymbol{\xi})$" is not shown explicitly for these quantities.

The acoustic phonon group velocity for sth polarization of wavevector $\mathbf{k}$ is calculated by

$$v_{s\mathbf{k}} = \left|\frac{\partial \omega_{s\mathbf{k}}}{\partial \mathbf{k}}\right|. \tag{2.23}$$

Then the average phonon group velocity can be obtained by

$$v = \frac{\sum_{\mathbf{k}} \sum_{s=1}^{3} C_{s\mathbf{k}} v_{s\mathbf{k}}}{C^a} \qquad s \in \text{acoustic phonon branches,} \tag{2.24}$$

with C^a being the average acoustic phonon specific heat obtained by summing $C_{s\mathbf{k}}$ over the acoustic branches

$$C^a = \sum_{\mathbf{k}} \sum_{s=1}^{3} C_{s\mathbf{k}} \qquad s \in \text{acoustic phonon branches.} \tag{2.25}$$

After the bulk thermal conductivity k_b, the average acoustic specific heat C^a and the average phonon group velocity v are obtained, the average phonon mean free path (MFP) can be calculated from approximated Kinetic theory by [57]

$$\Lambda \approx \frac{3k_b}{C^a v}, \tag{2.26}$$

Note that, in Eqs. (2.24), (2.25) and (2.26), only the acoustic branches of the phonon dispersion are included. The optical phonons are excluded for a better approximation of the average phonon MFP since they contribute little to the thermal conductivity around room temperature for Si and Ge due to their small group velocities. More detailed justification for this choice can be found in Refs. [58, 57]. Again, the phonon scattering properties Λ, v and C^a are all functions of the strain.

2.2.3 Boltzmann transport equation model for nanocomposites

Once the strain dependent phonon thermal properties of the bulk Si and Ge are obtained, the effective thermal conductivity of nanocomposites can then be calculated by using a thermal transport model. Among various models that can be used to predict the thermal conductivity of nanocomposites [36, 37, 38], BTE based thermal modeling approaches have been developed and applied to thermal transport analysis in various applications with demonstrated accuracy and efficiency (see [48] for a review). Among the BTE models, the "gray" BTE approach, which assumes all phonons have the same average group velocity and relaxation time, is adopted in this work. Published work has shown that frequency independent group velocity and relaxation time is a good approximation for the calculation of cross-plane phonon thermal conductivity [57]. By applying strain dependent thermal properties into BTE, the strain dependent thermal conductivity can be calculated.

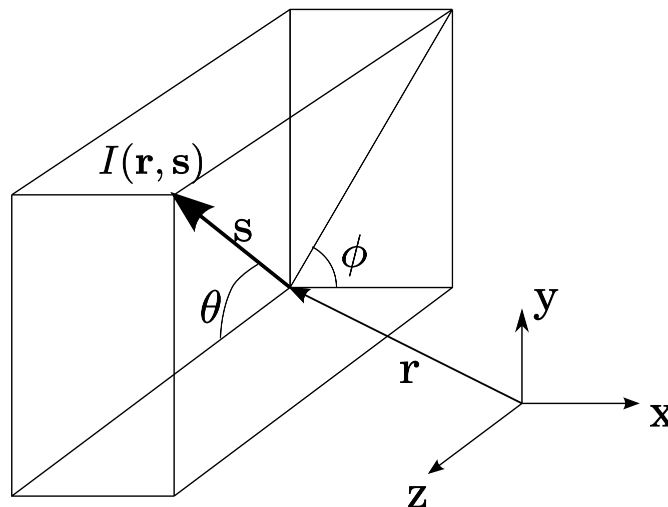

Figure 2.4: Directional phonon intensity.

In this work, we adopt the "gray" BTE approach for the computational thermal transport analysis of Si/Ge nanocomposites. The BTE model under "gray" assumption can be expressed in terms of total phonon intensity as [59, 60]

$$\nabla \cdot \left(I(\mathbf{r},\mathbf{s}) \cdot \mathbf{s}\right) = -\frac{I(\mathbf{r},\mathbf{s}) - I_0(\mathbf{r})}{\Lambda} \tag{2.27}$$

where $I(\mathbf{r},\mathbf{s})$ is the total phonon intensity at a spatial position $\mathbf{r} = \{x, y, z\}$ over a path length ds in the direction of unit vector $\mathbf{s}$. As shown in Fig. 2.4, $\mathbf{s}$ is defined by

$$\mathbf{s} = sin\theta cos\phi \mathbf{e}_x + sin\theta sin\phi \mathbf{e}_y + cos\theta \mathbf{e}_z \tag{2.28}$$

where $\theta \in [0, \pi]$ and $\phi \in [0, 2\pi]$ represent polar and azimuthal angles, respectively, and $\mathbf{e}_x$, $\mathbf{e}_y$ and $\mathbf{e}_z$ are the unit vectors in the x, y and z directions, respectively. $I_0(\mathbf{r})$ is the equivalent equilibrium phonon intensity which is given by

$$I_0(\mathbf{r}) = \frac{1}{4\pi} \int_0^{2\pi} \int_0^{\pi} I(\mathbf{r},\mathbf{s}) sin\theta d\theta d\phi \tag{2.29}$$

Assuming a uniform distribution of the Si nanowires, the BTE can be solved in a 2-D unit cell of the nanocomposite material as shown in Fig. 2.5. The edge length of the unit cell is denoted as L. The phonon intensities in the Si-Ge domains are determined by the BTE. Periodic boundary conditions are employed on the outer boundary of the unit cell. The phonon scattering at the Si-Ge interface is assumed to be diffuse. In this work, the boundary and interface models developed by Yang and Chen [9] for nanocomposites are adopted and implemented using the finite volume method. The boundary and interface conditions are briefly summarized as follows. For the top ($y = L$) and bottom ($y = 0$) edges, the periodic boundary condition can

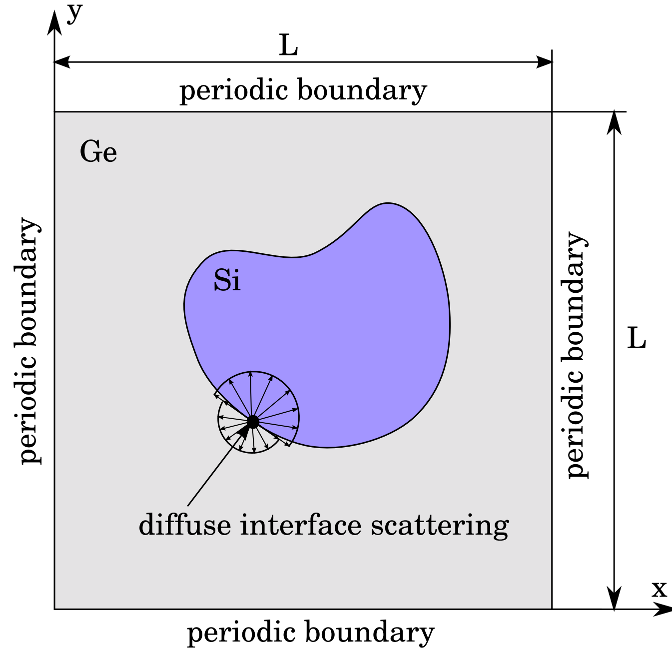

Figure 2.5: Unit cell of the Si/Ge nanocomposite material.

be written as

$$I(x, L, \mathbf{s}) = I(x, 0, \mathbf{s}), \tag{2.30}$$

for all x and $\mathbf{s}$, which implies that phonons coming in equal phonons going out for a given x and $\mathbf{s}$. For the right ($x = 0$) and left ($x = L$) edges, the periodic boundary condition implies that the difference between the phonon intensities in any given direction at the right and left edges is independent of y. This constant difference is imposed by a temperature drop, ΔT, between the left and right edges. The magnitude of ΔT, however, does not affect the result of the thermal conductivity. The periodic

boundary condition is given by

$$I(0, y, \mathbf{s}) - I(L, y, \mathbf{s}) = \frac{v_{Ge} C^a_{Ge} \Delta T}{4\pi}, \tag{2.31}$$

where v_{Ge} and C^a_{Ge} denote the group velocity and acoustic specific heat of Ge, respectively. The diffuse interface scattering is represented by a simple diffuse mismatch model which assumes, at the interface, part of the phonons are transmitted through and the rest are reflected back. The transmitted and reflected phonons are evenly distributed across all angles on each side of the interface, as shown in Fig. 2.5. From energy conservation, the relation of reflectivity R and transmissivity T is given by

$$T_{GS} = R_{SG} = 1 - T_{SG}, \tag{2.32}$$

where the subscript GS denotes from Ge into Si and vise versa, and T_{GS} is given by [57]

$$T_{GS} = \frac{C^a_{Si} v_{Si}}{C^a_{Ge} v_{Ge} + C^a_{Si} v_{Si}}. \tag{2.33}$$

By solving the BTE in both Si and Ge domains with the boundary and interface conditions, the phonon intensity $I(x, y, \mathbf{s})$ can be obtained. It is then straightforward to calculate the effective temperature distribution, heat flux and thermal conductivity. Note that, since the local thermal equilibrium condition breaks down in nanostructures, an effective temperature is used to represent the

local energy density, i.e.,

$$T(x,y) = \frac{4\pi I_0(x,y)}{C^a v} \tag{2.34}$$

The average temperature at each y-z plane along the x-direction is then obtained as

$$\bar{T}(x) = \frac{1}{L}\int_0^L T(x,y)\mathrm{d}y \tag{2.35}$$

The heat flux in the x-direction, q_x, is computed by integrating the x-component of the phonon intensity over the entire solid angle

$$q_x(x,y) = \int_0^{2\pi}\int_0^{\pi} I(x,y,\mathbf{s}) sin^2\theta cos\phi d\theta d\phi \tag{2.36}$$

The effective phonon thermal conductivity is then calculated by using Fourier's law.

$$k_p = \frac{\int_0^L q_x(x,y)\mathrm{d}y}{\bar{T}(0) - \bar{T}(L)} \tag{2.37}$$

Note that k_p is guaranteed to be constant along the x-axis by the periodic boundary conditions imposed by Eq. (2.30).

2.2.4 Finite volume solution of BTE

Due to the similarity between the thermal radiative transfer equation (RTE) and the BTE, numerical methods for solving RTE are often applicable to BTE. Among a variety of numerical methods that are used to solve the RTE, the discrete ordinates method (DOM) and the finite volume method (FVM) are most popular. The DOM is known for its simplicity and efficiency. However, like the finite

difference method, the DOM typically requires a structured grid, which imposes a major difficulty for problems involving complex geometries. In comparison, the FVM can be easily applied to unstructured meshes. Thus it provides greater flexibility in treating complex geometries. In addition, integration over the control angles is calculated exactly and heat flux in control volumes is automatically conserved in FVM [61]. Due to these attractive properties, the FVM has been employed for radiative thermal transport analysis in various applications [62, 63, 64, 65]. It has also been applied to obtain BTE solution for heat transfer analysis of submicron structures [66]. In this work, as the Si/Ge nanocomposites to be investigated contain Si nanowires with different shaped cross-sections as shown in Fig. 2.1, the FVM is employed in the computational analysis. One difficulty in the FVM solution of the BTE on an unstructured mesh is that the control angles may overlap with the control volume boundaries. In such cases, the overlapping control angle contains both the outgoing and incoming phonons. Several authors have addressed this issue for radiative heat transfer problems [63, 64, 67]. We employ an exact treatment proposed in Ref. [67]. This treatment is found to be effective to resolve the problem for our calculations.

As shown in Fig. 2.6, the 2-D domain of the Si-Ge unit cell is discretized into non-overlapping triangular volumes (or elements). The volume of a given triangular element is denoted as ΔV. The length of the edges is denoted as ΔA_i, $i = 1, 2, 3$. Within each triangular volume, the phonon intensity is defined on the center node of the triangular volume. The total solid angle, 4π, of the center node is discretized into $N_\theta \times N_\phi$ control angles along θ and ϕ directions. The control angles are denoted as $\Delta\Omega^{mn}$ ($1 \leq m \leq N_\theta$, $1 \leq n \leq N_\phi$) with the polar and azimuthal angles spanning from θ^m to θ^{m+1} and ϕ^n to ϕ^{n+1}, respectively, as shown in Fig. 2.6. Within each control

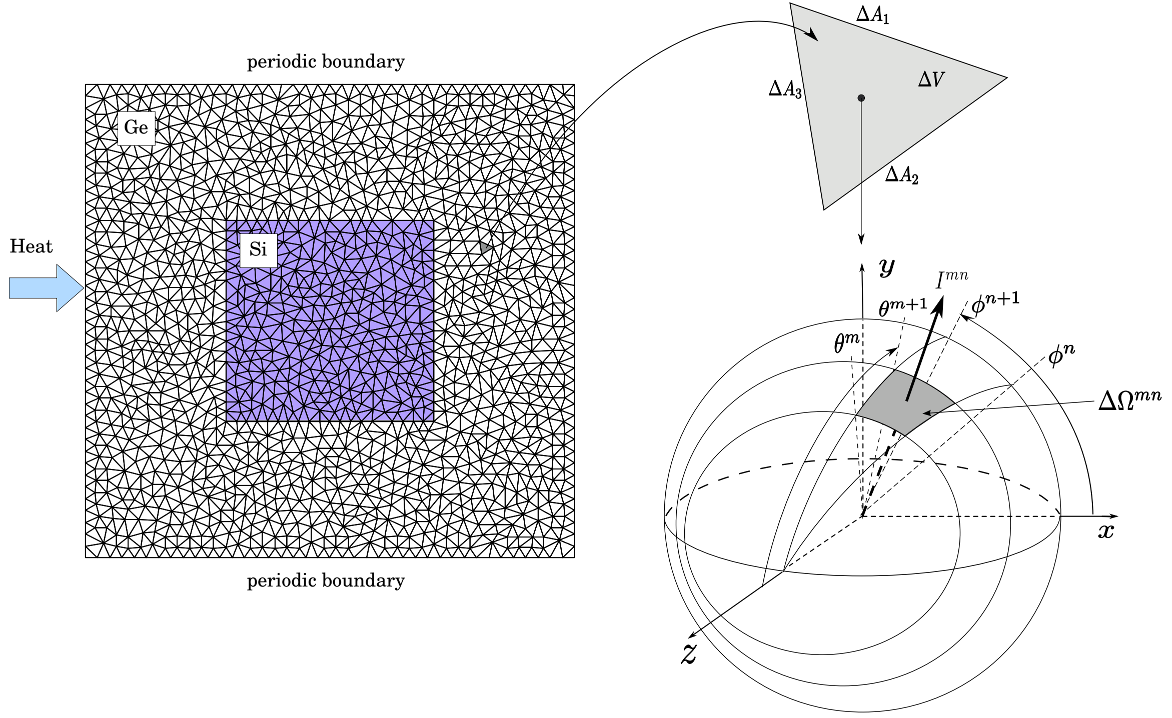

Figure 2.6: Spatial and angular discretization.

volume and control angle $\Delta\Omega^{mn}$, the phonon intensity is assumed to be constant and denoted as I^{mn}. For each control volume and control angle, the governing BTE, Eq. (2.27), is integrated over ΔV and $\Delta\Omega^{mn}$ to yield

$$\int_{\Delta\Omega^{mn}} \int_{\Delta V} \nabla \cdot (I\mathbf{s})\,\mathrm{d}V\,\mathrm{d}\Omega = \int_{\Delta\Omega^{mn}} \int_{\Delta V} (-\frac{I - I_0}{\Lambda})\,\mathrm{d}V\,\mathrm{d}\Omega \tag{2.38}$$

Applying the divergence theorem, Eq. (2.38) can be rewritten as

$$\int_{\Delta\Omega^{mn}} \int_{\Delta A} I\mathbf{s} \cdot \mathbf{n}\,\mathrm{d}A\,\mathrm{d}\Omega = \int_{\Delta\Omega^{mn}} \int_{\Delta V} (-\frac{I - I_0}{\Lambda})\,\mathrm{d}V\,\mathrm{d}\Omega \tag{2.39}$$

For a given triangular control volume with a center node P, the phonon intensity in the control angle $\Delta\Omega^{mn}$ is denoted as I_P^{mn}. Assuming that for a given control angle,

facial intensities are constant on each boundary face of the volume, the following finite volume formulation can be obtained from Eq. (2.39) as

$$\sum_{i=1,2,3} I_i^{mn}\,\Delta A_i D_{Ci}^{mn} = \frac{1}{\Lambda}\left(-I_P^{mn} + (I_0^{mn})_P\right)\Delta V\,\Delta\Omega^{mn}, \tag{2.40}$$

where I_i^{mn} is the facial intensity on ΔA_i, $i = 1, 2, 3$, and the directional weight D_{Ci}^{mn} is given by

$$D_{Ci}^{mn} = \int_{\theta^m}^{\theta^{m+1}} \int_{\phi^n}^{\phi^{n+1}} (\mathbf{s}\cdot\,\mathbf{n}_i) sin\theta \mathrm{d}\theta\,\mathrm{d}\phi, \qquad i = 1, 2, 3, \tag{2.41}$$

where $\mathbf{s}$ is given by Eq. (2.28), $\mathbf{n}_i$ is the outward normal of the i-th face of the control volume. For 2-D problems, D_{Ci}^{mn} can be obtained as

$$D_{Ci}^{mn} = \left[\frac{\Delta\theta}{2} - \frac{1}{4}\left(sin2\theta^{m+1} - sin2\theta^m\right)\right] \times \\ \left[n_x\left(sin\phi^{n+1} - sin\phi^n\right) - n_y\left(cos\phi^{n+1} - cos\phi^n\right)\right] \tag{2.42}$$

where n_x and n_y are the x- and y-components of $\mathbf{n}_i$. In Eq. (2.41), the sign of D_{Ci}^{mn} (or equivalently, the sign of $\mathbf{s}\cdot\mathbf{n}_i$) determines whether the phonons are incoming or outgoing across the faces of control volume.

The facial intensity I_i^{mn} is then related to the nodal intensity by a step scheme assuming a downstream facial intensity is equal to the upstream nodal intensity. For example, as shown in Fig. 2.7, for face 2 of the control volume of node P, if the azimuthal angle of $\mathbf{s}$ is between ϕ^2 and ϕ^3, one obtains $\mathbf{s}\cdot\mathbf{n}_2 > 0$, i.e., phonons are outgoing and P is the upstream node. Therefore, $I_{i=2}^{mn} = I_P^{mn}$. If $\mathbf{s}$ is between ϕ^4 and ϕ^5, then $\mathbf{s}\cdot\mathbf{n}_2 < 0$ and the node I of the neighbor control volume is the upstream node. Therefore, $I_{i=2}^{mn} = I_I^{mn}$. However, as shown in Fig. 2.7, the control angle from

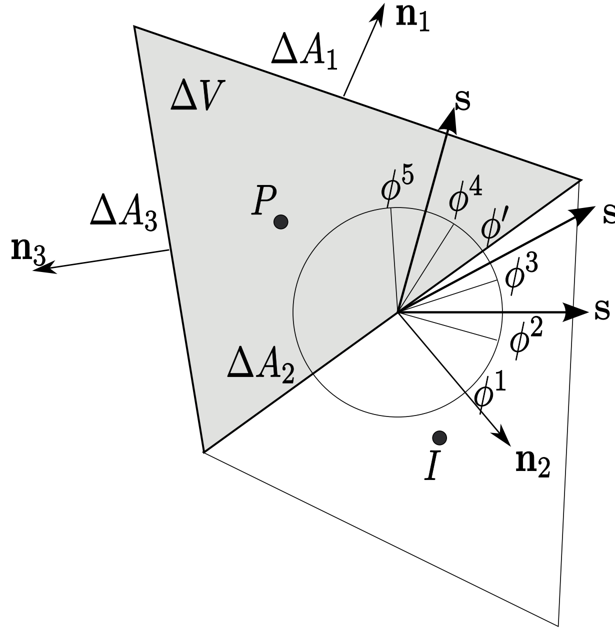

Figure 2.7: Step scheme for the facial intensity.

ϕ_3 to ϕ_4 overlaps with the face and contains both incoming and outgoing phonons. It is more involved to determine the facial intensity in this situation. The solution to this control angle overlap problem has been summarized in Ref. [63]. In this work, we employ an exact treatment described in Ref. [67] which splits the control angle into $[\phi^3, \phi']$ and $[\phi', \phi^4]$ as shown in Fig. 2.7, and integrates the two resultant control angle separately. The facial intensity can be expressed by the following general expression as

$$I_i^{mn} D_{ci}^{mn} = I_P^{mn} D_{ci,out}^{mn} + I_I^{mn} D_{ci,in}^{mn} \tag{2.43}$$

where, for a non-overlapping control angle, if $\mathbf{s} \cdot \mathbf{n}_i > 0$, then

$$D_{Ci,out}^{mn} = \int_{\theta^m}^{\theta^{m+1}} \int_{\phi^n}^{\phi^{n+1}} (\mathbf{s} \cdot \mathbf{n}_i) sin\theta \mathrm{d}\theta \, \mathrm{d}\phi, \qquad D_{Ci,in}^{mn} = 0, \tag{2.44}$$

and if $\mathbf{s}\cdot\mathbf{n}_i < 0$, then

$$D^{mn}_{Ci,in} = \int_{\theta^m}^{\theta^{m+1}} \int_{\phi^n}^{\phi^{n+1}} (\mathbf{s}\cdot\ \mathbf{n}_i) sin\theta \mathrm{d}\theta\, \mathrm{d}\phi, \qquad D^{mn}_{Ci,out} = 0. \tag{2.45}$$

For an overlapping control angle, without loss of generality, assuming $\mathbf{s}\cdot\mathbf{n}_i > 0$ in $[\phi^n, \phi']$ and $\mathbf{s}\cdot\mathbf{n}_i < 0$ in $[\phi', \phi^{n+1}]$, we have

$$D^{mn}_{Ci,out} = \int_{\theta^m}^{\theta^{m+1}} \int_{\phi^n}^{\phi'} (\mathbf{s}\cdot\ \mathbf{n}_i) sin\theta \mathrm{d}\theta \mathrm{d}\phi, \tag{2.46}$$

$$D^{mn}_{Ci,in} = \int_{\theta^m}^{\theta^{m+1}} \int_{\phi'}^{\phi^{n+1}} (\mathbf{s}\cdot\ \mathbf{n}_i) sin\theta \mathrm{d}\theta\, \mathrm{d}\phi. \tag{2.47}$$

When a control volume face is on the Si-Ge interface, the interface condition given in Eq. (2.32) is applied by replacing I^{mn}_I in Eq. (2.43) with

$$I^{mn}_I = \frac{R_{PI}}{\pi} \sum_{mn} I^{mn}_P D^{mn}_{Ci,out} - \frac{T_{IP}}{\pi} \sum_{mn} I^{mn}_I D^{mn}_{Ci,in} \tag{2.48}$$

where R_{PI} is the reflectivity from medium of node P to the medium of node I, and T_{IP} is the transmissivity from medium of node I to the medium of node P. It should be noted that the interface condition only modifies I^{mn}_I in Eq. (2.43) and I^{mn}_P remains the same. Otherwise, the transmission and reflection of the phonons would be double counted and the energy conservation condition would be violated. Substituting Eq. (2.43) into Eq. (2.40), the finite volume formulation of the BTE for each control volume and control angle can be obtained as

$$\begin{aligned}(\sum_i \Delta A_i D^{mn}_{Ci,out} + \frac{\Delta V}{\Lambda}\Delta\Omega^{mn} - \frac{\Delta V}{4\pi\Lambda}(\Delta\Omega^{mn})^2) I^{mn}_P \\ = -\sum_i \Delta A_i D^{mn}_{Ci,in} I^{mn}_I + \frac{\Delta V}{4\pi\Lambda}(\sum_{m'n'\neq mn} I^{m'n'}_P \Delta\Omega^{m'n'})\,\Delta\Omega^{mn}\end{aligned} \tag{2.49}$$

For the global system, there are a total of $N_V \times N_\phi \times N_\theta$ equations, where N_V is the number of control volumes. This set of equations are solved iteratively by using the Gauss-Seidel method. Note that, like the DOM, in Gauss-Seidel iterations, the nodal intensities are calculated in each control volume and control angle by using the values obtained from the last iteration. No global matrix storage is required. The iteration stops when the following convergence condition is reached:

$$max(\left|I_P^{mn} - (I^{mn})_P^{old}\right| / I_P^{mn}) \leq 10^{-6}. \quad (2.50)$$

Note that, while in this work we investigate the thermal conductivity of composite materials with periodic nanostructures, the approach presented is not limited to periodic systems. For non-periodic systems, the analysis procedure remains the same with the periodic boundary conditions (Eqs. (2.30, 2.31)) changing to temperature [68], diffuse [69] or other appropriate boundary conditions.

2.3 Results and Discussion

2.3.1 Strain effect on thermodynamic properties of bulk Si and Ge

In this section, we investigate the strain effect on thermodynamic properties of bulk Si and Ge. From the lattice dynamics with Tersoff potential, various thermodynamic properties of bulk Si and Ge can be calculated. A few thermodynamic properties that are used in the calculation of the thermal conductivity are first calculated under unstrained condition. These results are compared with the experimental data and other theoretical results. Table 2.1 lists

the specific heat (C), Debye temperature (T_D), Grüneisen parameter (γ), longitudinal acoustic group velocity at Γ point in the first Brillouin zone (v_{LA}^{Γ}), transverse acoustic group velocity at Γ point (v_{TA}^{Γ}), longitudinal acoustic group velocity at X point (v_{LA}^{X}), and the bulk thermal conductivity (k_b) of Si. The comparison shows that the Tersoff potential gives reasonable estimates to the thermodynamic properties, including the bulk thermal conductivity.

Table 2.1: Room temperature thermodynamic properties of bulk Si

$C(\frac{J}{m^3K})$	$T_D(K)$	γ	$v_{LA}^{\Gamma}(\frac{m}{s})$	$v_{TA}^{\Gamma}(\frac{m}{s})$	$v_{LA}^{X}(\frac{m}{s})$	$k_b(\frac{W}{mK})$
1.59×10^6	720	0.79	8705	5470	4540	167.6
1.65×10^6[70]	645[71]	0.8[72]	8480[73]	5860[73]	4240[73]	156[74]

As mentioned in Chap. 2.2.1, we considered a maximum of 2% strain in every direction caused by four types of strains: hydrostatic compressive, hydrostatic tensile, uniaxial compressive and uniaxial tensile, as shown in Fig. 2.8. In the following discussion, if not otherwise specified, the strains are corresponding to a 2% strain, i.e., $F_{ii} = 0.98, i = 1,2,3$ and $F_{ij} = 0, i \neq j$ for hydrostatic compressive strain, $F_{ii} = 1.02, i = 1,2,3$ and $F_{ij} = 0, i \neq j$ for hydrostatic tensile strain, $F_{11} = 0.98, F_{22} = F_{33} = 1.0$ and $F_{ij} = 0, i \neq j$ for uniaxial compressive strain, and $F_{11} = 1.02, F_{22} = F_{33} = 1.0$ and $F_{ij} = 0, i \neq j$ for uniaxial tensile strain.

Figure 2.9 shows the dispersion relations of Si for different strain conditions calculated from Eq. (2.13). Figure 2.9 (a) is for unstrained case and the dots in it are experimental data from [75]. The phonon dispersion calculated from our lattice dynamics model matches well with experimental data. Figure 2.9 (b) and (c)

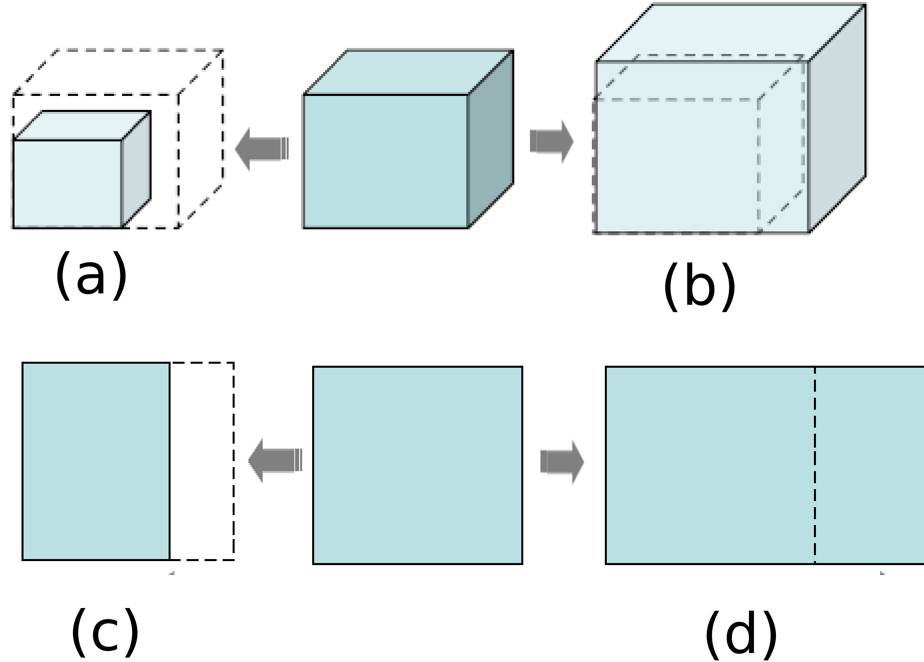

Figure 2.8: Strains considered: (1) hydrostatic compressive. (2) Hydrostatic tensile. (3) Uniaxial compressive. (4) Uniaxial tensile.

respectively show dispersion relation of Si when 2% hydrostatic compressive and hydrostatic tensile strains are applied. By comparison of Fig. 2.9 (a)-(c), we find that compressive strain increases phonons frequencies while tensile strain decreases them. Figure 2.9 (d) is the dispersion relation for 2% uniaxial tensile strain. Comparing (c) and (d) we find that hydrostatic strains has a larger influence on phonon frequencies than uniaxial strains. Strain effect on the dispersion relation of Ge is observed to be similar.

After frequency spectrum is known, other scattering properties can be calculated. Figure 2.10 shows the strain effect on the phonon density of states (PDOS) of Si under hydrostatic compressive and tensile strains. A direct sampling method is used in the calculation of PDOS, which generates $100 \times 100 \times 100$ uniformly distributed **k**-points

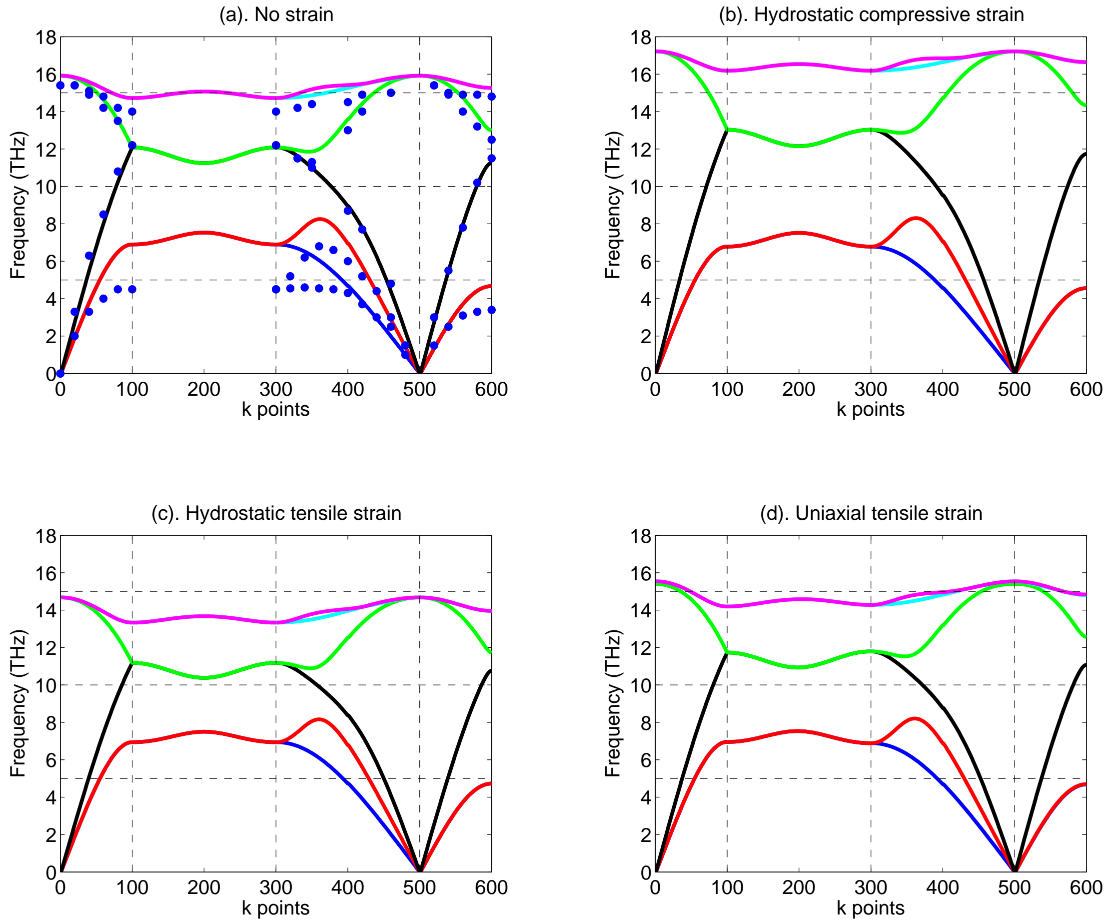

Figure 2.9: Dispersion relation of Si at 0 K for different strain conditions: (1) unstrained (dots are experimental data). (2) Hydrostatic compressive strain. (3) Hydrostatic tensile strain. (4) Uniaxial tensile strain.

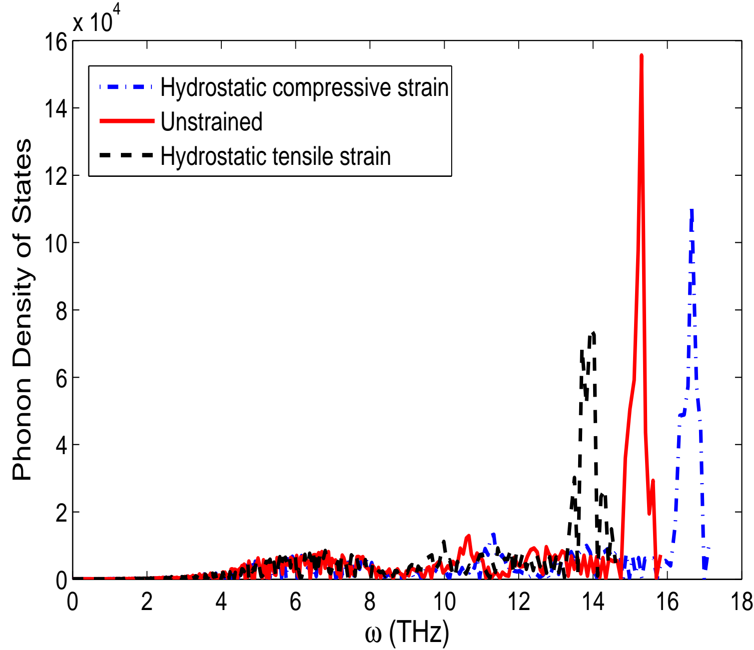

Figure 2.10: Strain dependent phonon density of state of Si at 300 K.

in the first Brillouin zone and approximates the PDOS by a normalized histogram. It is shown that a shift of optical phonons to the left occurs when the tensile strain is applied, while a shift to the right occurs for the compressive strain. In other words, compared to the unstrained case, most optical phonons will be at a lower (or higher) energy when tensile (or compressive) strain is applied. Note that there are similar peak shifts for longitudinal acoustic (LA) phonons, indicating that the hydrostatic strain has a significant effect on them as well. Variations of transverse acoustic phonons are also observed, although not equally significant compared to the LA and optical phonons. Similar behavior of the PDOS is observed for Ge under strain (not shown). The different frequency shift direction of the PDOS is largely due to the change of the stiffness of the atomic bonds which is represented by the force constants given in Eq. (2.14), i.e., a compressive (tensile) strain increases (decreases)

the force constants and consequently increases (decreases) the vibration frequencies of the atoms. Figure 2.11 shows the overall Grüneisen parameter under hydrostatic strain at different temperatures. It's shown that Grüneisen parameter increases when temperature increases and when tensile strain is applied. Again, similar behavior of the Grüneisen parameter of Ge is observed.

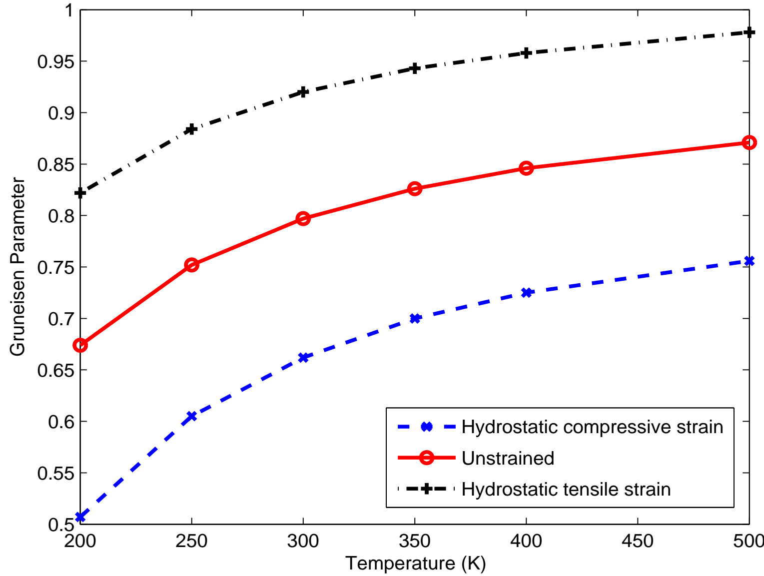

Figure 2.11: Strain dependent Grüneisen parameter of Si with respect to temperature.

Figure 2.12 shows the Debye temperature of bulk Si crystal under hydrostatic compressive, uniaxial compressive, hydrostatic tensile and uniaxial tensile strains at the temperature range 200-500 K comparing to the results of the unstrained case. The Debye temperature is almost independent of temperature but shows a strong dependence on strains. Debye temperature's increase with compressive strains and its decrease with the tensile strains can be explained from the PDOS variation shown in Fig. 2.10. In addition, it's shown in the figure that with the same 2% strain, hydrostatic strains produce a larger effect on T_D than the uniaxial strains.

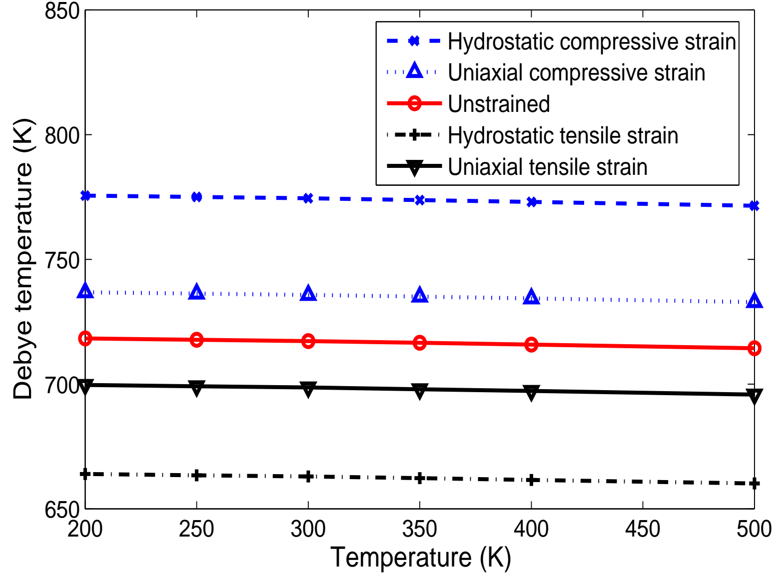

Figure 2.12: Strain dependent Debye temperature of Si between 200-500 K.

With the decrease in Grüneisen parameter and the increase in Debye temperature for compressive strains, the Slack relation given in Eq. (2.17) predicts a increase in bulk phonon thermal conductivity. Similarly, a reduction of thermal conductivity is predicted for tensile strains. Same conclusions can be obtained for Ge. Figure 2.13 shows the bulk thermal conductivity of Si with respect to temperature and strain. In Ref. [55], Slack has qualitatively explored the strain effect on bulk thermal conductivity of crystalline solids by assuming possible changes in Debye temperature and Grüneisen parameter due to strain. Our calculations have confirmed his prediction quantitatively. Figure 2.13 shows that hydrostatic strains have a stronger effect on bulk thermal conductivity than the uniaxial strains. The stars in the figure show the experiment data of unstrained bulk Si taken from Table I of Ref. [74]. The calculated unstrained bulk thermal conductivities are higher than experiment results but in reasonable agreement.

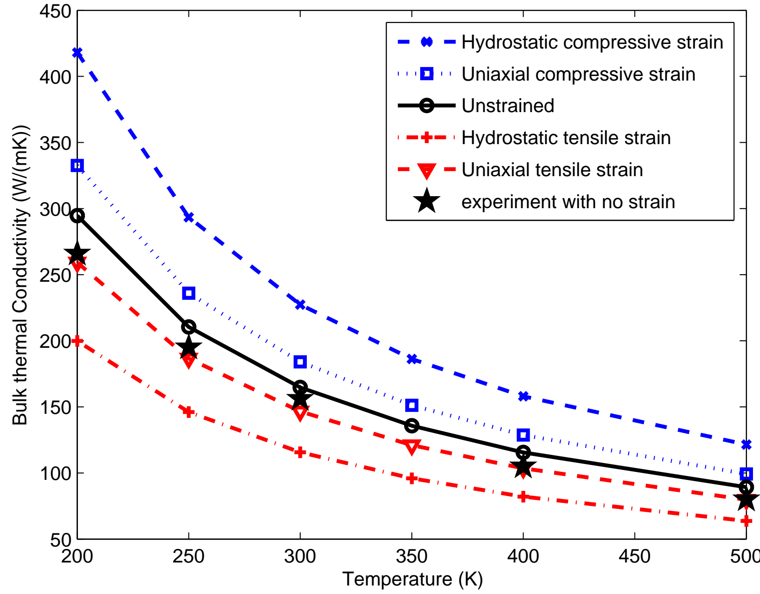

Figure 2.13: Strain dependent bulk thermal conductivity of Si between 200-500 K.

Figure 2.14 shows the contribution of optical phonons to the overall specific heat. It is shown that, at low temperatures ($T < 100K$), acoustic phonons are the major contributors to specific heat but at high temperatures ($T > 400K$), optical phonons contribute about half of the total specific heat. Similar results have been obtained in Ref. [57]. Since the optical phonons contribute little to heat transfer due to their small group velocities, it is justifiable to exclude the optical phonons in the calculation of the phonon mean free path and average group velocity as shown in Eqs. (2.26, 2.24). MD data taken from Fig. 10 of Ref. [53] and experiment data taken from Fig. 1 of Ref. [76] are also shown in Fig. 2.14. The strain and temperature dependence of the acoustic specific heat is shown in Fig. 2.15, where a compressive strain decreases the specific heat and a tensile strain increases it. Once again, the results for Ge are similar. The results are not shown for the sake of brevity.

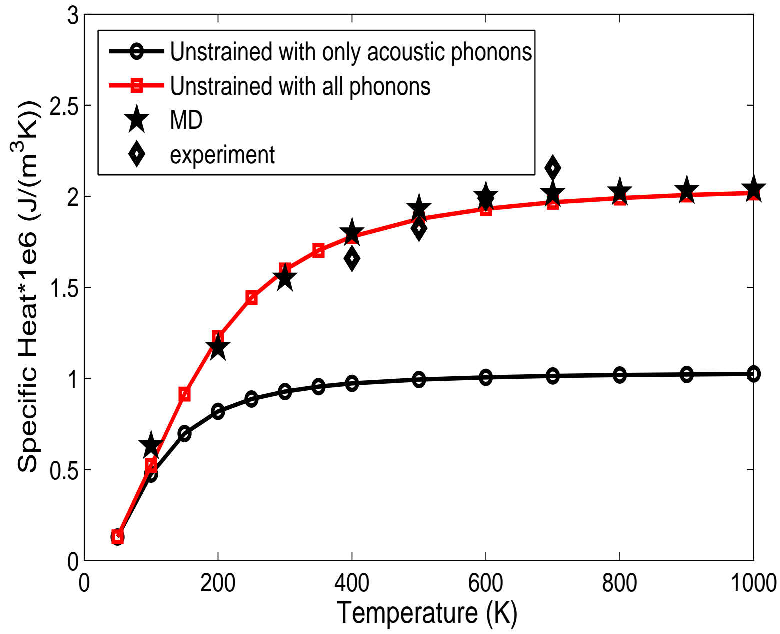

Figure 2.14: Specific heat of Si between 50-1000 K.

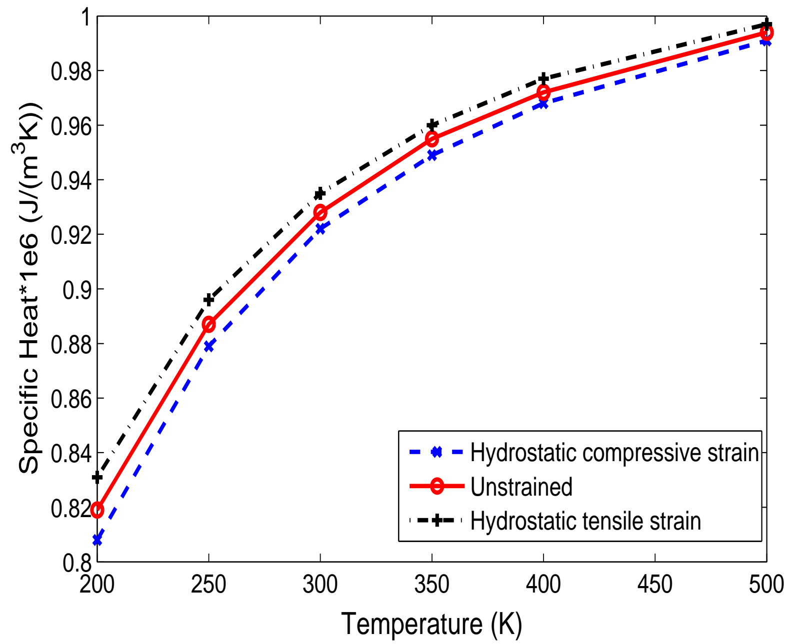

Figure 2.15: Strain effect on acoustic specific heat of Si between 200-500 K.

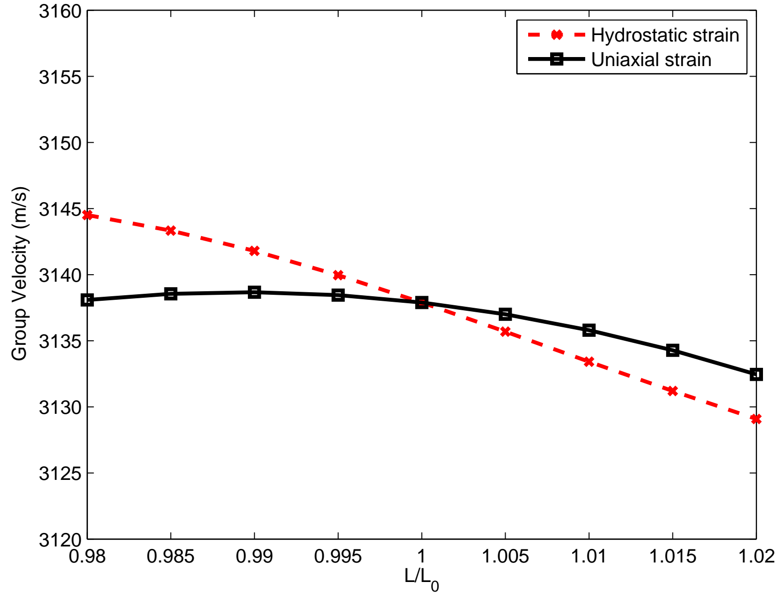

Figure 2.16: Average group velocity of Si as a function of strain in one direction (L_0 is the undeformed length).
.

Figure 2.16 shows the variation of average group velocity with respect to strain. For the small strains considered here, the group velocity shows a nearly linear dependence on the strain, for both hydrostatic and uniaxial cases. For the same 2% strain, hydrostatic strain leads to a larger variation than uniaxial strain. The group velocities of unstrained Si and Ge at room temperature are calculated to be 3143 m/s and 2233 m/s, respectively. In Ref. [9], the group velocities of Si and Ge were calculated by approximating the phonon dispersion using a simple sine function. The results are 1804 m/s for Si and 1042 m/s for Ge. It should be noted that this discrepancy is largely due to the differences in the phonon dispersion and the PDOS given by the Tersoff potential and the sine function.

Figure 2.17 shows phonon mean free path of Si with respect to strain. Bulk thermal conductivity of Si decreases with increasing temperature, further decreases

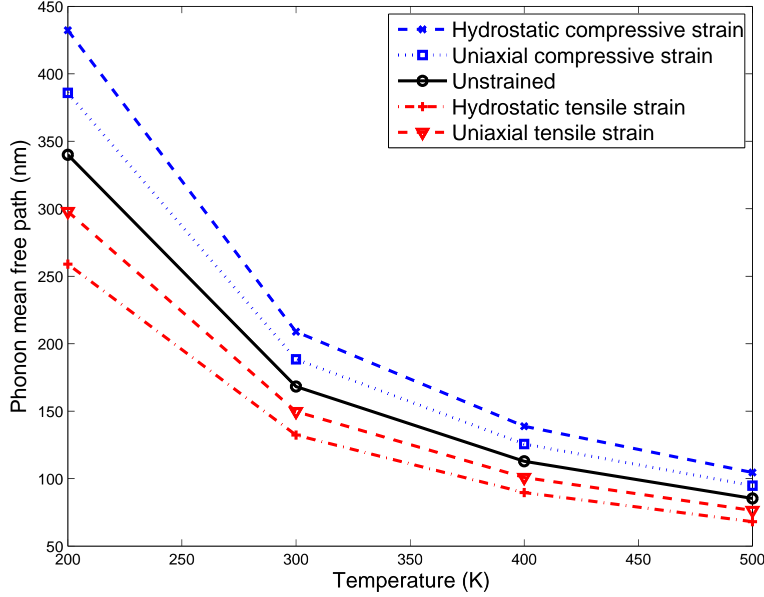

Figure 2.17: Strain dependent phonon mean free path of Si between 200-500 K.

with tensile strain applied. Acoustic specific heat increases with temperature and further increases with tensile strain applied. Strain and temperatures shows limited influence on average group velocity. Hence, from kinetic theory, phonon mean free path of Si should show the same dependence on temperature and strain as bulk thermal conductivity. Figure 2.17 confirms this prediction.

2.3.2 Strain dependent thermal conductivity of $Si_{0.2}Ge_{0.8}$ nanocomposites

Having calculated the thermal properties of bulk Si and Ge as functions of strain, the effective thermal conductivity is computed for the Si/Ge nanocomposites on unit cells as shown in Fig. 2.18 by using the FVM and solving the BTE over unstructured triangle meshes as shown in Fig. 2.6. The atomic percentage of Si is fixed at 20%, i.e.,

the nanocomposites are all $Si_{0.2}Ge_{0.8}$. In all calculations, θ is discretized uniformly into 12 angles from 0 and π while ϕ is discretized into 24 angles from 0 and 2π.

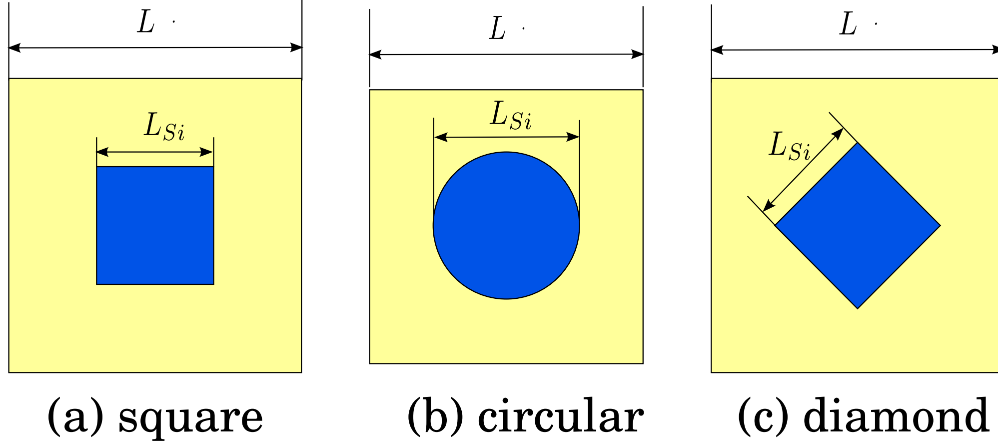

Figure 2.18: Unit cells with different cross-section shapes for $Si_{0.2}Ge_{0.8}$ nanocomposites: square, circular and diamond-shaped. L_{Si} is the characteristic length of the Si nanowire.

Figure 2.19 shows the size and temperature effects on phonon thermal conductivity of the $Si_{0.2}Ge_{0.8}$ nanocomposite with square-cross-section Si nanowires. The x-coordinate is the characteristic length of the Si nanowire, denoted as L_{Si}, which is the width of the square cross-section, as shown in Fig. 2.18 (a). Thermal conductivity of the nanocomposite decreases when the temperature increases or when size decreases. The large reduction of the thermal conductivity with the decreasing characteristic length is due to the dominance of the interface scattering over the ballistic transport in nanocomposites [9]. Figure 2.19 shows that this interface scattering induced thermal conductivity reduction holds over a wide range of temperatures while the effect is more significant at low temperatures.

The heat flux in the x-direction of the unstrained $Si_{0.2}Ge_{0.8}$ nanocomposite with

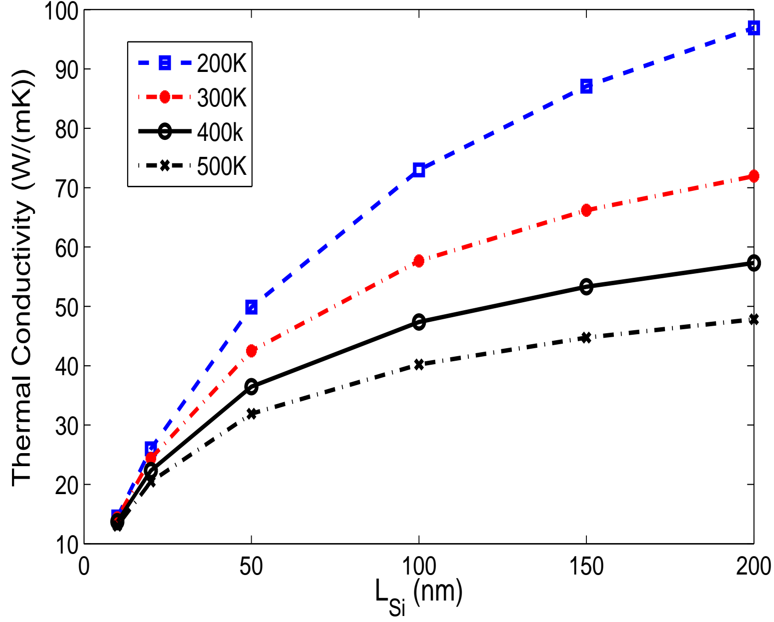

Figure 2.19: Phonon thermal conductivity of $Si_{0.2}Ge_{0.8}$ nanocomposites with respect to size and temperature (square Si nanowire cross-section).

10 nm × 10 nm Si nanowire at 300 K is shown in Fig. 2.20. The low heat flux along the path blocked by the Si wire is clearly due to the phonon scattering at the Si-Ge interface. The effect of strain along with the size effect on the effective thermal conductivity is shown in Figs. 2.21 and 2.22. It is shown that strain has a significant effect on the thermal conductivity of the nanocomposite. Depending on the characteristic length of the Si nanowire, with a strain of 2%, an applied hydrostatic tensile or compressive strain can reduce or increase the thermal conductivity up to 15%, while uniaxial tensile or compressive strain can reduce or increase the thermal conductivity by as much as 8%. More importantly, the strain effect on the thermal conductivity of bulk materials is largely preserved in the composite configuration over all the sizes. This result shows that the mechanical effect can be combined

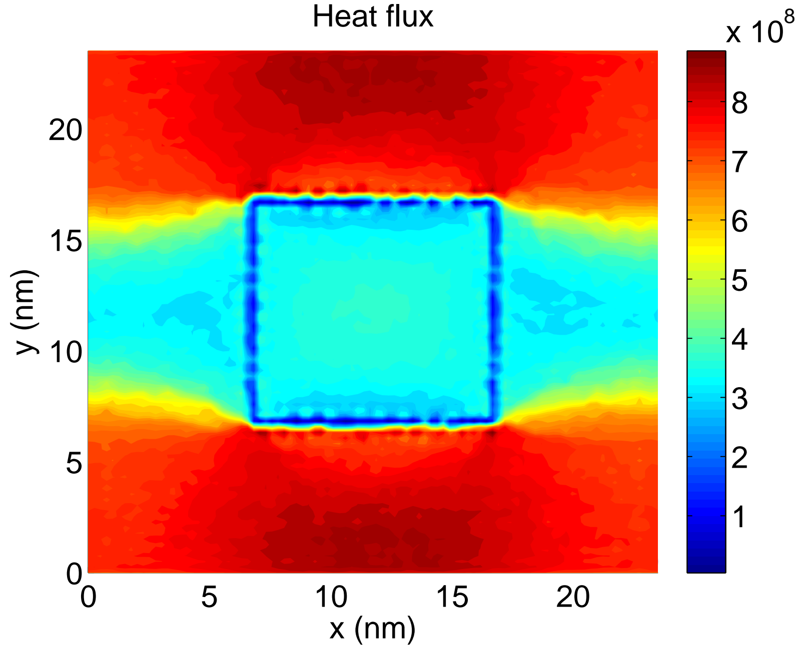

Figure 2.20: Heat flux profile of unstrained $Si_{0.2}Ge_{0.8}$ at 300 K (Si nanowire with 10 nm × 10 nm square cross-section).

with structural effects such as size and composition effects to further manipulate and control the thermal conductivity of nanomaterials and nanostructures.

If we fix the characteristic length of Si nanowire to be 10 nm but change the length of the unit cell L, we can study the content effect on phonon thermal conductivity. At 300 K, with the increase of the atomic percentage of Si, L decreases, which increases interface scattering, leading to reduced phonon thermal conductivity , as shown in Fig. 2.23.

Keeping the atomic percentage of the Si nanowire at 20%, we change the cross-sectional shape of the Si nanowire to be circular and diamond-shaped. Note that, for circular cross-sections, the characteristic length L_{Si} is the diameter and for diamond-shaped cross-sections, the characteristic length L_{Si} is the length of the edges, as shown

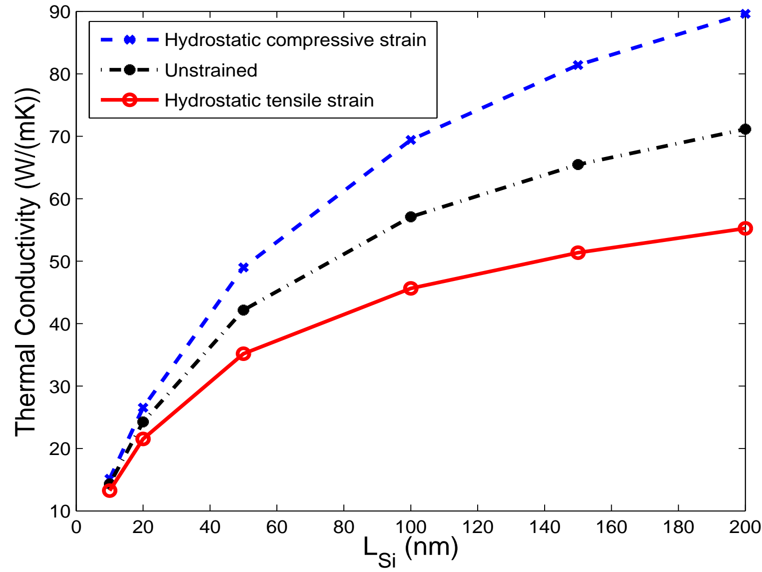

Figure 2.21: Phonon thermal conductivity of $Si_{0.2}Ge_{0.8}$ under hydrostatic strain at 300 K (square Si nanowire cross-section).

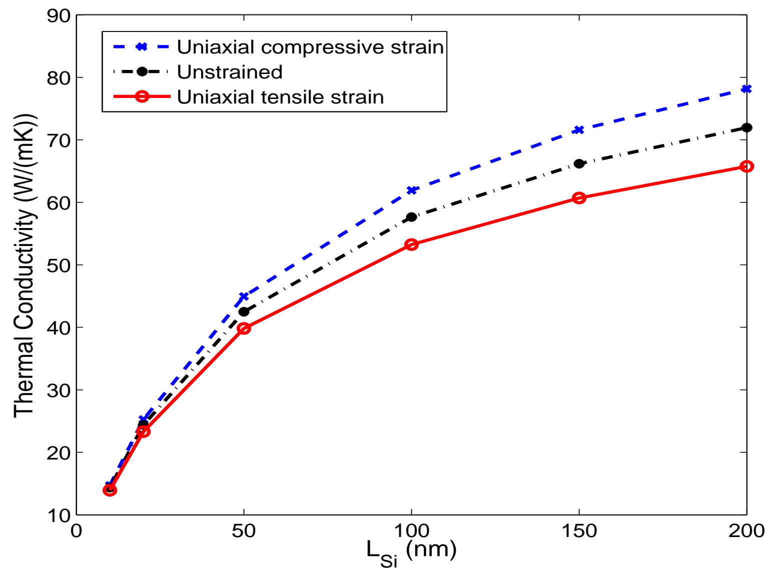

Figure 2.22: Phonon thermal conductivity of $Si_{0.2}Ge_{0.8}$ under uniaxial strain at 300 K (square Si nanowire cross-section).

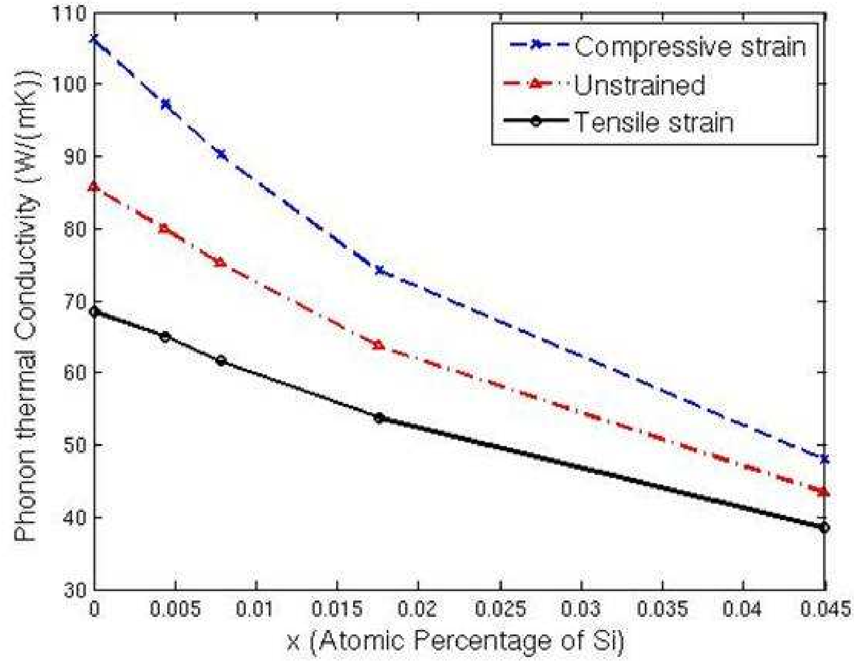

Figure 2.23: Content effect on phonon thermal conductivity of Si_xGe_{1-x} at 300 K (square Si nanowire cross-section).

in Fig. 2.18 (b) and (c). Same set of calculations are performed to obtain the strain and size effects on the effective thermal conductivity. The heat flux profiles for the diamond-shaped and circular cross-sections are shown in Figs. 2.24 and 2.25. The difference in the heat flux profiles is obvious, especially the shape of the low heat flux regions (the light colored regions).

In order to better understand the influence of cross-section shapes, we plot the effective temperature distribution for the three different unit cells, as shown in Fig. 2.26. Here effective temperature is a representative of local energy. We can clearly see jumps at the interfaces, which means local energy is not continuous at interfaces. Again, the shape of the local energy is related to their nanowire cross-section shapes.

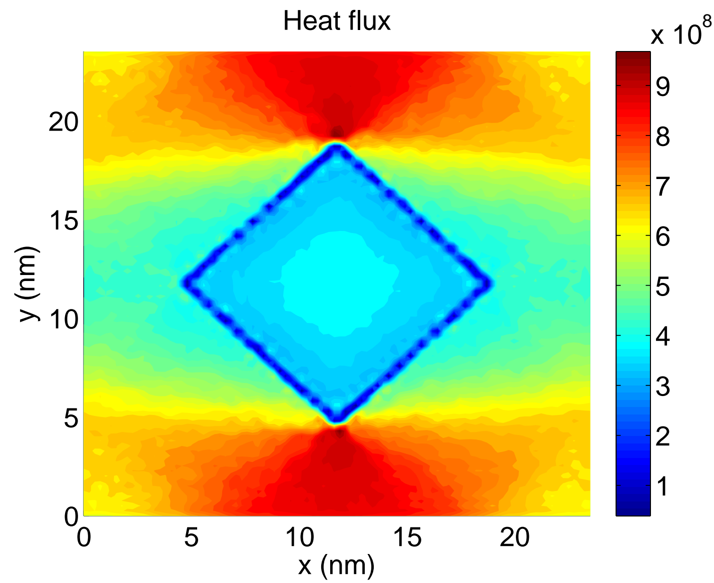

Figure 2.24: Heat flux profile of unstrained $Si_{0.2}Ge_{0.8}$ at 300 K (diamond-shaped Si nanowire cross-section with the characteristic length of 10 nm).

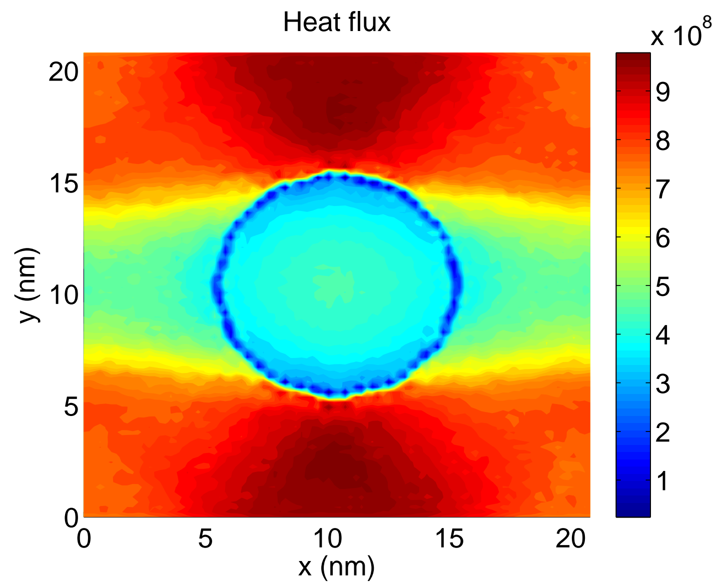

Figure 2.25: Heat flux profile of unstrained $Si_{0.2}Ge_{0.8}$ at 300 K (circular Si nanowire cross-section with the characteristic length of 10 nm).

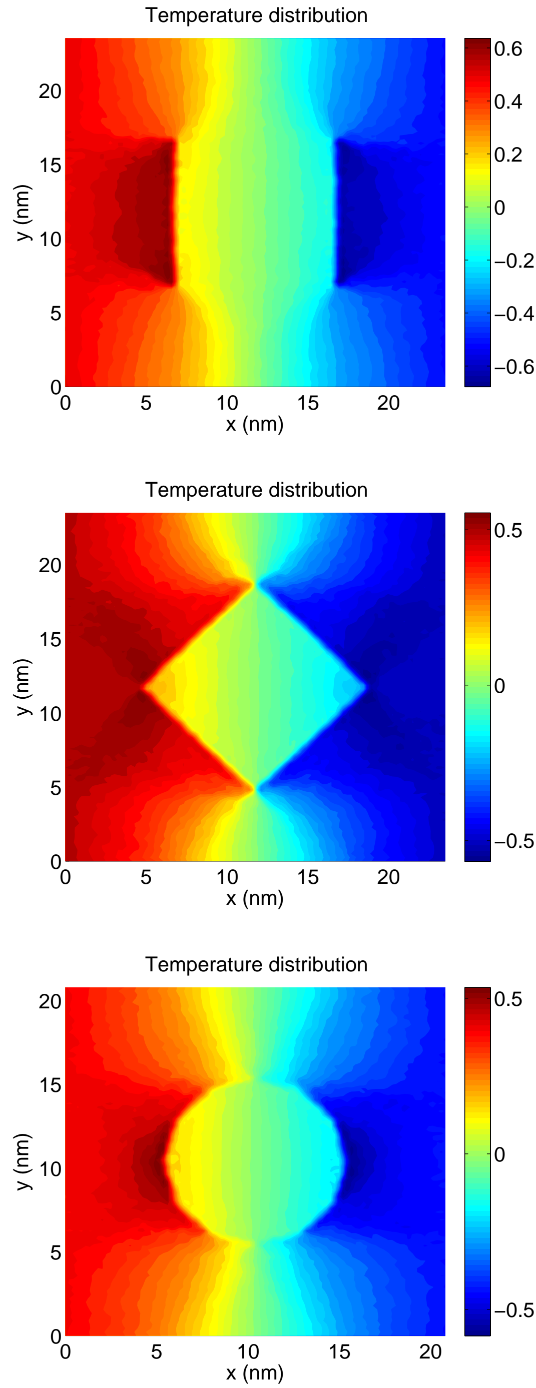

Figure 2.26: Effective temperature distribution of unstrained $Si_{0.2}Ge_{0.8}$ at 300 K ($L_{Si} = 10nm$). From top to bottom: square cross-section, diamond-shaped cross-section and circular cross-section for Si nanowire.

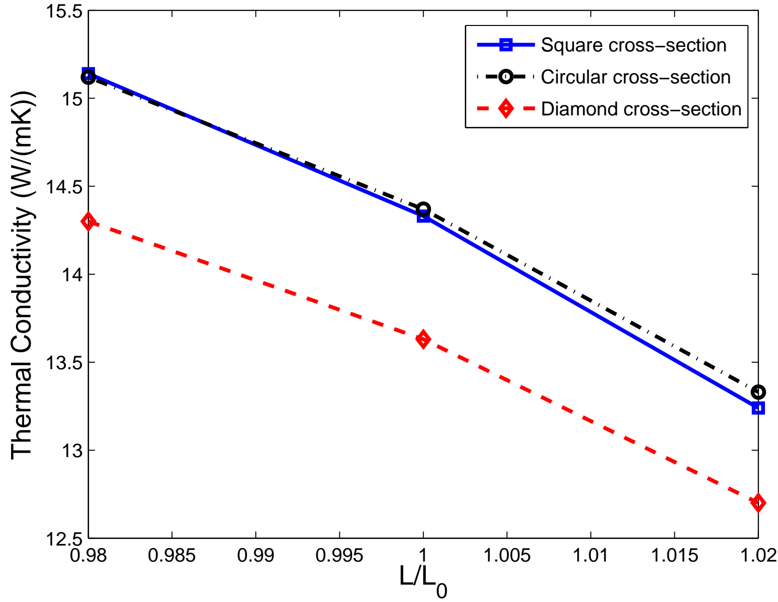

Figure 2.27: Phonon thermal conductivity of $Si_{0.2}Ge_{0.8}$ with different cross-section shapes of Si nanowire under hydrostatic strains at 300 K.

However, it is observed that the curves of the effective thermal conductivity are very similar to those shown in Figs. 2.21 and 2.22, except at the lower limit of the characteristic length. Figure 2.27 shows the thermal conductivities for the three types of Si nanowires at the characteristic length of 10 nm under hydrostatic strains at 300 K. The strain effect is almost the same for the three nanocomposites. The circular and square cases have very close thermal conductivities, with or without strain. The magnitude of the thermal conductivity for diamond-shaped cross-section is appreciably lower (about 5%). Figure 2.28 shows the difference in thermal conductivity for diamond-shaped and square cross-sections over the characteristic length from 10 nm to 200 nm. The thermal conductivity difference between the two nanocomposites drops exponentially. These results show that, with the same atomic percentage of Si, the cross-sectional shape makes little difference when the

characteristic length increases. However, for very small systems (e.g., characteristic length $< 10nm$), the cross-sectional shape starts to play a role.

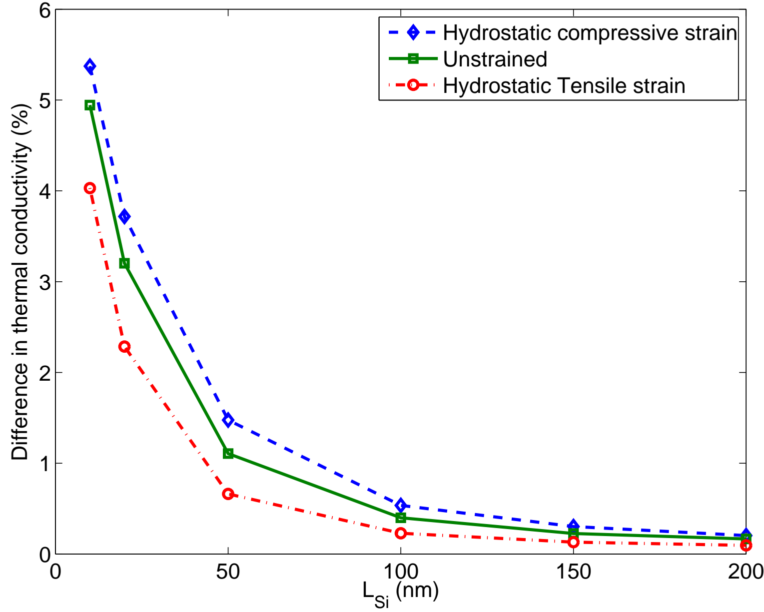

Figure 2.28: Difference in phonon thermal conductivity between diamond-shaped and square cross-sections as a function of characteristic length.

Compared with nanocomposites with square cross-section Si nanowire, corresponding nanocomposites with diamond-shaped cross-section of Si nanowire have lower phonon thermal conductivities. If we choose the diagonal length of the diamond to be the characteristic length and use the same L_{Si} and L, as shown in Fig. 2.29, another set of phonon thermal conductivities can be compared. Figure 2.30 shows phonon thermal conductivities of the unit cells described in Fig. 2.29 with L_{Si}/L to be the same as in $Si_{0.2}Ge_{0.8}$ nanocomposites with square cross-section Si nanowire. No strain is applied and the temperature is 300 K. In this case, phonon thermal conductivities of nanocomposites with diamond-shaped cross-section nanowire are larger than corresponding values of nanocomposites with

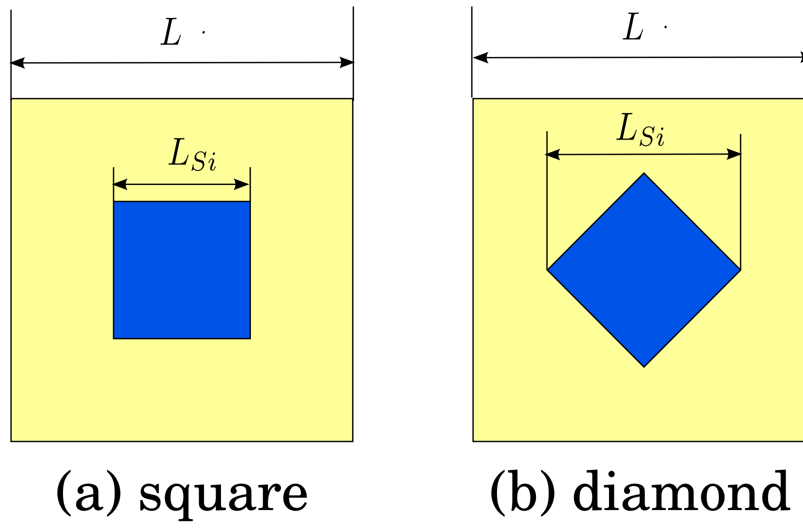

Figure 2.29: Unit cells with square and diamond cross-section shapes of Si nanowires.

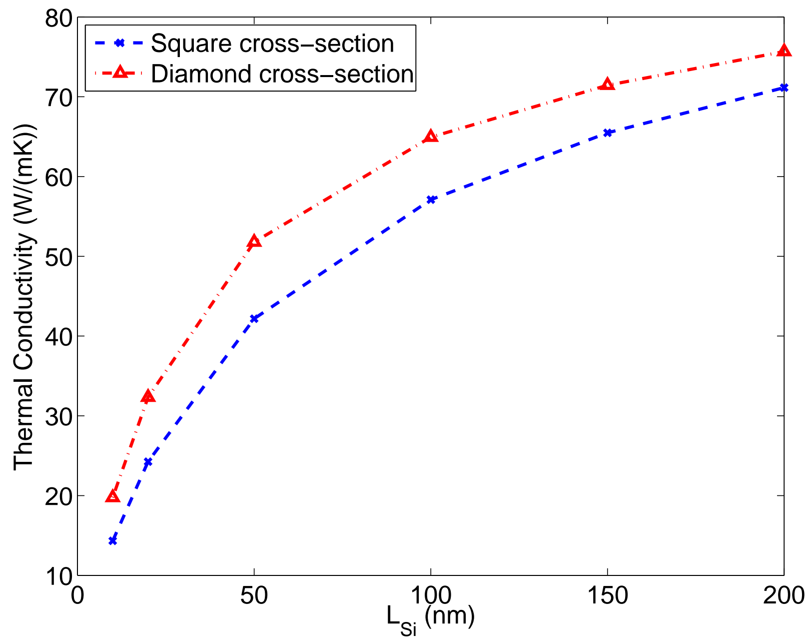

Figure 2.30: Phonon thermal conductivity of unstrained SiGe nanocomposites with square and diamond cross-section shapes of Si nanowire at 300 K.

square cross-section shape. This is because in the former one, the atomic percentage of Si is much less than 20%, resulting in smaller interface scattering and larger phonon thermal conductivity.

2.3.3 Strain dependent phonon thermal conductivity of porous nanostructures

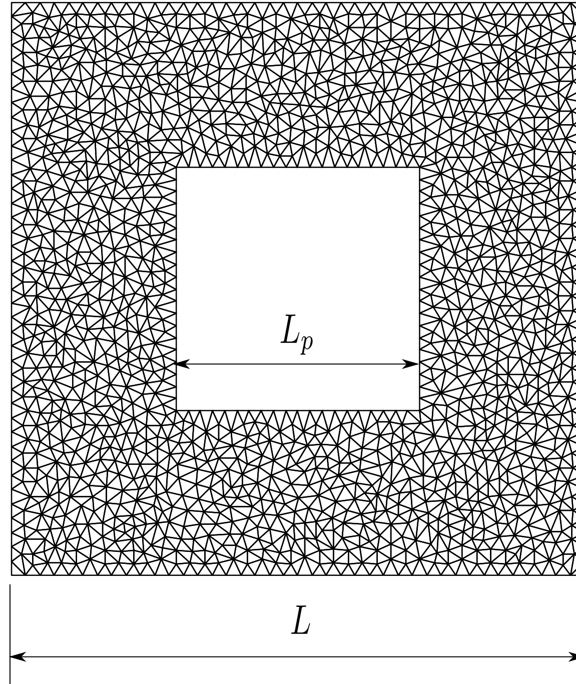

Figure 2.31: Mesh of the unit cell of a porous material.

Other than the Si/Ge nanocomposites, the BTE solver we developed can also be used to calculate phonon thermal conductivity of other materials, such as nano-porous materials. Figure 2.31 shows a mesh of the unit cell of a nano-porous material, where the center region is a nano-sized cavity. For the sake of simplicity, we use L_p to represent the characteristic length of the cavity and L to stand for the length of

the edge of the unit cell. On the boundary of the cavity, diffuse reflection of the phonons is assumed, i.e., all phonons are reflected and evenly distributed across all angles on the material side of the interface. Using the BTE solver, thermal transport properties are calculated. Figure 2.32 shows the heat flux and effective temperature distribution profiles for a nano-porous Ge material at 300 K with L_p equal to 10 nm and L_p/L equal to L_{Si}/L in the $Si_{0.2}Ge_{0.8}$ nanocomposite case. Comparing this figure with Fig. 2.20, it is shown that the heat flux along the path is more heavily blocked by the cavity. Compared with the Si/Ge nanocomposite with square nanowire cross-section shown in Fig. 2.26, the temperature drop in x direction across the cavity is slightly larger than that across the Si-Ge interfaces. The heat flux and temperature results imply a lower phonon thermal conductivity in the nano-porous material.

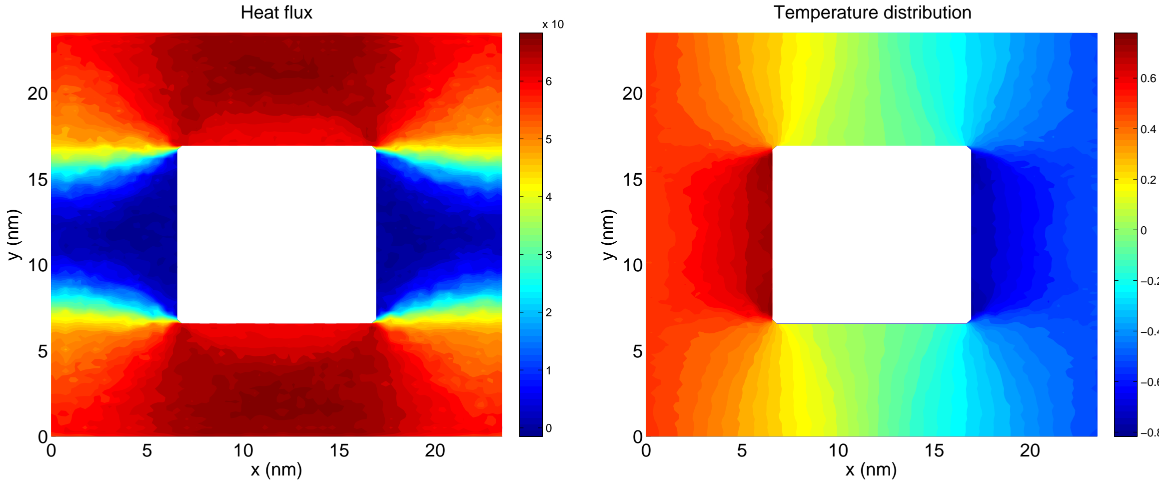

Figure 2.32: Heat flux and effective temperature distribution profiles of unstrained porous Ge at 300 K (square cross-section with the characteristic length of the cavity being 10 nm).

Figure 2.33 shows the size and temperature dependent phonon thermal conductivity of the nano-porous Ge material. Similar to $Si_{0.2}Ge_{0.8}$ nanocomposites, phonon thermal conductivity increases with size and decreases with temperature.

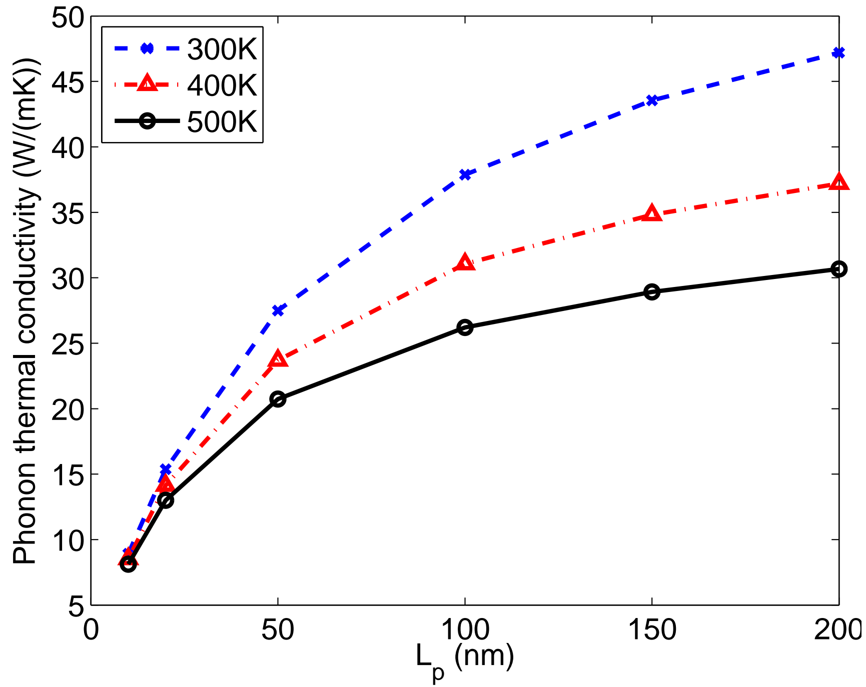

Figure 2.33: Phonon thermal conductivity of nano-porous Ge with respect to size and temperature.

Compared to those of $Si_{0.2}Ge_{0.8}$ nanocomposites shown in Fig. 2.19, phonon thermal conductivities of the nano-porous Ge materials are only about half of their counterparts. Figure 2.34 shows the different phonon thermal conductivities of porous Ge, porous Si and $Si_{0.2}Ge_{0.8}$ nanocomposites for different sizes at 300 K. Porous Si have a much larger phonon thermal conductivity compared to porous Ge with the same size. This is mostly attributed to the higher thermal conductivity of Si than that of Ge. In addition, porous Si have larger phonon thermal conductivities than corresponding $Si_{0.2}Ge_{0.8}$ nanocomposites at large sizes. This is because when the size is small, scattering due to porous and interfaces dominant but when size increases, Si's larger bulk thermal conductivity than Ge makes their difference clear.

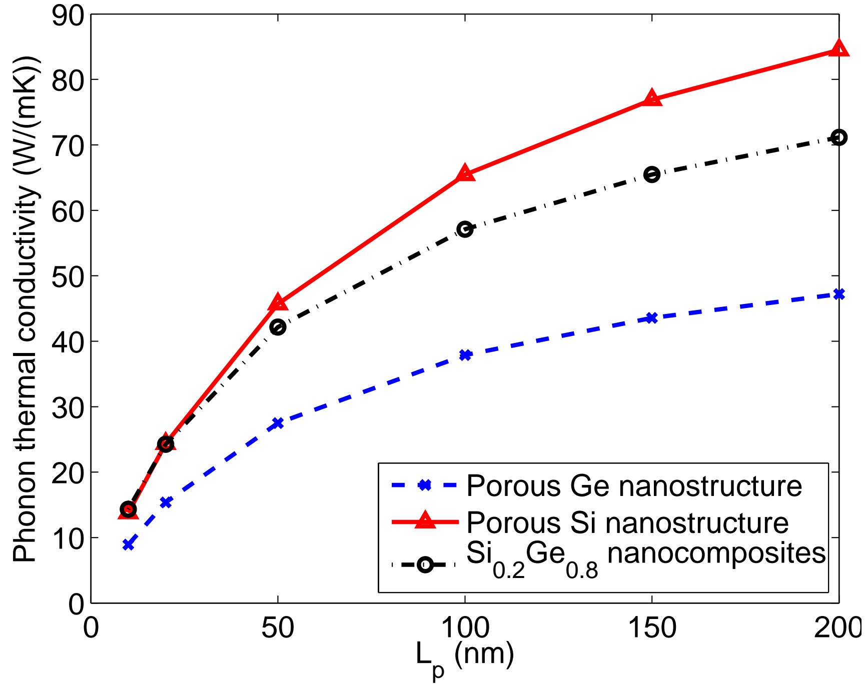

Figure 2.34: Phonon thermal conductivity of nano-porous Si and Ge compared to that of Si/Ge nanocomposites at 300 K.

2.4 Summary

A modeling and analysis approach to investigate the strain effect on the thermal transport in 2-D Si/Ge nanocomposites has been developed. Strains are incorporated into the lattice dynamics by using the Cauchy-Born rule. Thermal properties calculated from strain dependent lattice dynamics are then used in the phonon BTE for the thermal transport analysis of nanocomposites. A finite volume method is employed to solve the BTE over unstructured meshes. Our results show that the phonon thermal conductivity of the nanocomposites can be significantly decreased (or increased) by a tensile (or compressive) strain. With the same strain change, hydrostatic strain produces a larger variation in phonon thermal

conductivity than uniaxial strain. Depending on the size and shape of the embedded Si nanowire, a hydrostatic tensile strain of 2% can reduce the thermal conductivity of $Si_{0.2}Ge_{0.8}$ by as much as 15%, while a uniaxial tensile strain of 2% gives a maximum reduction of 8%. The shape effect on the thermal conductivity is also studied, it is found that with the same atomistic percentage, the cross-sectional shape makes little difference to the effective thermal conductivity except at very small characteristic lengths.

CHAPTER 3

STRAIN EFFECT ON ELECTRON TRANSPORT PROPERTIES AND ENERGY CONVERSION EFFICIENCY OF SI/GE NANOCOMPOSITES

3.1 Introduction

As discussed in Chap. 1, thermoelectric materials and devices have many promising applications [22, 23, 24, 25, 26]. They have several attractive properties, such as being pollution-free since they do not generate any harmful emissions, silent and reliable because they do not have any moving parts or vibrations, and highly portable due to their scalable modules. However, they are currently only in limited

use due to their relatively low energy conversion efficiency.

The state of the art thermoelectric cooling materials are based on alloys of Bi_2Te_3 with Sb_2Te_3 and Bi_2Te_3 with Bi_2Se_3, which can give a ZT of about 1 at room temperature [77]. State of the art thermoelectric power generation materials are PbTe and $Si_{0.8}Ge_{0.2}$, which have been used in space radioisotope thermoelectric power generators that operate at about 900 degrees with a maximum efficiency of about 7% [28]. However, $ZT \approx 4$ is required to match a conventional refrigerator for cooling and $ZT \approx 2$ is required to efficiently recover waste heat.

As already mentioned in Chap. 1, the efficiency of thermoelectric materials is evaluated by the dimensionless figure of merit defined by $ZT = S^2\sigma T/k_t$, where S, σ and T respectively denote the Seebeck coefficient, electrical conductivity and absolute temperature, while k_t represents the thermal conductivity, including contributions from phonons and electrons [27]. The key goal at thermoelectrics research is to increase ZT, but this is a challenging process because adjustment of one parameter unavoidably involves variations of others [28]. Recently, it has been reported that ZT values can be significantly improved in nanocomposites due to the largely increased interfaces, which strongly scatter phonons but only slightly influence the charge carrier transport, leading to significantly reduced phonon thermal conductivity and maintained or improved power factor $S^2\sigma$ [31, 32]. Compared to one of the state of the art thermoelectric power generation material, $Si_{0.8}Ge_{0.2}$ alloy, nanostructured Si/Ge bulk alloy leads to larger figure of merits due to the decreased phonon thermal conductivity [5, 78]. This method and others are being used to attempt to increase ZT values and create more universally viable thermoelectric nanocomposite materials. Nevertheless, in spite of these efforts, increasing ZT by a factor of 4 is still a great challenge today.

Strain can be introduced into nanocomposite materials under several conditions, such as phonon-induced lattice vibrations, lattice mismatch in nanocomposite growth and applied external mechanical force. We have performed strain analysis on phonon thermal conductivity of $Si_{0.2}Ge_{0.8}$ nanocomposites and found that tensile strain can significantly decrease the phonon thermal conductivity and shear strain has little influence. When the width of Si nanowire is 200 nm, a 2% hydrostatic tensile strain can reduce the thermal conductivity by as much as 15%, while a 2% uniaxial tensile strain gives a maximum reduction of 8% [79]. Strain effects on electron transport in Si and Ge semiconductor devices have been extensively studied and results show that strain can cause a considerable change in electron mobility [80, 81]. Carrier transport properties of nanostructured Si/Ge bulk alloys have been measured and analytically modeled [5, 78, 82]. However, to the best of our knowledge, the strain effect on electron transport properties of Si/Ge nanocomposites has not been investigated. In addition, the power factor and the thermal conductivity of Si and Ge respond differently to strain due to the different transport mechanisms of electrons and phonons. Since ZT is a combination of these physical quantities, how ZT of nanocomposites is going to respond to external strain is in fact unknown. Investigating the strain effect on ZT of nanocomposites will not only help understanding the behavior of nanocomposite thermoelectric materials under strain but also benefit the design and manufacturing of such materials.

In this chapter, we seek to investigate the influence of mechanical deformation on the electrical transport properties and the dimensionless figure of merit of Si/Ge nanocomposite thermoelectric materials. We focus on studying the effect of externally applied strains on σ, S, k_t and ZT of n-type $Si_{0.8}Ge_{0.2}$ nanocomposites. The strain dependent Seebeck coefficient and electrical conductivity of the Si/Ge nanocomposites

are calculated from analytical formulas derived from the BTE under the relaxation-time approximation with strain induced energy shift and effective mass variation, which are computed from the deformation potential theory and a two band degenerate $\mathbf{k}\cdot\mathbf{p}$ method. The strain effect on phonon thermal conductivity in the nanocomposite material is computed by using the model discussed in Chap. 2. Electronic thermal conductivities are calculated from electrical conductivities by the Wiedemann-Franz law. Then, by combining the strain effect models (phonon and electron), the strain effect on ZT of the nanocomposite materials is obtained.

3.2 Theory

It has been widely accepted that the enhancement of electrical conductivity of semiconductors under strain can be attributed to two mechanisms [83, 84]: (1) the average conductivity effective mass is reduced by carrier re-population and band warping; (2) the intervalley scattering rate is suppressed by subband splitting and change in the electron density of states (DOS). In this work, the modeling of the strain effect on the electrical conductivity of Si/Ge nanocomposites is based on the above principles.

3.2.1 The Miller index notation

The orientation and planes in crystal (Bravais) lattices can be conveniently described via Miller indices [85, 71]. The Miller indices uses three integers h, k and l to determine a family of lattice planes. The Miller indices can be determined as the inverse intercepts along the lattice vectors. To obtain the Miller index of a plane, one first defines the three lattice vectors $\mathbf{a}_1$, $\mathbf{a}_2$ and $\mathbf{a}_3$ and determines the ratio

between the points that intercept the plane and the chosen crystal lattice vectors, then calculates the reciprocals of these numbers and chooses the smallest three integers (hkl) that have a greatest common divisor of one. The result, then enclosed in brackets, is the index of the plane. Equivalently, (hkl) describes a plane intercepting the three points $\mathbf{a}_1/h$, $\mathbf{a}_2/k$, and $\mathbf{a}_3/l$, or some multiple thereof.

Another way to define Miller indices is via a point in the reciprocal lattice. Define the three primitive reciprocal lattice vectors $\mathbf{b}_1$, $\mathbf{b}_2$ and $\mathbf{b}_3$. Then the three Miller indices h, k, l in (hkl) denote planes orthogonal to the reciprocal lattice vector:

$$\mathbf{g}_{hkl} = h\mathbf{b}_1 + k\mathbf{b}_2 + l\mathbf{b}_3. \tag{3.1}$$

If the plane is parallel to the respective axis, a Miller index 0 is chosen. If a plane cuts an axis on the negative side of the origin, a negative index is used, indicated with a minus sign over or in front of the index.

Different brackets further distinguish their meanings. Round brackets, (hkl), stand for a certain plane or the vector perpendicular to the plane. Curly brackets, $\{hkl\}$, represent all planes that are equivalent to (hkl) due to the symmetry of the crystal. Square brackets, $[hkl]$ denote a given direction in the crystal. Generally, it is not perpendicular to the (hkl) plane except in cubic crystals. Similar to curly brackets, angle brackets, $\langle hkl \rangle$ mean all directions that are equivalent to the direction $[hkl]$. For example, in cubic crystals, $\langle 100 \rangle$ includes equivalent directions [100], [010], [001], $[\bar{1}00]$, $[0\bar{1}0]$, and $[00\bar{1}]$. Figure 3.1 describes planes (100), (110) and (111) in a cubic crystal.

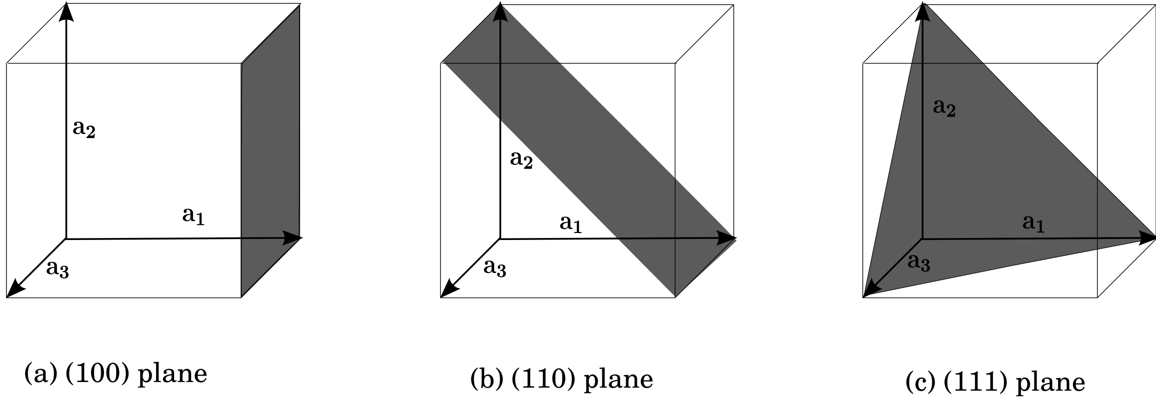

Figure 3.1: Miller indices for a cubic crystal.

3.2.2 Band structure of Si and Ge

To evaluate strain effect on electron transport in Si/Ge nanocomposites, it is first necessary to study band structures of Si and Ge under different strain conditions.

Traditionally, an energy band structure is illustrated by plotting the E-**k** diagram in the first Brillouin zone, where E is the electron energy and $\mathbf{k}$ is a wave vector. Geometrically, the first Brillouin zone is a primitive cell of the reciprocal lattice. Conventionally, it is defined as the smallest volume entirely enclosed by the perpendicular bisecting planes of the reciprocal lattice vectors drawn from the origin. As shown in Fig. 2.3, Si and Ge have diamond crystal structures, whose space lattices are face-centered cubics (FCC). The reciprocal space of FCC is a body-centered cubic (BCC) lattice and the first Brillouin zone for a FCC lattice is a truncated octahedron, as shown in Fig. 3.2. The band structure, i.e., the E-**k** diagram, describes the relation between the electron energy and wave vector $\mathbf{k}$ from the origin of the Brillouin zone to the zone edge. There are three important minima in the conduction band of Si: Γ point located at $\mathbf{k} = 0$, L point along $\langle 111 \rangle$

directions at the boundary of the first Brillouin zone and a third one near the zone boundary along ⟨100⟩ directions. The lines connecting Γ and Ł points are usually denoted by Λ. The point along ⟨100⟩ directions at the boundary is called X point and the line connecting Γ and X is called Δ-line, as displayed in Fig. 3.2.

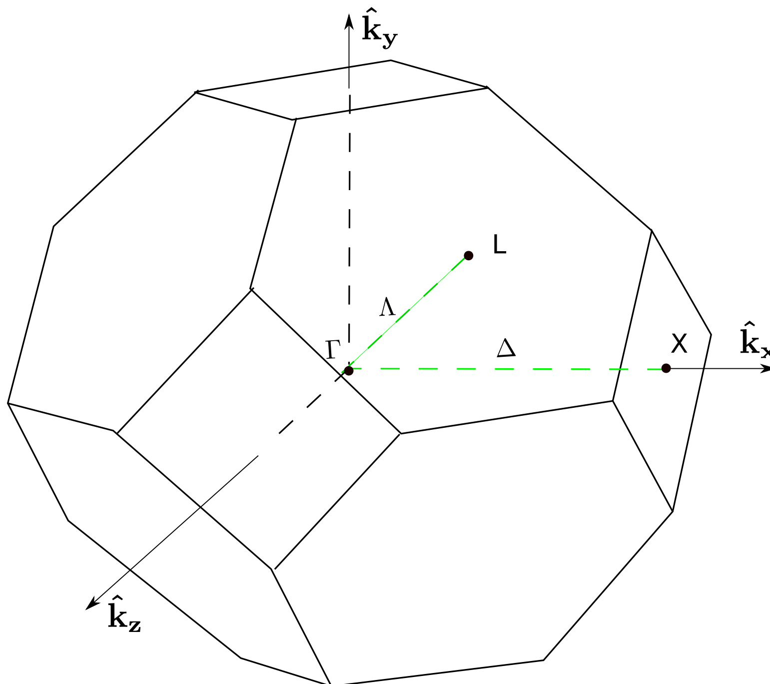

Figure 3.2: First Brillouin zone for Si and Ge.

Taking Si as an example, in unstrained n-type Si, electrons fill Δ valleys before Λ valleys. Generally, the Λ valleys can be ignored for electron transport simulations in Si at relatively low temperatures. In an unstrained Si crystal, there are six degenerate Δ valleys with the same minimum energy located near the X point at the conduction band. The distribution of electrons in these valleys can be considered the same. This is because in cubic semiconductors such as Si and Ge, the x, y, z directions are equivalent in the Brillouin zone, therefore, the energy diagrams along these directions

are the same.

However, advantageous strain reduces the symmetry of those valleys, which changes the relative population of electrons, causing subband splitting. In addition, strains along a low-symmetry axis further break crystal symmetry and result in the warping of the energy surface of subbands, leading to the effective mass variation. In short, mechanical strains cause band energy splitting and warping, resulting in the variation of the conduction band minima and effective mass, thus leading to changes on transport properties. Figure 3.3 gives a diagram of band structure change under uniaxial stress for bulk n-type Si. Figure 3.3 (a) shows the conduction band at unstrained condition. All six subbands are equivalent. Figure 3.3 (b) shows band splitting under $\langle 100 \rangle$ uniaxial tensile strain. The longitudinal tensile strain causes the $\Delta 4$ subband to shift down and the $\Delta 2$ to shift up, leading to electron re-population from the $\Delta 2$ valleys to the $\Delta 4$ valleys. Figure 3.3 (c) describes band splitting under $\langle 110 \rangle$ uniaxial tension. This kind of strain makes the $\Delta 2$ subband to shift down and the $\Delta 4$ to shift up, resulting in electron re-population from the $\Delta 4$ valleys to the $\Delta 2$ valleys. In addition to carrier re-population, uniaxial tension along $\langle 110 \rangle$ directions usually causes band warping, leading to changes of effective mass.

In unstrained Ge, the lowest conduction bands lie at L point along Λ valleys with four degenerate valleys. However, for $Si_{1-x}Ge_x$ alloys, generally the band structure and electronic properties can be modeled as Si-like with the lowest conduction minima near the X-point in the Brillouin zone for $x < 0.85$ and as Ge-like with conduction band minima at the L-point for $x > 0.85$ [86]. Further, in highly strained Ge grown on $Si_{1-x}Ge_x$ with $x < 0.40$, the conduction band minimum locates on the Δ valleys [87]. Here we assume that the lowest conduction band of $Si_{0.8}Ge_{0.2}$ nanocomposites lies at the $0.85X$ points of Δ valleys, the same as that in Si.

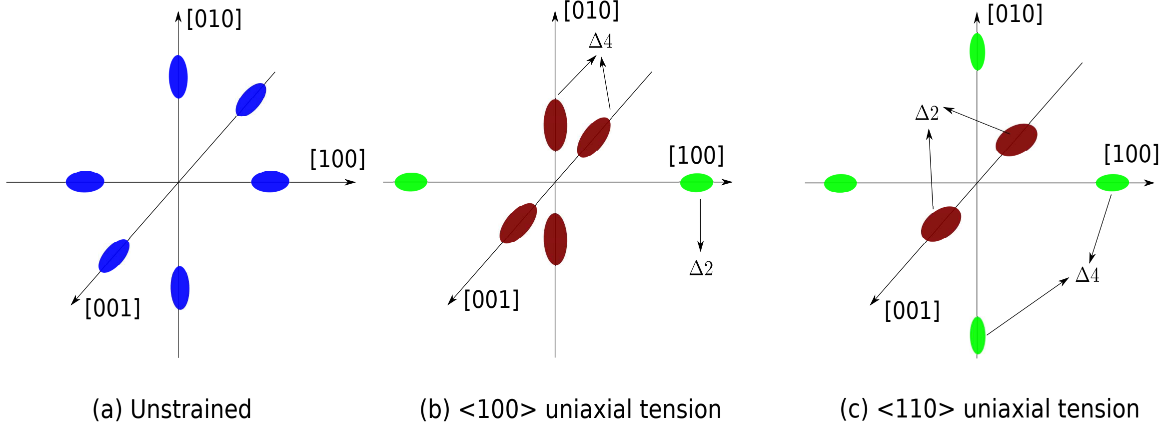

Figure 3.3: Simplified band structure change under uniaxial strain for bulk n-type Si: (a) unstrained. (b) Uniaxial $\langle 100 \rangle$ tension. (3) Uniaxial $\langle 110 \rangle$ tension.

In the calculation of electron transport properties, three coordinate systems are defined as shown in Fig. 3.4: the ellipsoidal coordinate system (ECS), the crystal coordinate system at undeformed configuration (CCSU) and the crystal coordinate system at deformed configuration (CCSD). The ECS is spanned by three unit vectors $\hat{\mathbf{k}}_{\mathbf{l}}$, $\hat{\mathbf{k}}_{\mathbf{t1}}$ and $\hat{\mathbf{k}}_{\mathbf{t2}}$ chosen along the principal axes of each energy ellipsoid. CCSU consists of lattice basis vectors $\hat{\mathbf{k}}_{\mathbf{1}}$, $\hat{\mathbf{k}}_{\mathbf{2}}$ and $\hat{\mathbf{k}}_{\mathbf{3}}$, oriented along the three orthogonal $\langle 100 \rangle$ crystallographic directions of the underlying material. The basis for CCSD is represented by three vectors $\hat{\mathbf{k}}'_{\mathbf{1}}$, $\hat{\mathbf{k}}'_{\mathbf{2}}$ and $\hat{\mathbf{k}}'_{\mathbf{3}}$ along with the three deformed axes of CCSU. Note that, the basis for CCSD is no longer unit vectors. The three coordinate systems are related to each other. The CCSU can be mapped to the CCSD by the deformation gradient $\mathbf{F}$ tensor and the CCSU can be related to the ECS in the reciprocal space. In all our simulations, the CCSU is fixed in real space, the ECS depends on the specific material and is unique to each ellipsoid, and the CCSD is unique for a given deformation gradient $\mathbf{F}$.

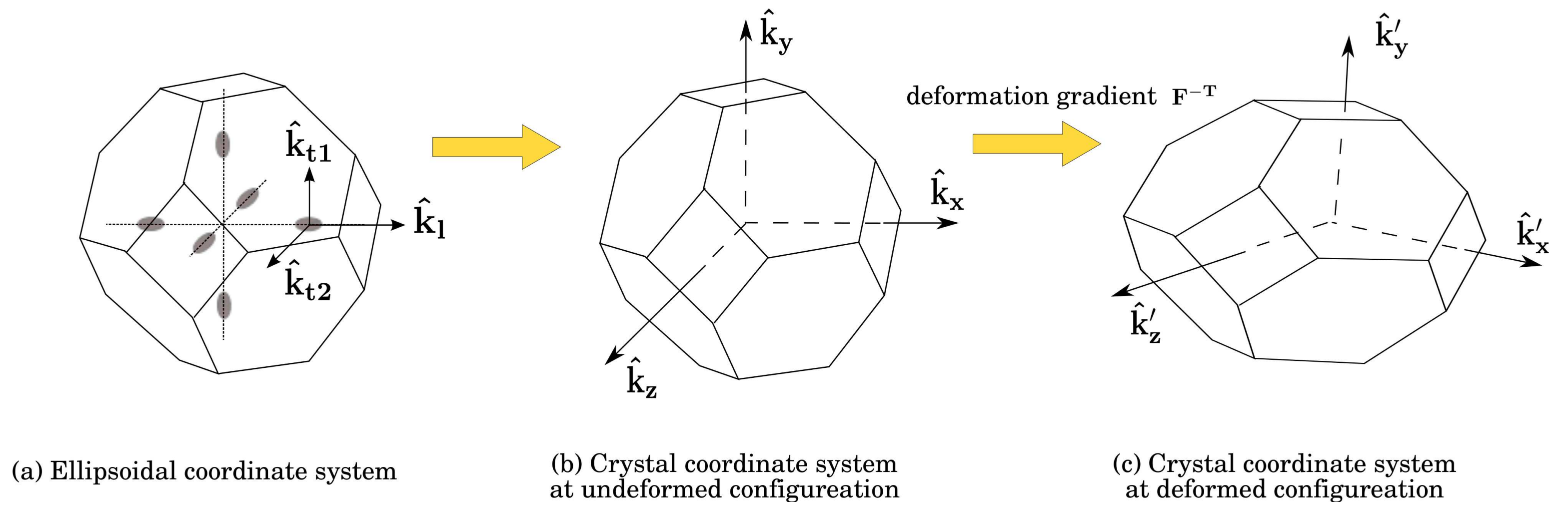

(a) Ellipsoidal coordinate system

(b) Crystal coordinate system at undeformed configureation

(c) Crystal coordinate system at deformed configureation

Figure 3.4: Coordinate systems: ellipsoidal coordinate system (ECS), crystal coordinate system at undeformed configuration (CCSU) and crystal coordinate system at deformed configuration (CCSD).

The total energy of an electron in a semiconductor, E_t, is the sum of the carrier's potential energy, E_C, and kinetic energy, E:

$$E_t = E_C + E, \tag{3.2}$$

where E_C is the conduction band minima and E is defined by

$$E(1 + \alpha E) = \frac{\hbar^2 k_l^2}{2m_l} + \frac{\hbar^2 k_{t1}^2}{2m_{t1}} + \frac{\hbar^2 k_{t2}^2}{2m_{t2}} \ , \tag{3.3}$$

in the ECS. In this equation, the nonparabolicity and anisotropicity have been accounted to increase the accuracy, $\hbar$ is the reduced Planck's constant, and k_l/k_t are longitudinal/transverse component of the wave vector.

As discussed earlier, strain usually introduces band shift and effective mass variation. Deformation potential theory was developed to describe energy shift introduced by strain. The energy shift of the n-th conduction band valley due to applied strain, ΔE_C^n, is given by [88],

$$\Delta E_C^n = \Xi_d \cdot (\varepsilon_{xx} + \varepsilon_{yy} + \varepsilon_{zz}) + \Xi_u \cdot (\hat{\mathbf{k}} \cdot \varepsilon_{ij} \cdot \hat{\mathbf{k}}) \ , \tag{3.4}$$

where Ξ_d and Ξ_u are the dilation and uniaxial-shear deformation potential of the conduction band, respectively, which can be calculated from theoretical methods or fitted by experimental results. Some of the reported values in the literature for nearly pure Si are $\Xi_{d,100} = 2.2 \pm 0.3eV$, $\Xi_u = 9.2 \pm 0.3eV$ at 295 K [88] and $\Xi_{d,100} = 2.5eV$, $\Xi_{d,111} = 5.7eV$, $\Xi_u = 9.5eV$ [89], where the subscript refers to a particular crystal direction. In Eq. (3.4), n refers to one of the six valleys, i and j represent x, y, z and $\hat{\mathbf{k}}$ is the unit vector parallel to the valley n. Note that Eq. (3.4) holds for

arbitrary stress/strain conditions. However, because the Δ valleys are along $\langle 100 \rangle$ direction, the effect of shear strains is lost in Eq. (3.4). In order to account for energy shift due to shear strain, we follow a degenerate $\mathbf{k} \cdot \mathbf{p}$ theory at the zone-boundary X point proposed by Ungersboeck et al. [90]. Note that an x-y plane shear strain ε_{xy} only shifts the band energy of z-direction valleys with the value [90],

$$\Delta E_{C,shear}^{\pm z} = \begin{cases} -\kappa^2 \varepsilon_{xy}^2 \Delta/4 \ , \ \kappa \left|\varepsilon_{xy}\right| < 1 \\ -(2\kappa \left|\varepsilon_{xy}\right| - 1)\Delta/4 \ , \ \kappa \left|\varepsilon_{xy}\right| > 1 \end{cases} , \tag{3.5}$$

where Δ is the band separation between the two lowest conduction bands of the unstrained lattice at the X point, and $\kappa = 4\Xi_{u'}/\Delta$ with $\Xi_{u'}$ being the deformation potential responsible for the band splitting of the two lowest conduction bands at the zone boundary.

From full band calculations, the effect of normal stress on effective masses can be ignored but the shear strain ε_{xy} will affect the effective masses of valleys in z-directions (Figs. 11-13 of [91]). This is because the energy surface of two-fold valleys in z-directions is warped due to ε_{xy} (Fig. 14 of [91] and Fig. 2 of [92]), which has been experimentally demonstrated using UTB (ultrathin-body) FETs (Field-effect-transistors) [91]. From the same degenerate two band $\mathbf{k} \cdot \mathbf{p}$ theory, we have [90]

$$m_{l,[001]}/m_l^* = \begin{cases} (1 - \kappa^2 \varepsilon_{xy}^2)^{-1} \ , \ \kappa \left|\varepsilon_{xy}\right| < 1 \\ (1 - 1/\kappa \left|\varepsilon_{xy}\right|)^{-1} \ , \ \kappa \left|\varepsilon_{xy}\right| > 1 \end{cases} , \tag{3.6}$$

$$m_{t,[110]}/m_t^* = \begin{cases} (1 + \eta \kappa \varepsilon_{xy})^{-1} \ , \ \kappa \left|\varepsilon_{xy}\right| < 1 \\ (1 + \eta sgn(\varepsilon_{xy}))^{-1} \ , \ \kappa \left|\varepsilon_{xy}\right| > 1 \end{cases} , \tag{3.7}$$

$$m_{t,[\bar{1}10]}/m_t^* = \begin{cases} (1 - \eta \kappa \varepsilon_{xy})^{-1} \ , \ \kappa \left|\varepsilon_{xy}\right| < 1 \\ (1 - \eta sgn(\varepsilon_{xy}))^{-1} \ , \ \kappa \left|\varepsilon_{xy}\right| > 1 \end{cases} . \tag{3.8}$$

Here sgn denotes the signum function, m_l/m_t are electron longitudinal/transverse effective mass with strain, m_l^*/m_t^* are electron longitudinal/transverse effective mass without strain, and $\eta \approx 1 - m_t^*/m_0$ [93] with m_0 being the free electron mass. Note that, when there is no shear strain, $m_l = m_l^*$ and $m_t = m_t^*$.

In addition, the nonparabolicity coefficient in the two valleys along z-direction is also influenced by ε_{xy}, i.e. [92],

$$\alpha^{\pm z} = \alpha_0 \frac{1 + 2(\eta\kappa\varepsilon_{xy})^2}{1 - (\eta\kappa\varepsilon_{xy})^2} \tag{3.9}$$

where α_0 is the nonparabolicity coefficient when no strain is applied, which is chosen to be $0.5eV^{-1}$ for intrinsic Si and $1.5eV^{-1}$ for $Si_{0.8}Ge_{0.2}$ nanocomposites when doping density is $10^{-19}cm^{-3}$.

Once again, ε_{xy} only introduces band shift, effective masses variation and nonparabolicity coefficient change of valley pairs along [001] and [00$\bar{1}$]. Similarly, ε_{yz} and ε_{zx} only influence band dispersion relations for valley pairs along [100]/[$\bar{1}$00] and [010]/[0$\bar{1}$0] respectively.

In order to show shear strain effect on subband dispersion, the in-plane energy contour of z-direction subband (solid line) with 1% of ε_{xy} shear strain is shown in Fig. 3.5. In comparison, energy contour of unstrained subbands (dashed line) is also shown here. The spacing between lines is 10 meV. It is shown that after shear strain is applied, the energy contour for z-direction subbands becomes an ellipse. Effective masses are no longer equal in [100] and [010] directions.

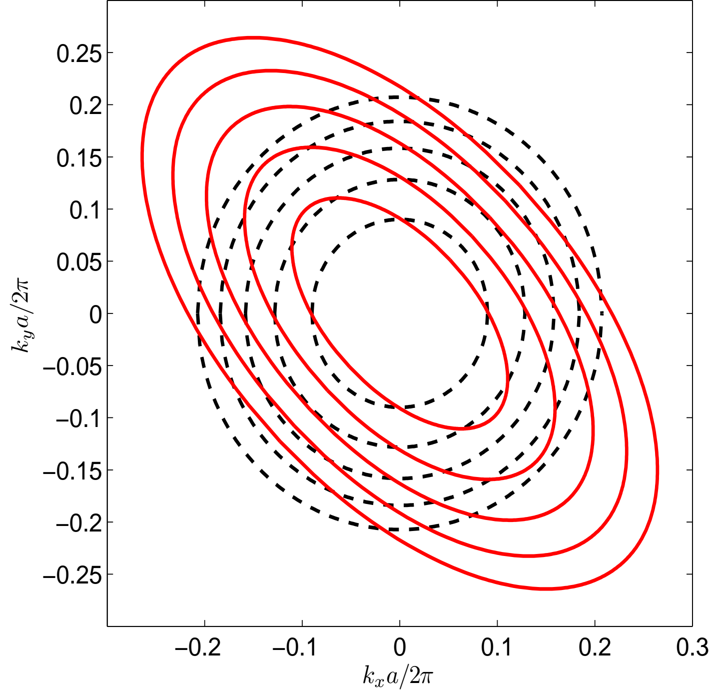

Figure 3.5: Energy contour of the Si out-of-plane subbands with 1% of shear strain (solid line) and no strain (dashed line).

3.2.3 Strain effect on electron transport of Si/Ge nanocomposites

The change of dispersion relation changes electron transport properties. The i direction electrical conductivity of the n-th valley σ_i^n can be calculated from an analytical model based on BTE under relaxation-time approximation [94]:

$$\sigma_i^n = -\frac{e^2}{3}\int_0^\infty \tau^n(E)[\upsilon_i^n(E)]^2 \frac{\partial f^n(E, E_F)}{\partial E} g^n(E_p) dE, \tag{3.10}$$

where e is the electrical carrier charge, τ is the momentum relaxation time, and υ_i^n is the group velocity of charge carriers in i direction defined by [95]

$$\upsilon_i^n = \frac{\sqrt{2E(1+\alpha^n E)}}{\sqrt{m_i^n}(1+2\alpha^n E)}, \tag{3.11}$$

with m_i^n the i-direction effective mass of n-th valley. In Eq. (3.10), f is the Fermi-Dirac distribution function defined by

$$f = \left[e^{(E+E_C-E_F)/k_BT}+1\right]^{-1}, \tag{3.12}$$

where E_F is the Fermi level calculated from [95]

$$N = \sum_n \int_0^\infty g^n(E) f^n dE, \tag{3.13}$$

with $g^n(E)$ being the density of states(DOS) for the n-th valley given by [96]

$$g^n(E) = 2\sqrt{E(1+\alpha^n E)}(1+2\alpha^n E)(m_{d1}^n)^{3/2}/(\pi^2\hbar^3). \tag{3.14}$$

where m_{d1} is DOS effective mass for valley n [96]:

$$m_{d1}^n = (m_l m_{t1} m_{t2})^{1/3}(1+2\alpha^n E). \tag{3.15}$$

Here doped Si/Ge nanocomposites are assumed to be n-type with a carrier concentration $N = 1e19cm^{-3}$. The total relaxation time is calculated by using Matthiessen's rule to combine the influences from the ionized impurity, phonon deformation potential and grain boundary (interface) scatterings mechanisms.

Ionized impurity scattering rate is calculated from [97]

$$\tau_{II}^{-1} = \frac{Ne^4\mathcal{H}(1+2\alpha E)}{16\pi\sqrt{2m_{d1}}\varepsilon^2\left[E(1+\alpha E)\right]^{2/3}}, \tag{3.16}$$

with

$$\gamma = 4k^{*2}L_D^2, \tag{3.17}$$

and

$$\mathcal{H} = ln(1+\gamma) - \frac{\gamma}{1+\gamma}, \tag{3.18}$$

where k^* is effective wave vector defined by [96]

$$k^* = \frac{\sqrt{2m_{d1}E(1+\alpha E)}}{\hbar}, \tag{3.19}$$

and L_D is screening length obtained from [98],

$$L_D = \frac{(\pi)^{2/3}\ \varepsilon^{1/2}\ \hbar}{(3N)^{1/6}\ m_{d1}^{1/2}\ e}. \tag{3.20}$$

For electron-phonon DP scattering rate, we used a model proposed in [96],

$$\tau_{DP}^{-1} = \tau_0^{-1}\left\{\left[1 - \frac{\alpha E}{1+2\alpha E}\left(1 - \frac{D_v}{D_c}\right)\right]^2 - \frac{8}{3}\frac{\alpha E(1+\alpha E)}{(1+2\alpha E)^2}\frac{D_v}{D_c}\right\}, \tag{3.21}$$

with

$$\tau_0^{-1} = \frac{\pi\ k_BT\ D_c^2\ g(E)}{\hbar\ K}. \tag{3.22}$$

For grain boundary scattering rate, a model proposed in [82] is used, i.e.,

$$\tau_{GB}^{-1} = 8\pi^2 U_0^2 z_0^2 r_0^4 g(E) N_g \mathcal{I}/\hbar, \tag{3.23}$$

with number density of interface N_g being $N_g = 4\ L_{Ge}/(\pi\ r_0^2\ L_{Si}^2)$ and $\mathcal{I}$ being Eq. (22) in reference [82]. Other parameters can be found in Table 3.1.

Table 3.1: Parameters used to calculate electron transport properties for n-type Si and $Si_{1-x}Ge_x$ nanocomposites.

m_l^*/m_0[86]	$0.92(1-x)+0.80x-0.183(1-x)x$
m_t^*/m_0[86]	$0.19(1-x)+0.20x-0.183(1-x)x$
E_d[86]	$1.1+3.4x(eV)$
E_u[86]	$9.29+0.71x(eV)$
$E_{u'}$[86]	$7.0+11.5x(eV)$
Δ[90]	$0.53(eV)$
Low frequency permittivity[86]	$\varepsilon=(11.7+4.5x)\varepsilon_0$ ‡
Electron/hole deformation potential[97]	$D_c=9.0eV, D_v=5.0eV$
Bulk modulus[86]	$K=97.9-22.8x(GPa)$
Grain boundary potential parameters[82]	$U_0=45meV, z_0=2.0nm, r_0=1.0nm$

‡ ε_0: vacuum permittivity .

The conductivity calculated in the valley ECS has to be transformed to the CCSD by a transformation matrix C with the relation $\hat{\mathbf{k}}_{\mathbf{D}} = C^n\hat{\mathbf{k}}_{\mathbf{E}}^{\mathbf{n}}$, where $\hat{\mathbf{k}}_{\mathbf{D}} = (\hat{\mathbf{k}}_{\mathbf{1}}'\ \hat{\mathbf{k}}_{\mathbf{2}}'\ \hat{\mathbf{k}}_{\mathbf{3}}')^{\mathbf{T}}$ and $\hat{\mathbf{k}}_{\mathbf{E}}^{\mathbf{n}} = (\hat{\mathbf{k}}_{\mathbf{l}}\ \hat{\mathbf{k}}_{\mathbf{t1}}\ \hat{\mathbf{k}}_{\mathbf{t2}})^T$ represent vectors in the axes of the CCSD and n-th valley ECS, individually.

The direct relation between ECS to CCSD depends on the material under consideration. For a given conduction band ellipsoid in a given material, the unit

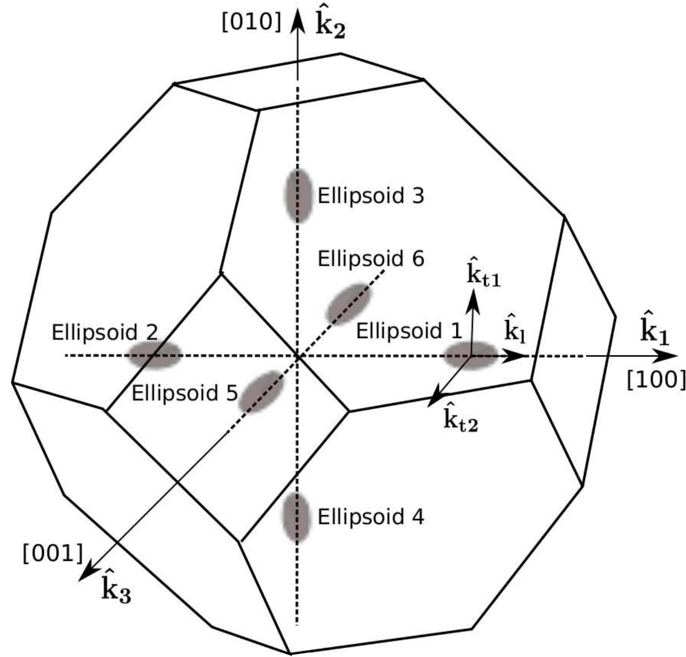

Figure 3.6: Conduction band constant energy ellipsoids along Δ for Si.

basis vector $\hat{\mathbf{k}}_\mathbf{l}$, $\hat{\mathbf{k}}_\mathbf{t1}$ and $\hat{\mathbf{k}}_\mathbf{t2}$ in the ECS can be expressed in the CCSU, thus forms a rotation matrix $\Re_{E\leftarrow U}$, which transforms the components of the unit wave vector $\hat{\mathbf{k}}_\mathbf{U} = (\hat{\mathbf{k}}_\mathbf{1}\ \hat{\mathbf{k}}_\mathbf{2}\ \hat{\mathbf{k}}_\mathbf{3})^T$ in CCSU to $\hat{\mathbf{k}}_\mathbf{E}^\mathbf{n}$ in ECS. Different ellipsoid transformation matrices have been shown in [99] for sixfold-degenerate Δ and the eightfold-degenerate Λ valleys. For Si, there are six degenerate constant energy Δ valley conduction band ellipsoids, as shown in Fig. 3.6. The basis vectors are unique for each ellipsoid in the ECS, with $\hat{\mathbf{k}}_\mathbf{l}$ along the major axis and $\hat{\mathbf{k}}_\mathbf{t1}, \hat{\mathbf{k}}_\mathbf{t2}$ perpendicular to it. There is a unique transformation matrix $\Re_{E\leftarrow U}$ for each ellipsoid, with the rows coming from the components of $\hat{\mathbf{k}}_\mathbf{l}$, $\hat{\mathbf{k}}_\mathbf{t1}$ and $\hat{\mathbf{k}}_\mathbf{t2}$. For instance, for ellipsoid 1 in Fig. 3.6, $\hat{\mathbf{k}}_\mathbf{l} = (1\ 0\ 0)$, $\hat{\mathbf{k}}_\mathbf{t1} = (0\ 1\ 0)$ and $\hat{\mathbf{k}}_\mathbf{t2} = (0\ 0\ 1)$,

thus,

$$\Re^{\Delta_1}_{E\leftarrow U} = \begin{bmatrix} 1 & 0 & 0 \\ 0 & 1 & 0 \\ 0 & 0 & 1 \end{bmatrix}. \tag{3.24}$$

Transformation matrix for other ellipsoids can be obtained similarly.

Having determined $\Re_{E\leftarrow U}$, for a crystal lattice under deformation, a rotation matrix $\Re_{U\leftarrow D}$, which transforms $\hat{\mathbf{k}}_{\mathbf{D}}$ in CCSD to $\hat{\mathbf{k}}_{\mathbf{U}}$ in CCSU, is determined by using the deformation gradient tensor $\mathbf{F}$,

$$\Re_{U\leftarrow D} = \mathbf{F}^T. \tag{3.25}$$

Accordingly, the relation between wave vectors in CCSD and ECS is obtained as,

$$\hat{\mathbf{k}}^{\mathbf{n}}_{\mathbf{E}} = \Re_{E\leftarrow U}\Re_{U\leftarrow D}\hat{\mathbf{k}}_{\mathbf{D}}. \tag{3.26}$$

Then we will have $C^n = \Re^{-1}_{U\leftarrow D}\Re^{-1}_{E\leftarrow U}$.

The total conductivity is the summation of conductivities from all the six valleys [81],

$$\sigma_{ij} = \sum_{n}^{6}\sum_{p}^{3} c^n_{ip}\sigma^n_p \left[c^n_{pj}\right]^{-1} , \tag{3.27}$$

where c^n_{ip} and $\left[c^n_{pj}\right]^{-1}$ are components of C^n and its inverse matrices.

The Seebeck coefficient is defined by

$$S_{ij} = \frac{\sum_n^6 \sum_p^3 c_{ip}^n S_p^n \sigma_p^n [c_{pj}^n]^{-1}}{\sigma_{ij}}, \tag{3.28}$$

with

$$S_i^n = -\frac{1}{eT} \frac{\int_0^\infty \tau^n(E)[\upsilon_i^n(E)]^2 \frac{\partial f^n(E,E_F)}{\partial E}(E - E_F) g^n(E) dE}{\int_0^\infty \tau^n(E)[\upsilon_i^n(E)]^2 \frac{\partial f^n(E,E_F)}{\partial E} g^n(E) dE}. \tag{3.29}$$

3.2.4 Strain effect on thermal transport of Si/Ge nanocomposites

For strain effects on phonon thermal transport of SiGe nanocomposites, we use the model described in Chap. 2. The only difference is the 2-D unit cell. Here we study Ge-nanowire Si-host nanocomposite materials and a unit cell is shown in Fig. 3.7. Ge nanowires are assumed to be uniformly distributed, so the BTE can be solved to obtain phonon intensities by finite volume method on this 2-D unit cell of the nanocomposites with periodic boundary conditions and a diffuse mismatch interface model. The edge length of the unit cell is set to be L_{Si} and the edge length of Ge nanowire is set to be L_{Ge}.

The electronic thermal conductivity, k_e, is calculated from the Wiedemann-Franz law, $k_e = \sigma L_z T$, where L_z is the Lorenz number. For metals, $L_z = 2.45 \times 10^{-8} W\Omega K^{-2}$. However, L_z depends on doping for semiconductors [94]. Here we assume the nanocomposites are heavily doped. In this case, the semiconductors become metal-like and L_z for metals is used.

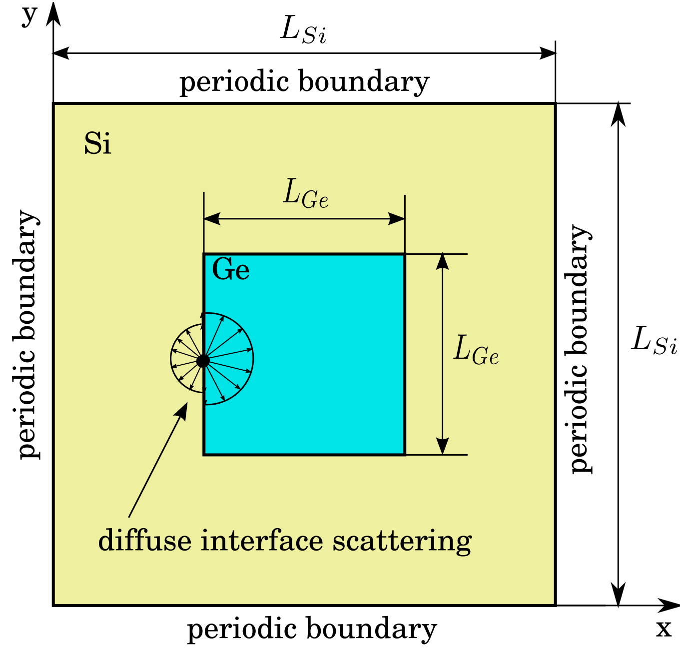

Figure 3.7: $Si_{1-x}Ge_x$ unit cell.

3.2.5 Strain effect on ZT of Si/Ge nanocomposites

Having obtained strain dependent phonon thermal conductivity and electrical properties, the calculation of dimensionless figure of merit of nanocomposite thermoelectric materials is straightforward, i.e., $ZT = S^2\sigma T/(k_p + k_e)$.

3.3 Results and Discussion

3.3.1 Thermoelectric properties of $Si_{0.8}Ge_{0.2}$ nanocomposites

This section investigates the strain effect on electrical properties of bulk Si and $Si_{1-x}Ge_x$ nanocomposites. As a validation of the electrical conductivity model described in Chap. 3.2.3, electrical conductivities of $Si_{0.7}Ge_{0.3}$ alloy and $Si_{0.8}Ge_{0.2}$

nanocomposites are computed as functions of temperature. The comparison of the obtained results with available experimental data is shown in Fig. 3.8. Experiment data for $Si_{0.7}Ge_{0.3}$ alloy and $Si_{0.8}Ge_{0.2}$ nanocomposites are obtained from [100] and [82], respectively. The computational results show a good agreement with the experiment data.

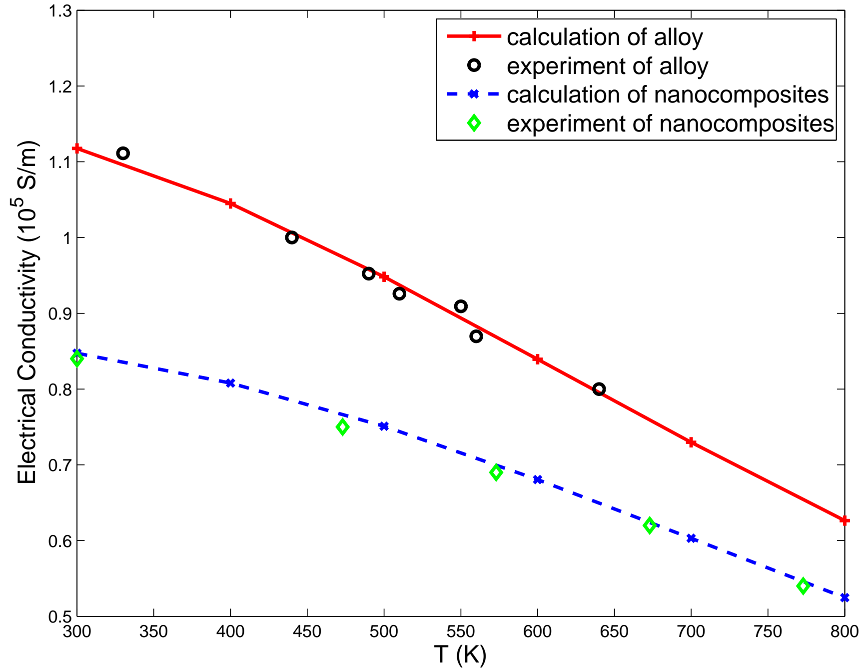

Figure 3.8: Temperature dependent electrical conductivity of $Si_{0.7}Ge_{0.3}$ alloy and $Si_{0.8}Ge_{0.2}$ nanocomposites.

The strain effect on electrical conductivity is verified by comparing the electron mobility of intrinsic Si for [100] uniaxial strain with data from [90], as shown in Fig. 3.9. Results here are not exactly the same with the results shown in [90] but they show similar dependence on strain. The difference comes from the different modeling tools and different scattering mechanisms considered. Our results are based on an analytical formula derived from BTE with several fitting parameters. Their results

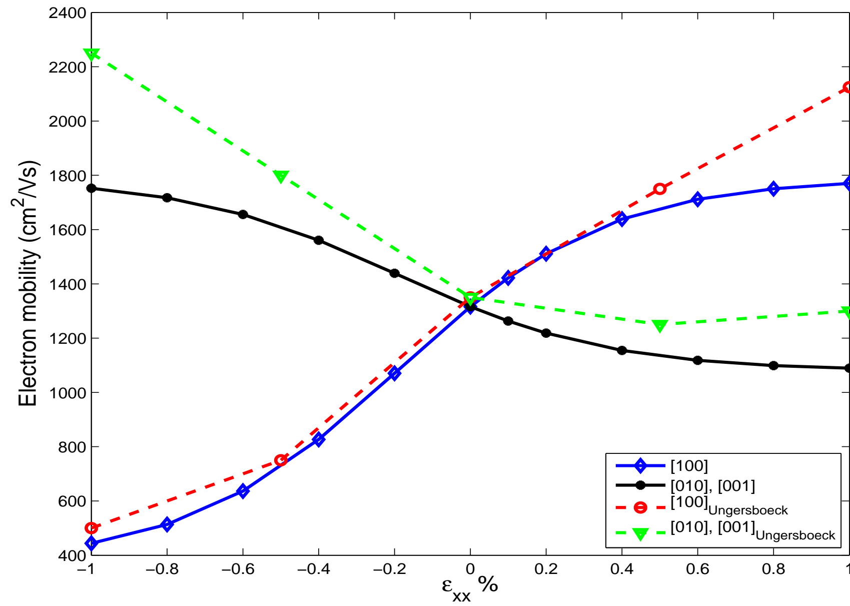

Figure 3.9: Bulk electron mobility of intrinsic Si as a function of strain for stress direction along [100].

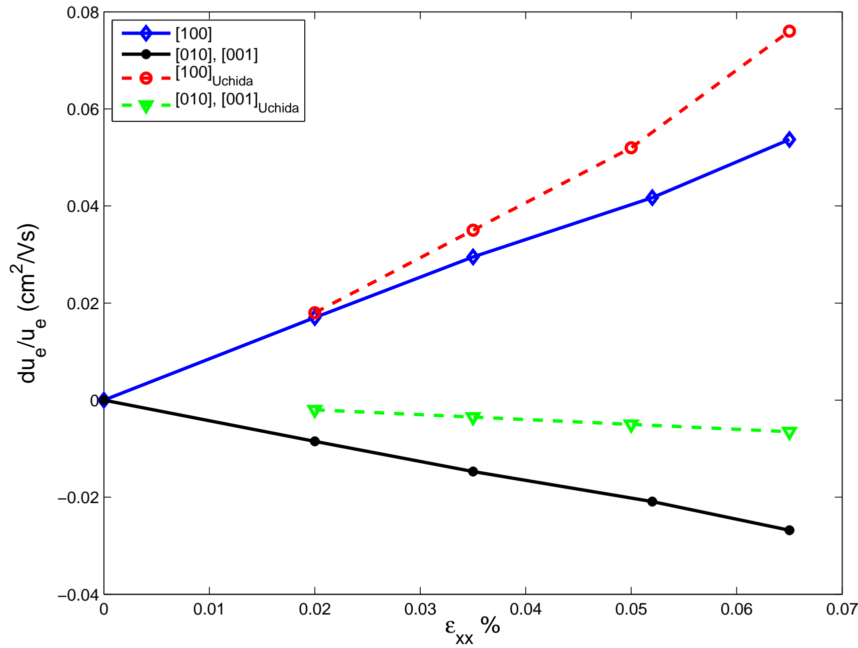

Figure 3.10: Electron mobility enhancement of intrinsic Si as a function of strain for stress direction along [100].

were calculated numerically by solving the semiclassical BTE using an MC method. We considered ionized impurity and phonon deformation potential scatterings but their models contained ionized impurity scattering, phonon scattering, alloy scattering and impact ionization scattering. Figure 3.10 shows electron mobility enhancement of intrinsic Si as a function of strain for stress direction along [100] calculated from our model and experiment results obtained from [91]. Our results show similar trends as experimental data. And Fig. 3.11 shows electron mobility enhancement of Si as a function of strain introduced by $\langle 100 \rangle$ tension. Experimental data is obtained from [91] and our results show good match with them. From the three figures, we find out that uniaxial tensile strain along $\langle 100 \rangle$ direction increases electron mobility in the same direction but decreases them in the two perpendicular directions, which implies possible change in power factor.

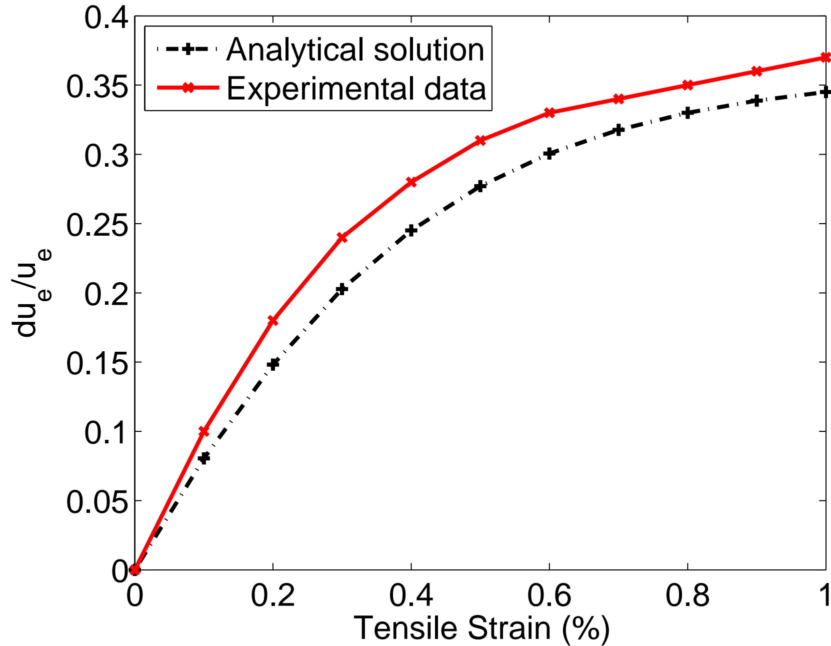

Figure 3.11: Electron mobility enhancement as a function of $\langle 100 \rangle$ tension.

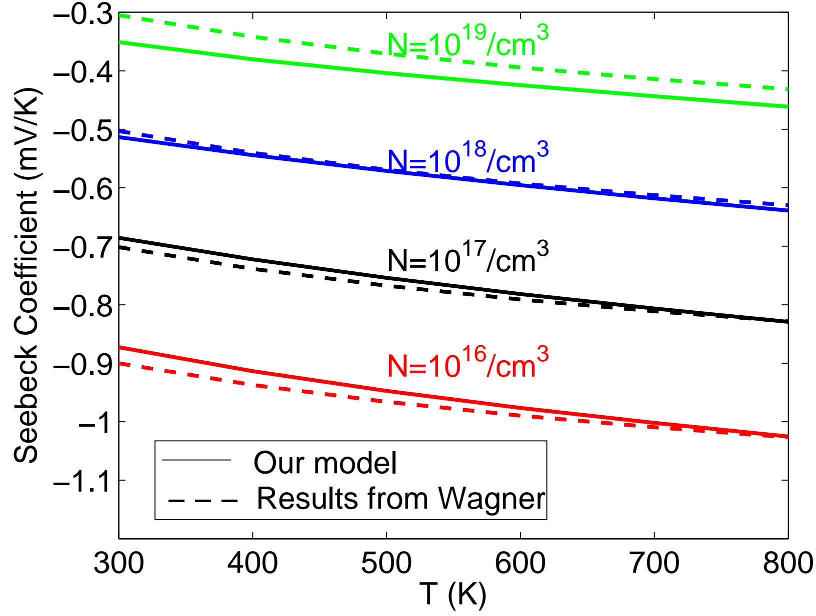

Figure 3.12: Seebeck coefficient of Si.

Seebeck coefficient of unstrained bulk Si is shown in Fig. 3.12. Solid lines are Seebeck coefficient calculated from our model and dashed lines are from Fig. 3.8 of [101]. For doping density from $10^{16}/cm^3$ to $10^{19}/cm^3$, our model matches well with Wagner's model. The results indicate that Seebeck coefficient decreases with increasing temperature, and further decreases with decreasing doping density.

3.3.2 Strain effect on figure of merit of $Si_{0.8}Ge_{0.2}$ nanocomposites

Three types of strains have been studied on the $Si_{0.8}Ge_{0.2}$ nanocomposites with the length of Ge nanowire, L_{Ge}, to be 10 nm, 15 nm and 20 nm: (1) 1% uniaxial strain in $\langle 100 \rangle$ direction; (2) 1% shear strain on (001) plane; (3) 1% biaxial normal strain in

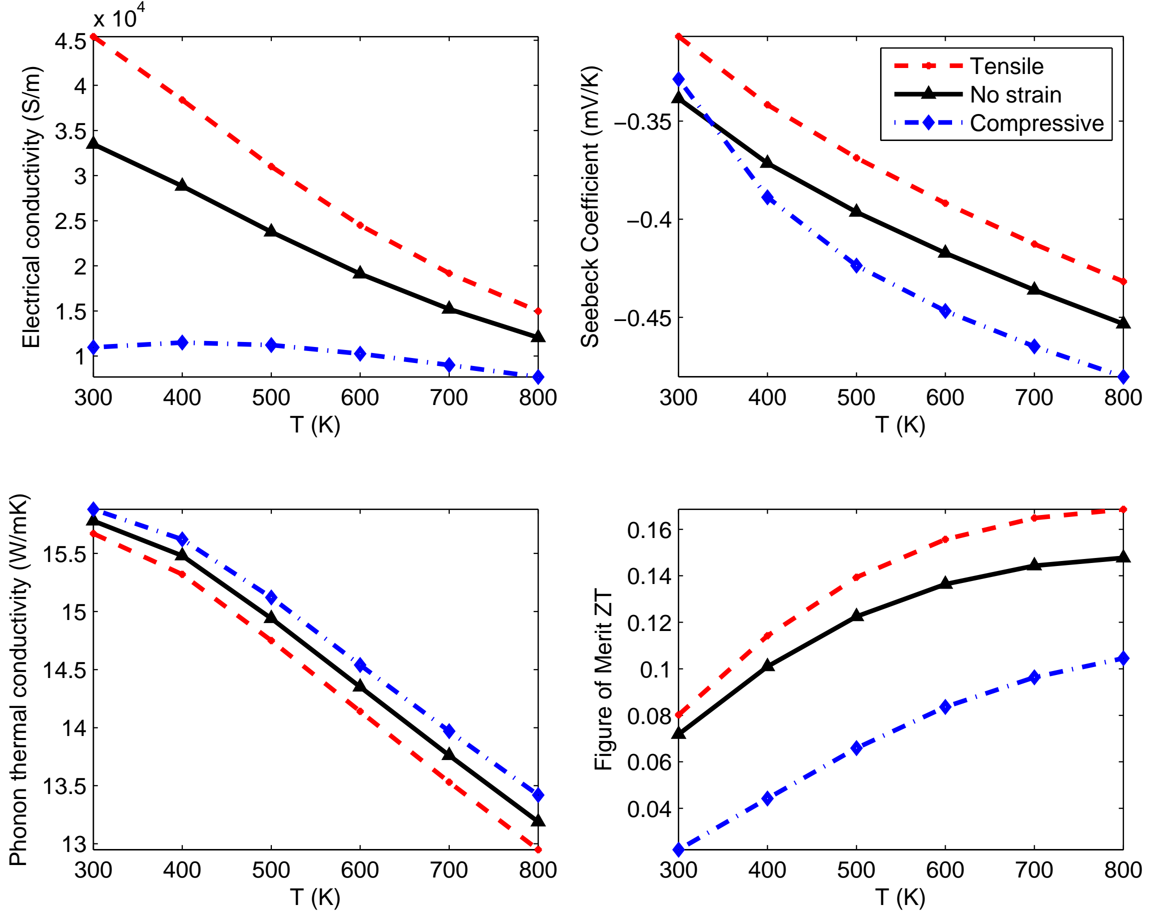

Figure 3.13: Thermoelectric properties of $Si_{0.8}Ge_{0.2}$ under uniaxial strain when $L_{Ge} = 10nm$.

[100] and [010] directions. The calculated Seebeck coefficient, electrical conductivity, phonon thermal conductivity and figure of merit are shown in Figs. 3.13-3.15 for $L_{Ge} = 10nm$, Figs. 3.16-3.18 for $L_{Ge} = 15nm$ and Figs. 3.19-3.21 for $L_{Ge} = 20nm$.

For the three nanowire sizes, as shown in Figs. 3.13, 3.16 and 3.19, uniaxial tensile strain along $\langle 100 \rangle$ direction increases electrical conductivity but decreases Seebeck coefficient and thermal conductivity along the direction in which the force is applied. Even though the decreased Seebeck coefficient somehow cancels the

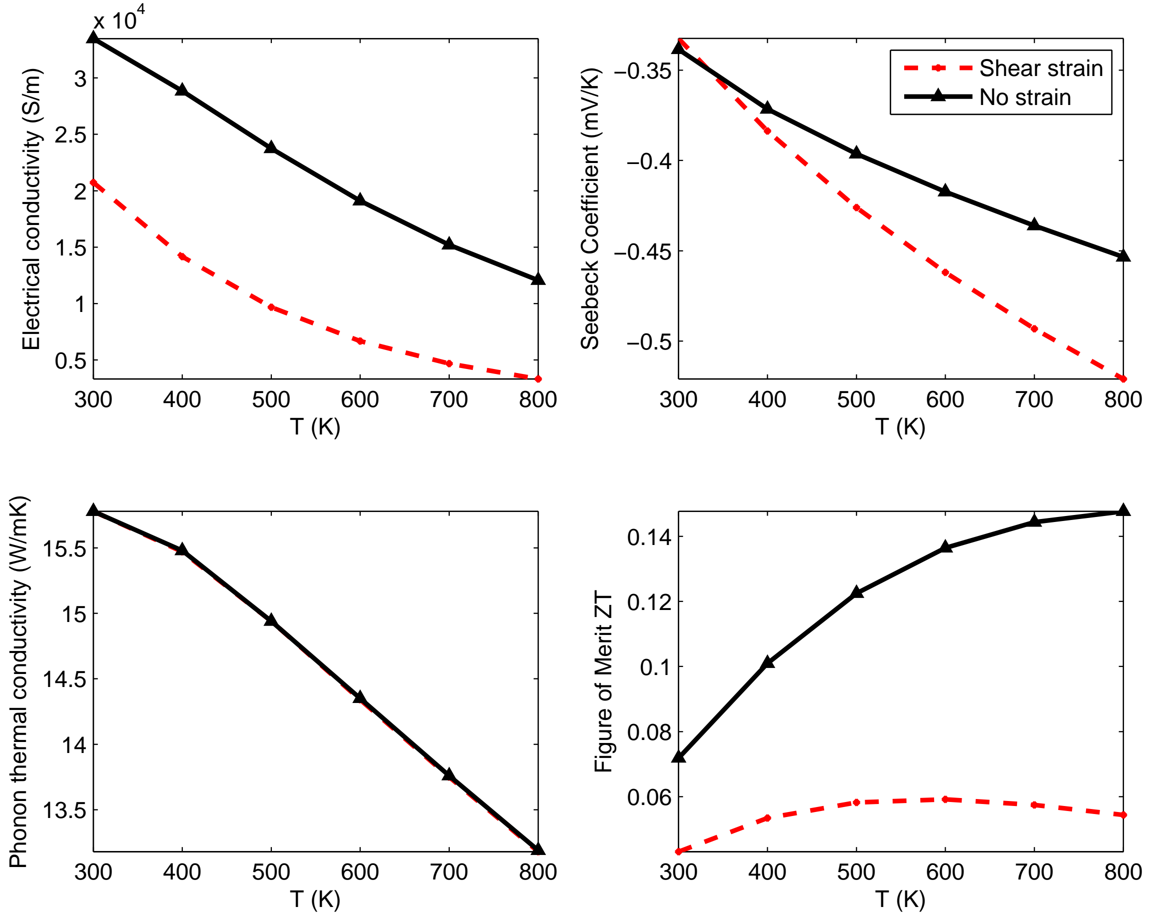

Figure 3.14: Thermoelectric properties of $Si_{0.8}Ge_{0.2}$ under shear strain when $L_{Ge} = 10nm$.

enhancement of ZT, we still find out that uniaxial tensile strain increases dimensionless figure of merit along the applied force direction. Uniaxial compressive strain largely decreases electrical conductivity and at the same time increase the phonon thermal conductivity. Even though Seebeck coefficient increases with compressive strain at high temperatures, ZT still decreases with uniaxial compressive strain applied.

Figures 3.14, 3.17 and 3.20 show that shear strain largely decreases electrical

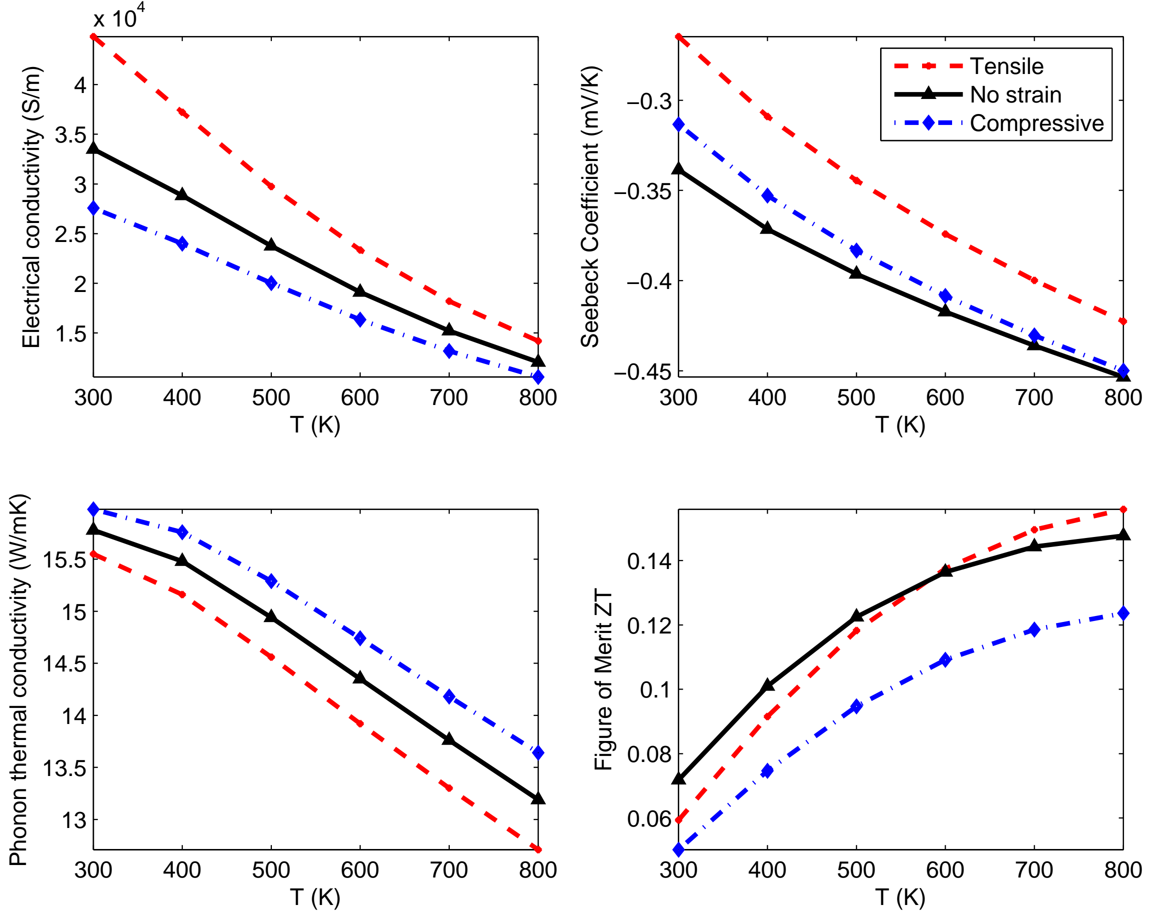

Figure 3.15: Thermoelectric properties of $Si_{0.8}Ge_{0.2}$ under biaxial strain when $L_{Ge} = 10nm$.

conductivity. With temperature increase, shear strain first decreases Seebeck coefficient and then increases it. However, the power factor is decreased by shear strain. At the same time, shear strain shows almost no influence on phonon thermal conductivity. Thus shear strain leads to a drop in ZT.

Figures 3.15, 3.18 and 3.21 show strain effect on thermoelectric properties of Si/Ge nanocomposites along the direction in which biaxial strain occurs. Biaxial tensile strain increases electrical conductivity but decreases Seebeck coefficient while

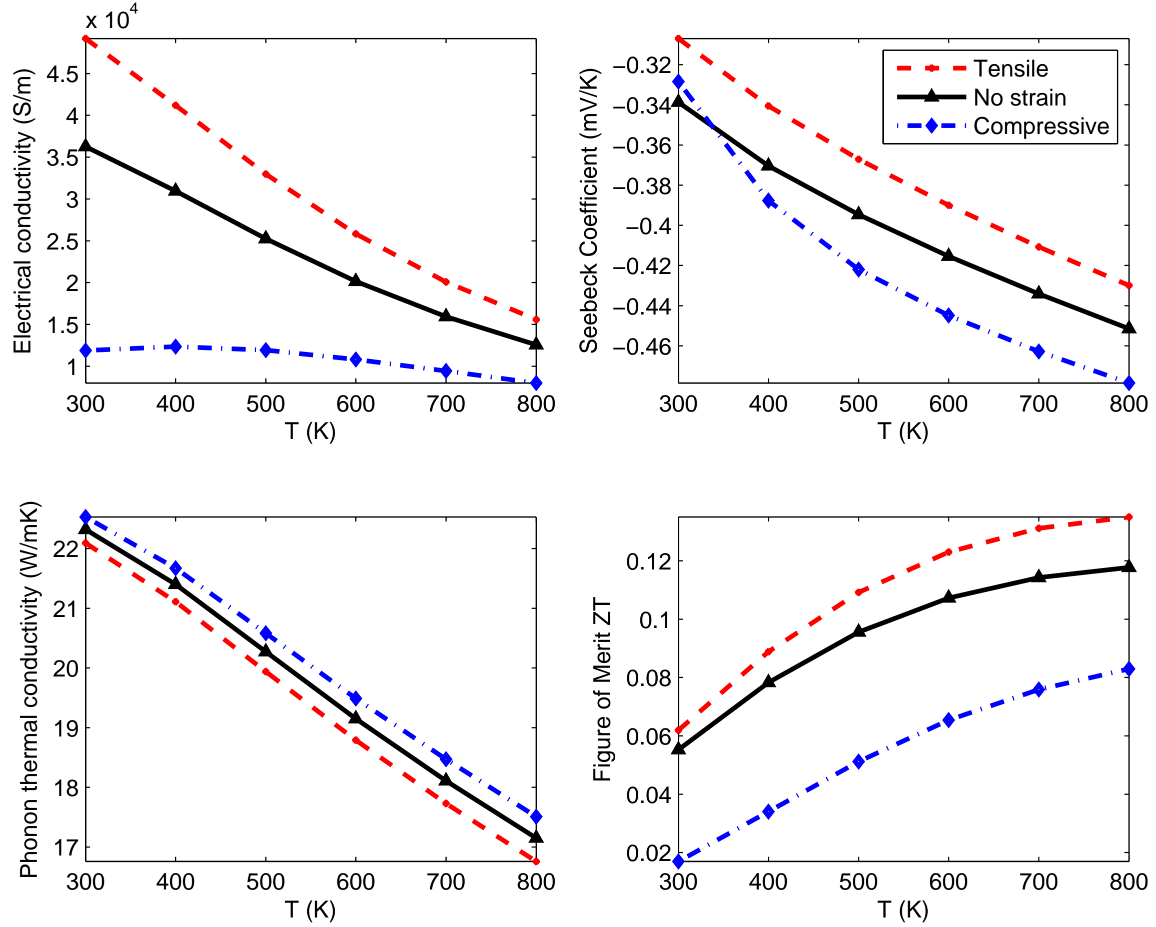

Figure 3.16: Thermoelectric properties of $Si_{0.8}Ge_{0.2}$ under uniaxial strain when $L_{Ge} = 15nm$.

biaxial compressive strain decreases electrical conductivity and Seebeck coefficient. Phonon thermal conductivity is decreased by tensile strain and increased by compressive strain. Combining them we find that tensile strain decreases ZT at relatively low temperature but increases it with increasing temperatures. Compressive strain decreases ZT at all temperatures considered here.

Comparing different types of strain, the uniaxial tensile strain leads to the largest increase of figure of merit. And this increase becomes clearer when the temperature

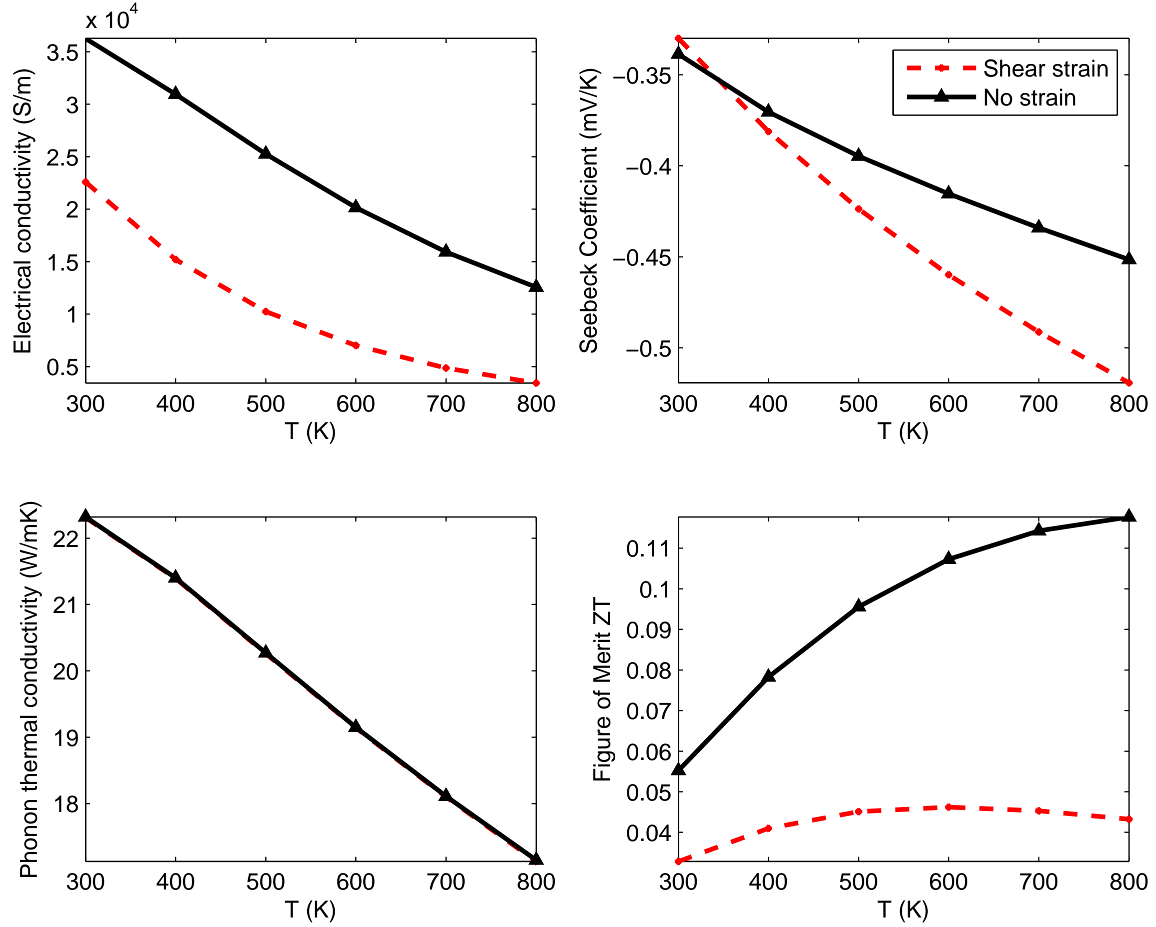

Figure 3.17: Thermoelectric properties of $Si_{0.8}Ge_{0.2}$ under shear strain when $L_{Ge} = 15nm$.

increases. At 800 K, 1% uniaxial tensile strain results in 14% increase of dimensionless figure of merit.

By comparing the same strain with different sizes, taking Figs. 3.13,3.16 and 3.19 for example, the increase of the size of the unit cell of SiGe nanocomposites largely increases phonon thermal conductivities, slightly increases electrical conductivity but has little influence on Seebeck coefficient, leading to slightly decreased figure of merit. This result shows that interface scattering has a large influence on phonon transport

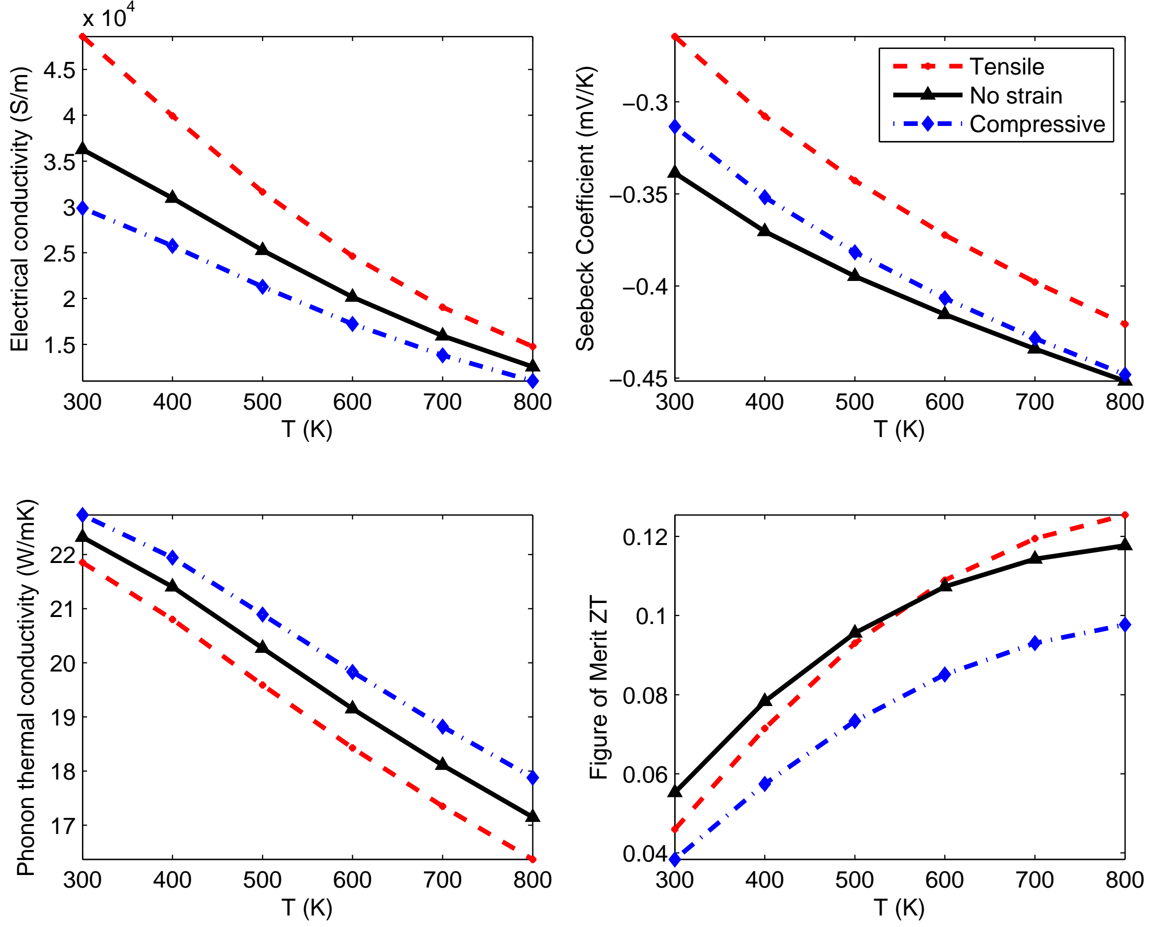

Figure 3.18: Thermoelectric properties of $Si_{0.8}Ge_{0.2}$ under biaxial strain when $L_{Ge} = 15nm$.

but small effects on electron transport. When L_{Ge} increases from 10 nm to 20 nm, the phonon thermal conductivity increases by about 60% (see Figs. 2.21 and 2.22) but the electrical conductivity only increases less than 5%. The change in electrical conductivity obtained here along with Fig. 3.8 shows that interface scattering has a small influence on electrical conductivity. This explains why ZT decreases when L_{Ge} increases.

Comparing phonon thermal conductivity figure in Fig. 3.13 with 2.22, we find

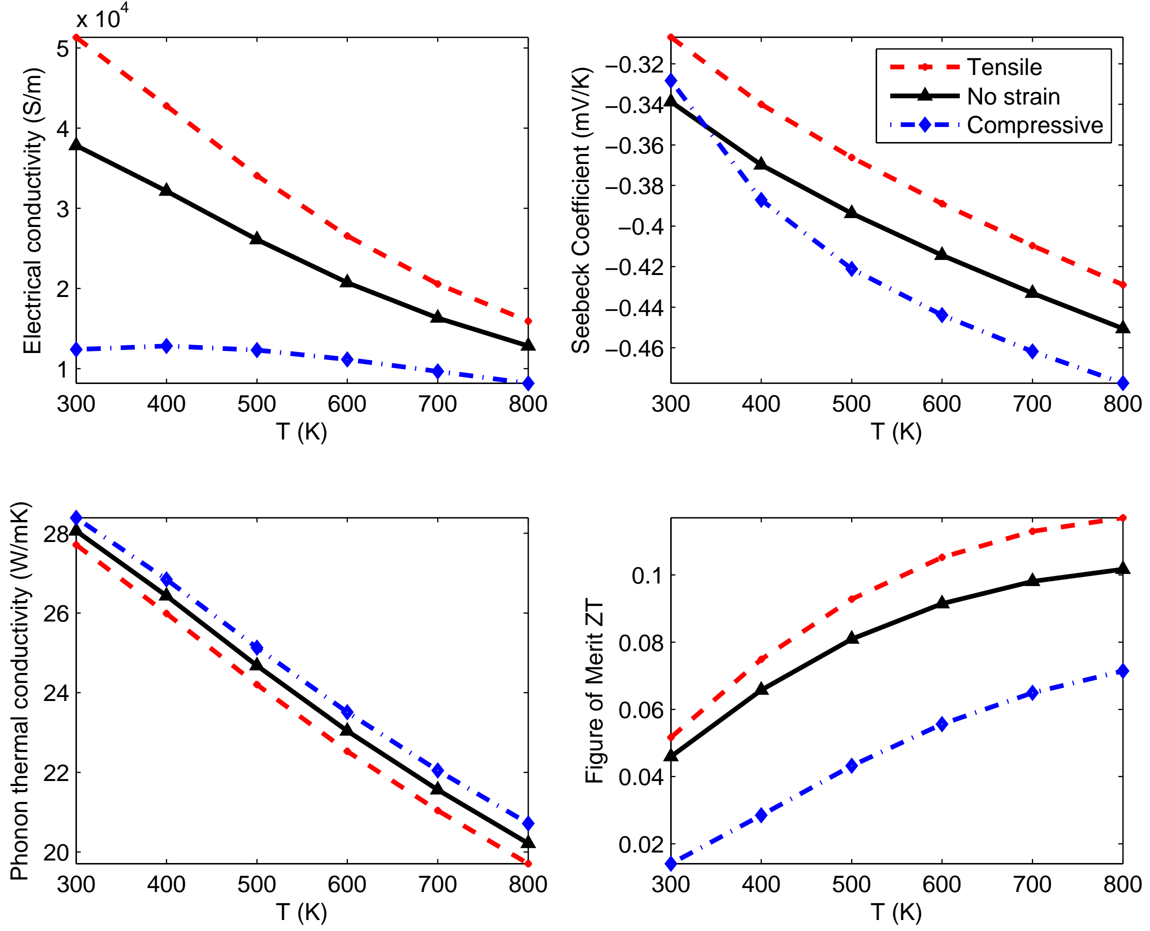

Figure 3.19: Thermoelectric properties of $Si_{0.8}Ge_{0.2}$ under uniaxial strain when $L_{Ge} = 20nm$.

out that at the same temperature and the same characteristic length, phonon thermal conductivity of $Si_{0.8}Ge_{0.2}$ is very close to that of $Si_{0.2}Ge_{0.8}$ nanocomposites. Figure 4.3 of [101] shows that SiGe alloys have similar property. Wang et al. found out that nanostructured n-type SiGe bulk alloy could reach a peak $ZT \approx 1.3$ at around 1173K [78]. This is mainly attributed to the low thermal conductivity, which is around 2.5 W/mk at 1173K. The low thermal conductivity comes from their increased interface scattering.

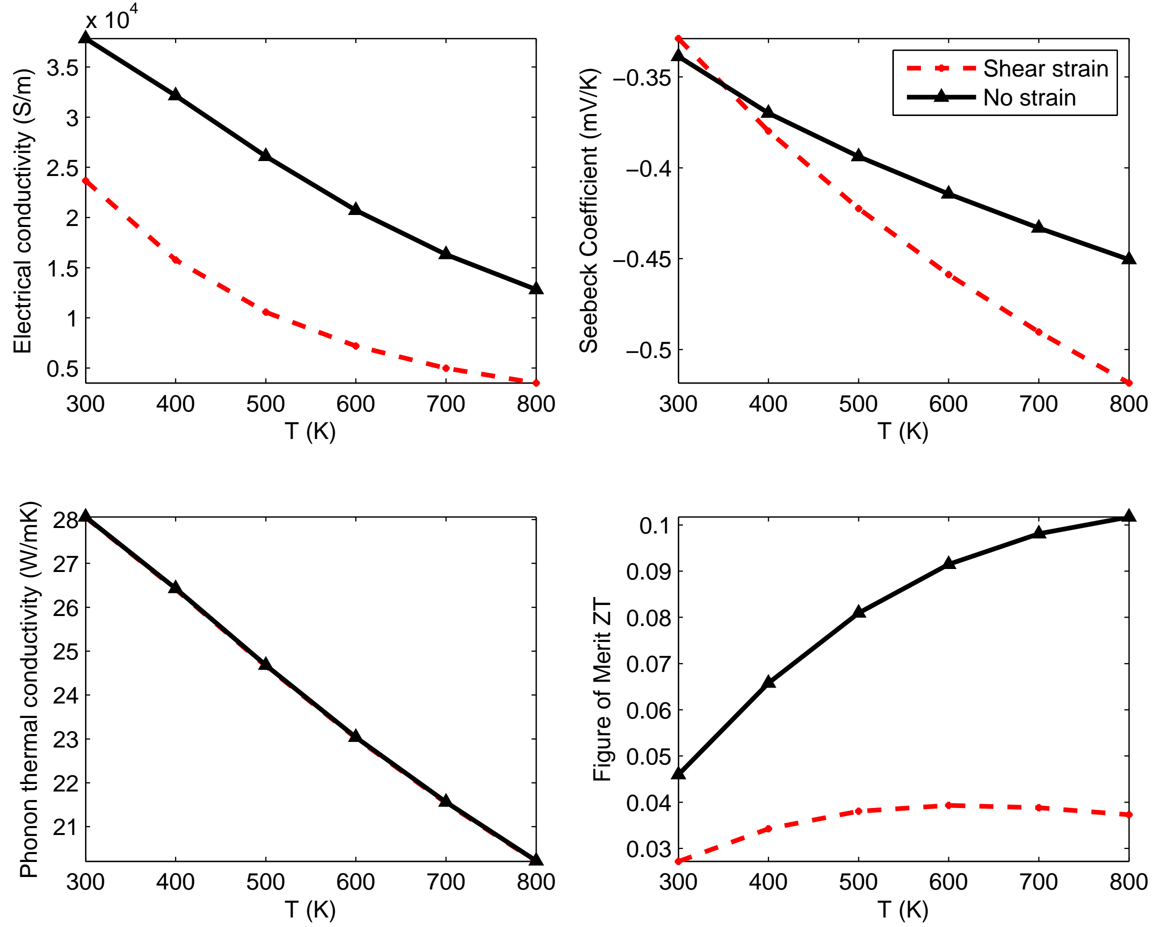

Figure 3.20: Thermoelectric properties of $Si_{0.8}Ge_{0.2}$ under shear strain when $L_{Ge} = 20nm$.

3.4 Summary

Strain effect on thermoelectric properties of SiGe nanocomposites has been studied in this chapter with analytical and numerical models. The influence of strain on electron transfer was studied by analytical formulas derived from BTE with band structures obtained from a degenerate $\mathbf{k} \cdot \mathbf{p}$ theory. Strain effect on thermal transport was studied by solving phonon BTE using strain dependent

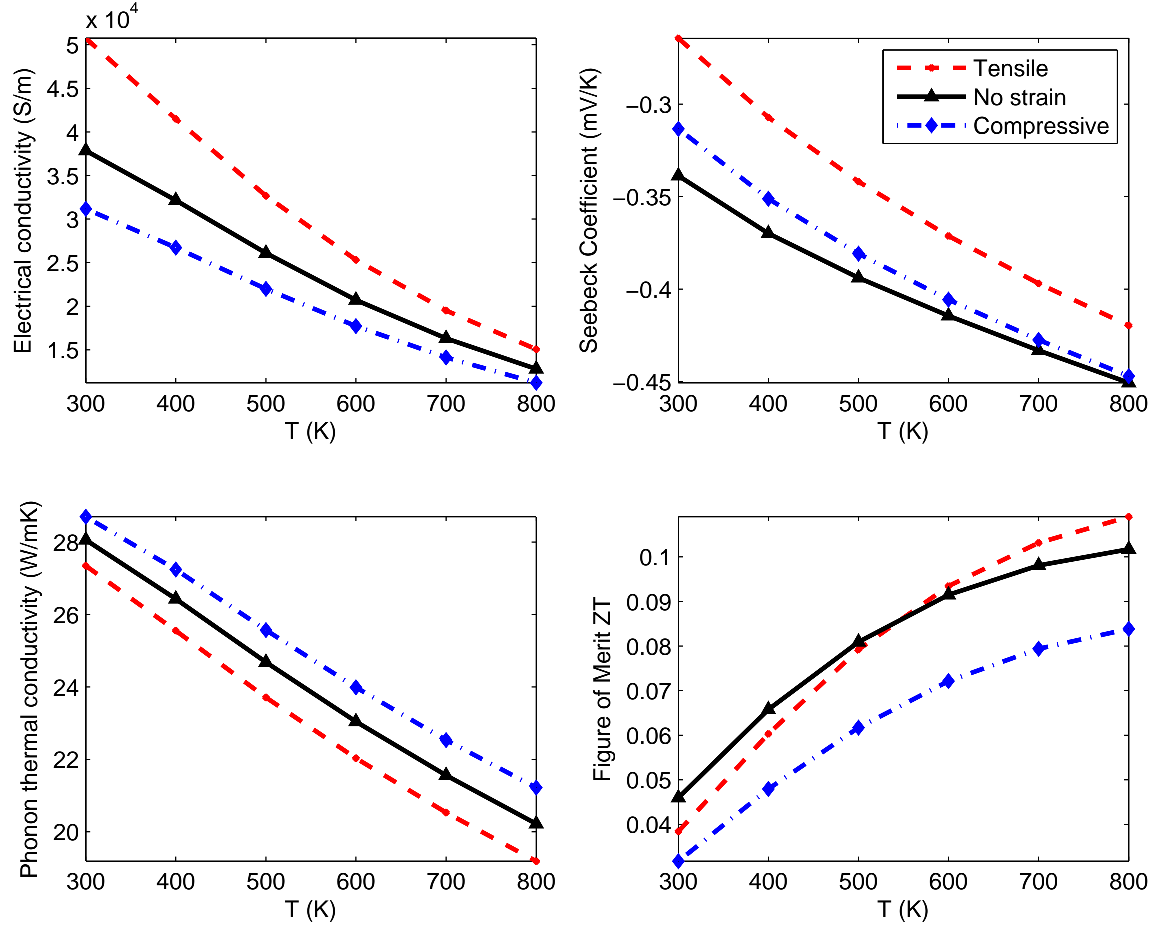

Figure 3.21: Thermoelectric properties of $Si_{0.8}Ge_{0.2}$ under biaxial strain when $L_{Ge} = 20nm$.

phonon scattering properties calculated from lattice dynamics. Our results confirm that nanocomposites are better thermoelectric materials compared to their alloys. In the 300-800 K temperature range, uniaxial tensile strain along ⟨100⟩ direction can improve dimensionless figure of merit parallel to the tension. Biaxial tensile strain along [100] and [010] directions only leads to ZT enhancement at high temperatures in the tension directions. Shear strain and compressive strains decrease dimensionless figure of merit. At 800 K with electron concentration to be

$10^{19} cm^{-3}$, 1% uniaxial tensile strain can increase figure of merit of $Si_{0.8}Ge_{0.2}$ nanocomposites by 14% at 800 K and the dimensionless figure of merit can reach 0.18 in $Si_{0.8}Ge_{0.2}$ nanocomposites.

CHAPTER 4

COMPUTATIONAL ANALYSIS OF NANOCOMPOSITE BASED THERMAL ACTUATORS

4.1 Introduction

Micro-scale thermal actuators (TAs) are miniature devices using thermal expansion produced by Joule heating to generate in-plane deflections and actuation forces. Typical thermal actuators are comprised of beam structures whose elongation due to thermal expansion is the main driving force of the device. Compared to other MEMS actuators such as electrostatic actuators and magnetic actuators, TAs can provide a larger force output per unit area [102, 103]. In addition, the structures of TAs are usually simple, making integration and fabrication very easy. However, TAs typically generate small displacements and have a high power consumption due to energy loss from the heated beams to the

surroundings. To overcome these shortcomings, a variety of methods have been proposed to improve the mechanical performance and energy efficiency of TAs. For instance, Comtois and Bright employed an array of two or more TAs to generate high forces [102]. Que et al. found that cascaded Si devices could save power while offering comparable actuation displacement [103]. Huang et al. and Hickey et al. investigated effects of the length and width of TA beams on the overall performance [104, 33]. Sigmund investigated topology optimized TAs [105]. Yan et al. introduced a bidirectional vertical TA which can generate twice the total deflection of the traditional U-shaped actuator [106]. Along the line of topology optimization, Chen et al. proposed TAs with contour beams to increase actuator stroke and decrease power consumption [107]. The design of the contour beams was further improved by Sassen et al. [35]. While all these approaches can improve the performance of TAs, another important dimension of TA design and optimization, the material configuration, has not been paid much attention.

The concept of thermal actuation using nanocomposite materials is explored in this chapter. Nanocomposites are multi-phase materials containing components with nanometer characteristic lengths. In this work, we propose to incorporate nanocomposites in actuator structures and utilize their non-classical electrical to thermal conductivity ratio to tailor the temperature profile in the actuator and achieve a larger thermal actuation displacement. To test the validity of the concept, we develop a multi-scale electro-thermo-mechanical model for computational analysis of nanocomposite TAs. While models for micro TAs have been well developed [104, 33, 108], the inclusion of nanocomposites impose a major challenge, i.e., nano-scale size and scattering effects on carrier transport properties must be accounted for in the micro-scale electro-thermo-mechanical analysis. To address this

issue, we construct a top-down multi-scale model for the computational analysis. In the multi-scale model, the thermo-mechanical behavior of the actuator is described using the continuum theories, while the material thermal and electrical transport properties are calculated from atomistic models to take into account size, interface scattering and strain effects. The carrier transport properties such as thermal and electrical conductivities obtained from the atomistic descriptions are used in the continuum level models to calculate the physical quantities such as temperature and structural deformation. These continuum quantities are then employed as external conditions for the re-calculation of the thermal and electrical conductivities from the atomistic descriptions. The iteration between the two levels continues until a self-consistent solution is obtained. Broadly speaking, this two-level multi-scale model fits in the quasicontinuum multi-scale modeling framework [53, 109]. By using the multi-scale model, we demonstrate the performance of nanocomposite TAs. The effects of several design parameters are also investigated.

4.2 Conceptual Development

Commonly used in-plane TAs can be categorized according to their geometry configuration into V-shaped and U-shaped TAs. A V-shaped TA consists of a V-shaped beam anchored at both ends with a tip in the middle. Upon heating, the tip will deform in the vertical direction due to the thermal expansion of the beam as shown in Fig. 4.1 (a). A U-shaped TA contains two beam structures (legs) with different cross-sections as shown in Fig. 4.1 (b). The difference in cross-section causes a temperature difference between the two legs resulting in larger expansion of the thin (hot) leg than the wide (cold) leg, and thus a lateral deflection of the actuator [110].

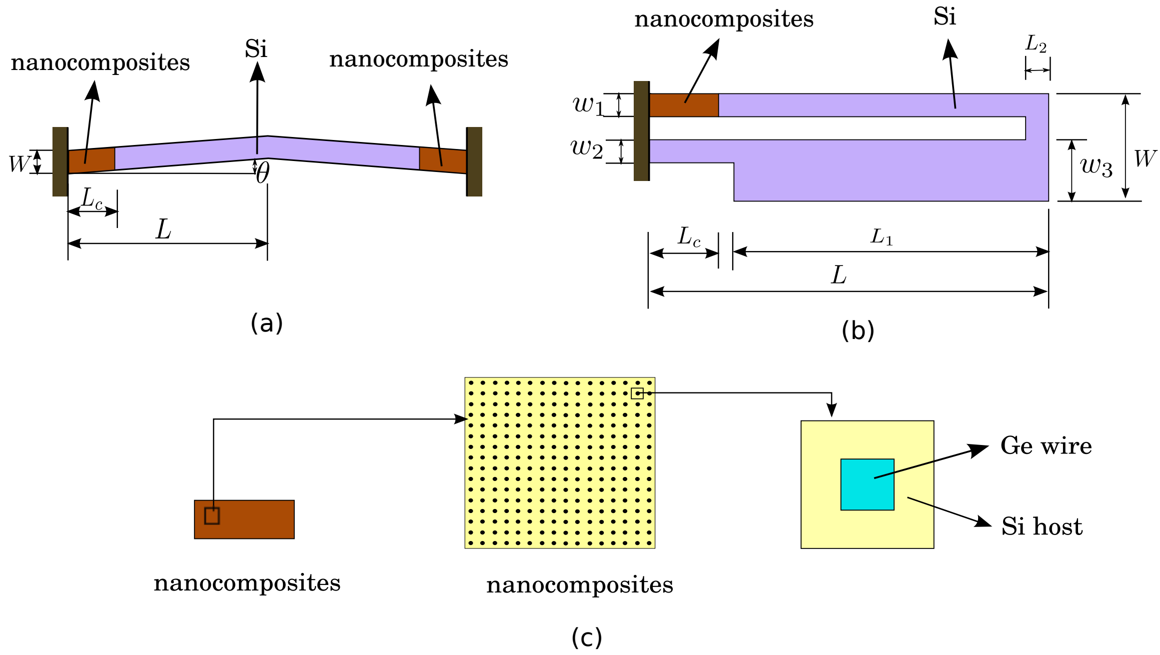

Figure 4.1: Si/Ge nanocomposite-based thermal actuators: (a) V-shaped actuator. (b) U-shaped actuator. (c) Si/Ge nanocomposite material.

Taking the V-shaped TA shown in Fig. 4.1 (a) as an example and assuming heat transfer in the TA is dominated by conduction along the longitudinal axis of the beam, the steady state temperature distribution in the TAs can be obtained by solving the 1-D governing equation

$$\nabla \cdot (k_t \nabla T) = -\frac{\sigma V^2}{4L^2} , \tag{4.1}$$

where k_t is the total thermal conductivity, T is the temperature, V is the applied voltage, σ is the electrical conductivity and L is half length of the actuator beam (assuming θ is small). If k_t is constant and the temperature at the two ends is T_0,

the solution to Eq.(4.1) can be obtained as

$$T(x) = -\frac{\sigma V^2}{8L^2 k_t}(x - L)^2 + T_0 + \frac{\sigma V^2}{8k_t} \ . \tag{4.2}$$

With the initial temperature set to be T_0, the total elongation of the beam, Δ, can be calculated as

$$\Delta = \int_0^{2L} \alpha_L(T) \cdot [T(x) - T_0] \ dx \ , \tag{4.3}$$

where α_L is the linear thermal expansion coefficient of the actuator beam. From Eq. (4.2), it is clear that the TA's temperature distribution can be altered by changing the length of TA beams. In addition, by changing the cross-sectional area along the length of the TA beam, the current density and the strength of the Joule heating can be varied to alter the temperature distribution. Along this line, efforts have been made to improve TAs' performance by adjusting the length, width and cross-section of the TA's beams [104, 33, 107, 35], using the array or cascade of TAs [102, 103] and optimization of fabrication and topology [105, 106]. While these TA optimization strategies focus on the geometry configuration of the device, we observe that the σ/k_t ratio plays an important role in the temperature function as shown in Eq. (4.2). A material with high σ/k_t ratio would enable a rapid change in the temperature solution given in Eq. (4.2) and thus facilitate temperature manipulation in the TA beam. Nanocomposites are such materials with a high σ/k_t ratio due to a low phonon thermal conductivity caused by strong phonon scattering at the interfaces of material components. This unique property of nanocomposites has been successfully applied to create efficient thermoelectric materials [17]. Another observation can be made from Eq. (4.3) that a large temperature increase,

$\Delta T(x) = T(x) - T_0$, along the entire length of the beam ($0 \leq x \leq 2L$) is desirable to achieve a large thermal expansion in beam length. However, to prevent failure of the device, an allowable temperature increase, ΔT_{allow}, is usually imposed for most TAs. Therefore, the temperature increase in an optimal TA design can be translated as $\Delta T(x) \rightarrow \Delta T_{allow}$ for $0 \leq x \leq 2L$. In light of these considerations, we use nanocomposites at the two ends of the V-shaped TA (shown in Fig. 4.1 (a)) to enable a rapid temperature increase within a short distance. Conventional materials such as doped Si with relatively low σ/k_t ratio are then used for the rest of the beam to lower the temperature gradient and maintain the elevated temperature in the majority of the TA beam structure. With this material configuration, a high $\Delta T(x)$ is produced through most part of the TA beam and a high beam thermal expansion can be achieved. The same idea can be used in the U-shaped TAs where the nanocomposite material is used at the fixed end of the upper beam as shown in Fig. 4.1 (b). It should be noted that this approach is compatible and can be combined with other geometry configuration based optimization approaches.

In this chapter, we investigate a type of Si/Ge nanocomposites for thermal actuation. As shown in Fig. 4.1 (c), the Si/Ge nanocomposite has a periodic nano structure with Ge nanowires embedded in a Si host material. In the following sections, we present a multi-scale model for the electro-thermo-mechanical analysis of the nanocomposite TAs. By using the model, numerical simulations are carried out to demonstrate the performance of the nanocomposite TAs.

4.3 Computational Modeling

We adopt a top-down multi-scale paradigm to model the nanocomposite TAs. The overall thermo-mechanical response of the actuators due to the Joule heating is modeled using classical continuum theories, while the thermal and electrical properties of the doped Si and the nanocomposite material are obtained from nano-scale models and the mechanical stiffness and thermal stress matrices of nanocomposites are calculated using the Mori-Tanaka method. Phonon thermal conductivities of Si/Ge nanocomposites are computed as a function of mechanical strain through a combined model of strain dependent lattice dynamics and ballistic BTE. Electronic thermal conductivities are calculated using the Wiedemann-Franz law. For doped Si and Si/Ge nanocomposites, the electrical conductivity is calculated by using an analytical model derived from the BTE under relaxation-time approximation. Electron scattering effects due to ionized impurity and phonon deformation-potential are included in the relaxation time for doped Si while an additional material interface scattering is included for the nanocomposites.

4.3.1 Mechanical analysis

If we define the overall stress of the nanocomposites to be $\boldsymbol{\sigma} = \{\sigma_x \; \sigma_y \; \sigma_z \; \sigma_{xy} \; \sigma_{yz} \; \sigma_{xz}\}^T$, the three-dimensional (3D) governing equations for elasticity problems can be expressed as follows:

$$\frac{\partial \sigma_x}{\partial x} + \frac{\partial \sigma_{xy}}{\partial y} + \frac{\partial \sigma_{xz}}{\partial z} + b_x = 0 \ ,$$
$$\frac{\partial \sigma_{xy}}{\partial x} + \frac{\partial \sigma_y}{\partial y} + \frac{\partial \sigma_{yz}}{\partial z} + b_y = 0 \ , \tag{4.4}$$
$$\frac{\partial \sigma_{xz}}{\partial x} + \frac{\partial \sigma_{yz}}{\partial y} + \frac{\partial \sigma_z}{\partial z} + b_z = 0,$$

with b_x, b_y and b_z to be body forces at x, y and z directions, respectively. Assume the displacement to be $\mathbf{u} = \{u_x \ u_y \ u_z\}^T$, and the overall strain to be $\boldsymbol{\varepsilon} = \{\varepsilon_x \ \varepsilon_y \ \varepsilon_z \ \varepsilon_{xy} \ \varepsilon_{yz} \ \varepsilon_{xz}\}^T$, according to kinematics, we have

$$\left\{ \begin{array}{c} \varepsilon_x \\ \varepsilon_y \\ \varepsilon_z \\ \varepsilon_{xy} \\ \varepsilon_{yz} \\ \varepsilon_{xz} \end{array} \right\} = \left\{ \begin{array}{c} \frac{\partial u_x}{\partial x} \\ \frac{\partial u_y}{\partial y} \\ \frac{\partial u_z}{\partial z} \\ \frac{\partial u_x}{\partial y} + \frac{\partial u_y}{\partial x} \\ \frac{\partial u_y}{\partial z} + \frac{\partial u_z}{\partial y} \\ \frac{\partial u_z}{\partial x} + \frac{\partial u_x}{\partial z} \end{array} \right\}. \tag{4.5}$$

The constitutive relation for thermoelastic material response is given by

$$\boldsymbol{\sigma} = \mathbf{C}\boldsymbol{\varepsilon} + \mathbf{c}\Delta T, \tag{4.6}$$

where $\mathbf{C}$ is the 6×6 overall stiffness matrix of composites, $\mathbf{c} = \{c_1 \ c_2 \ c_3 \ c_4 \ c_5 \ c_6\}^T$ is the 6×1 thermal stress vector defined as $\mathbf{c} = -\mathbf{C}\mathbf{m}$ where $\mathbf{m}$ is a vector listing the

linear thermal expansion coefficients, ΔT is temperature gradient. Note that because the mechanical problem is analyzed on a composite, homogenized effective stress and strain need to be used instead of stress and strain of a single material.

The elastic constants of the constituent materials can be homogenized to obtain the effective elastic constants of the composites. Several models have been proposed to obtain the effective elastic moduli in terms of atomic percentage and phase geometry. For example, Hashin-Shtrikman bounds have been used to bracket the actual magnitudes of the moduli for two-phase and multi-phase systems [111]. Self-consistent approaches have been applied to calculate effective elastic moduli for aligned fiber composites [112] and two-phase media reinforced by randomly oriented inclusions of various shapes [113]. The Mori-Tanaka method [114] was applied by Chen et al. to evaluate the effective elastic moduli of multi-phase composites reinforced by aligned fibers or platelets and similar systems with randomly oriented reinforcement [115]. Benveniste et al. have identified conditions limiting the use of the self-consistent and Mori-Tanaka methods in multi-phase systems [116]. Dvorak and Benveniste have commented on their extensive similarities [117]. Reiter et al. calculated the elastic response of micromechanical systems consisting of piecewise homogeneous layers by using both Mori-Tanaka and self-consistent methods. It was found that the Mori-Tanaka method gives a better prediction of the mechanical behavior for composite materials with a well-defined continuous matrix and discontinuous second phase, while the self-consistent approach is more accurate for graded materials with a skeletal micro-structure in wide transition zone between matrix phases [118]. For this reason, Mori-Tanaka method is adopted in this work to obtain the effective elastic moduli of the Si/Ge nanocomposites.

The Mori-Tanaka method provides a way to predict the elastic properties of

two-phase composites according to the inclusion's volume fraction and geometry. In Mori-Tanaka method, the average inclusion strain is related to average matrix strain and the inclusion interaction effects are approximately accounted for. The method is summarized as follows.

Composites reinforced by aligned fibers are often transversely isotropic. If the axis of symmetry is chosen as parallel to the z-axis of a Cartesian coordinate system, then the elastic response of a transversely isotropic solid may be described in the form [119]:

$$\begin{Bmatrix} \frac{1}{2}(\sigma_x + \sigma_y) \\ \\ \sigma_z \end{Bmatrix} = \begin{bmatrix} \mathcal{K} & \mathcal{L} \\ \\ \mathcal{L} & \mathcal{N} \end{bmatrix} \begin{Bmatrix} \varepsilon_x + \varepsilon_y \\ \\ \varepsilon_z \end{Bmatrix} ,$$

$$\sigma_x - \sigma_y = 2\mathcal{M}(\varepsilon_x - \varepsilon_y) \ , \tag{4.7}$$

$$\sigma_{xy} = \mathcal{M}\varepsilon_{xy}, \qquad \sigma_{yz} = \mathcal{P}\varepsilon_{yz}, \qquad \sigma_{xz} = \mathcal{P}\varepsilon_{xz} \ ,$$

where $\mathcal{K}$ is the plane-strain bulk modulus for lateral dilatation without longitudinal extension, $\mathcal{N}$ is the modulus for longitudinal uniaxial straining, $\mathcal{L}$ is the associated cross modulus, $\mathcal{M}$ is the rigidity modulus in any transverse direction and $\mathcal{P}$ is the shear modulus for longitudinal shearing. For an isotropic material, these moduli are related to the bulk and shear moduli K and G as:

$$\mathcal{K} = K + \frac{1}{3}G, \qquad \mathcal{L} = K - \frac{2}{3}G, \qquad \mathcal{N} = K + \frac{4}{3}G, \qquad \mathcal{M} = \mathcal{P} = G. \tag{4.8}$$

Elastic constants of single crystal Si and Ge in an arbitrarily oriented coordinate system can be obtained from the literature [120]. It has been shown that, for the temperature range of 300-800 K we considered in this work, doping and temperature

effects on the elastic constants of single crystal Si and nanostructured n- and p- type Si/Ge composites are negligible [121, 122]. In this work, we take (100) direction as the longitudinal direction of the actuators and assume the in-plane elastic constants are isotropic. For a two-phase composite system, the effective elastic constants in Eq. (4.8) can be obtained by [115]:

$$
\begin{aligned}
\mathcal{P} &= \frac{2V_f\mathcal{P}_m\mathcal{P}_f + V_m(\mathcal{P}_m\mathcal{P}_f + \mathcal{P}_m^2)}{2V_f\mathcal{P}_m + V_m(\mathcal{P}_f + \mathcal{P}_m)} \\
\mathcal{M} &= \frac{\mathcal{M}_m\mathcal{M}_f(\mathcal{K}_m + 2\mathcal{M}_m) + \mathcal{K}_m\mathcal{M}_m(V_f\mathcal{M}_f + V_m\mathcal{M}_m)}{\mathcal{K}_m\mathcal{M}_m + (\mathcal{K}_m + 2\mathcal{M}_m)(V_f\mathcal{M}_m + V_m\mathcal{M}_f)} \\
\mathcal{K} &= \frac{V_f\mathcal{K}_f(\mathcal{K}_m + \mathcal{M}_m) + V_m\mathcal{K}_m(\mathcal{K}_f + \mathcal{M}_m)}{V_f(\mathcal{K}_m + \mathcal{M}_m) + V_m(\mathcal{K}_f + \mathcal{M}_m)} \\
\mathcal{L} &= \frac{V_f\mathcal{L}_f(\mathcal{K}_m + \mathcal{M}_m) + V_m\mathcal{L}_m(\mathcal{K}_f + \mathcal{M}_m)}{V_f(\mathcal{K}_m + \mathcal{M}_m) + V_m(\mathcal{K}_f + \mathcal{M}_m)} \\
\mathcal{N} &= V_m\mathcal{N}_m + V_f\mathcal{N}_f + (\mathcal{L} - V_f\mathcal{L}_f - V_m\mathcal{L}_m)\frac{\mathcal{L}_f - \mathcal{L}_m}{\mathcal{K}_f - \mathcal{K}_m} \ ,
\end{aligned}
\tag{4.9}
$$

where the subscripts f and m represent the fiber and matrix, respectively, and V_f and V_m are the volume fractions of the fiber and matrix, respectively, with $V_f + V_m = 1$.

The stiffness matrix $\mathbf{C}$ in the constitutive law can be obtained from Eq. (4.8) with the effective elastic constants calculated from Eq. (4.9), i.e.,

$$
\mathbf{C} = \begin{bmatrix}
\mathcal{K}+\mathcal{M} & \mathcal{K}-\mathcal{M} & \mathcal{L} & 0 & 0 & 0 \\
\mathcal{K}-\mathcal{M} & \mathcal{K}+\mathcal{M} & \mathcal{L} & 0 & 0 & 0 \\
\mathcal{L} & \mathcal{L} & \mathcal{N} & 0 & 0 & 0 \\
0 & 0 & 0 & \mathcal{M} & 0 & 0 \\
0 & 0 & 0 & 0 & \mathcal{P} & 0 \\
0 & 0 & 0 & 0 & 0 & \mathcal{P}
\end{bmatrix} . \tag{4.10}
$$

The overall thermal stress vector $\mathbf{c}$ of the composite material can then be found in the form [123],

$$\mathbf{c} = \mathbf{c}_m + (\mathbf{C} - \mathbf{C}_m)(\mathbf{C}_m - \mathbf{C}_f)^{-1}(\mathbf{c}_m - \mathbf{c}_f). \tag{4.11}$$

In our case, composites with fibers as inclusions in the TAs can be treated as plane strain problem, so $\sigma_{xz} = 0$ and $\sigma_{yz} = 0$. Then the stress-strain relation, Eq. (4.6), can be simplified as

$$\left\{ \begin{array}{c} \sigma_x \\ \sigma_y \\ \sigma_{xy} \end{array} \right\} = \left[\begin{array}{ccc} \mathcal{K}+\mathcal{M} & \mathcal{K}-\mathcal{M} & 0 \\ \mathcal{K}-\mathcal{M} & \mathcal{K}+\mathcal{M} & 0 \\ 0 & 0 & \mathcal{M} \end{array} \right] \left\{ \begin{array}{c} \varepsilon_x \\ \varepsilon_y \\ \varepsilon_{xy} \end{array} \right\} + \left\{ \begin{array}{c} c_1 \\ c_2 \\ c_4 \end{array} \right\} \Delta T, \tag{4.12}$$

The temperature dependence of linear thermal expansion coefficients of Si and Ge have been studied extensively [124]. An empirical expression was given by Okada and Tokumaru for Si thermal expansion from 120 to 1500 K [125]. Reeber and Wang used a semi-empirical quasi-harmonic model to fit available data for Si and Ge from near 0 K to the vicinity of their respective melting points and obtained the following relation [126]

$$\alpha_V = 3 \sum_{i=1}^{4} X_i \frac{(\theta_i/T)^2 \, e^{\theta_i/T}}{[e^{\theta_i/T} - 1]^2}, \tag{4.13}$$

where α_V is the volume thermal expansion, θ_is and X_is are fitting parameters, whose recommended values for Si and Ge can be found in Table 2 of [126]. Assuming isotropic thermal expansion, the linear thermal expansion coefficients of Si and Ge are obtained as 1/3 of their volume thermal expansion. With elastic and thermal expansion properties of the nanocomposite material obtained, the mechanical analysis

is performed by using the linear elasticity theory, i.e.,

$$\nabla \cdot \boldsymbol{\sigma} = 0 \tag{4.14}$$

4.3.2 Thermal analysis

As heat transfer is dominated by conduction in electric current heated slender beams, convection and radiation are neglected. The temperature distribution in actuator beams is obtained by solving the Fourier heat conduction equation,

$$\nabla \cdot (k_t \nabla T) = -J^2/\sigma, \tag{4.15}$$

where J is the current density. Note that k_t contains both phonon and electronic contributions: $k_t = k_p + k_e$ where k_p is the phonon thermal conductivity and k_e is the electronic thermal conductivity.

The solution of Eq. (4.15) is challenging for nanocomposite materials. First, for Si/Ge nanocomposites, when the characteristic length of the nano-fibers is less than a hundred nanometers, ballistic phonon transport dominates. Interface scattering plays an important role in the thermal resistance of the material [94]. The phonon thermal conductivity needs to be determined by using ballistic transport models. Second, the thermal conductivity also depends on mechanical strain [46, 79]. In the coupled thermo-mechanical analysis of the TAs, the strain effect on the thermal conductivity needs to be considered. Third, the electrical conductivity of doped Si/Ge nanocomposites can be different from that in the bulk materials. Various scattering effects need to be included along with the temperature effect. These issues are addressed as follows.

4.3.2.1 Thermal conductivities modeling of doped Si and Si/Ge nanocomposites

The calculation of phonon thermal conductivity of doped Si and Si/Ge nanocomposites has been discussed in Chap. 2. The main procedure is repeated briefly as follows. With deformation information obtained from mechanical analysis, **F** is related to **u** by

$$\mathbf{F} = \begin{bmatrix} F_{11} & F_{12} & 0 \\ F_{21} & F_{22} & 0 \\ 0 & 0 & 1 \end{bmatrix} \tag{4.16}$$

$$= \begin{bmatrix} 1+\frac{\partial u_x}{\partial x} & \frac{\partial u_x}{\partial y} & 0 \\ \frac{\partial u_y}{\partial x} & 1+\frac{\partial u_y}{\partial y} & 0 \\ 0 & 0 & 1 \end{bmatrix} \tag{4.17}$$

With the above deformation gradient tensor, phonon dispersion relations are calculated. Then the strain and temperature dependent bulk phonon thermal conductivity of Si and Ge is computed by Slack relation given by Eq. (2.17) and phonon thermal conductivity of Si/Ge nanocomposites is calculated by solving BTE, Eq. (2.27), in a 2-D unit cell of the nanocomposite material as shown in Fig. 3.7 by finite volume method with periodic boundary conditions and diffuse mismatch interface conditions shown in Eq. (2.32).

The electronic thermal conductivity, k_e, is calculated from the Wiedemann-Franz law, $k_e = L_z \sigma T$. We consider a doping level of $2 \times 10^{20} cm^{-3}$ for the TAs in this work thus the value of metal is used for L_z. Note that, since the electronic thermal conductivity, k_e, is only a small fraction of the total thermal conductivity, k_t, the

strain effect on the electronic thermal conductivity is not considered.

4.3.2.2 Electrical conductivity modeling of doped Si and Si/Ge nanocomposites

The electrical conductivity σ is calculated from the analytical model based on BTE under relaxation-time approximation described in Chap. 3. Here doped Si and Si/Ge nanocomposites are assumed to be n-type with a carrier concentration of $2 \times 10^{20} cm^{-3}$. Three-band transport is considered by calculating the contribution from two conduction bands, one close to the X point and one at the L point, and one valence band at the Γ point. Results indicate that contributions from L conduction band and Γ valence band are negligible at the carrier concentration and temperature considered here. Nonparabolicity and anisotropicity are accounted for in the dispersion relation of electrons. For doped Si, ionized impurity (II) and phonon deformation potential (DP) scatterings have been included in the carrier transport. For Si/Ge nanocomposites, in addition to II and DP scatterings, grain boundary (GB) scattering (interface scattering) is also included. Matthiessen's rule is used to obtain the total relaxation time accounting for all the scattering mechanisms. Detailed expressions for X conduction band are listed in Table 3.1. Note that, as a limitation of the current model, strain effect on the electrical conductivity is not considered.

4.3.3 Main Procedure

In the main computational procedure for the electro-thermo-mechanical analysis of the TAs as shown in Fig. 4.2, for a given input current density J, $T = T_0 = 300K$ and $\boldsymbol{\varepsilon} = 0$ are specified as the initial conditions. Heat conduction equation with

Joule heating is solved to obtain the temperature distribution in the actuator. The temperature change is then used in the mechanical analysis as discussed in Chap. 4.3.1. After the displacements, strain and stress are computed, the strain and temperature dependent phonon thermal conductivity, the temperature dependent electronic thermal conductivity and electrical conductivity are calculated as described in Chap. 4.3.2. The updated material properties are then used to solve the thermal and mechanical equations again. The iterative procedure continues until a converged solution is obtained.

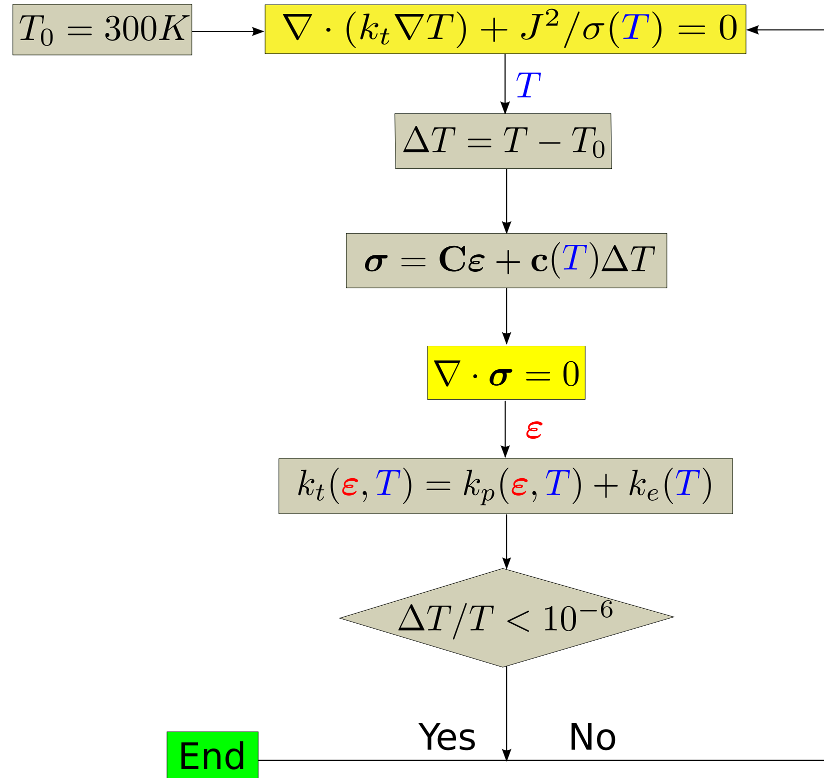

Figure 4.2: Computational procedure for the electro-thermo-mechanical analysis of the thermal actuators.

4.4 Results and Discussion

4.4.1 Properties of Si and $Si_{1-x}Ge_x$ nanocomposites

The strain and/or temperature dependent mechanical, thermal and electrical properties of bulk Si and $Si_{1-x}Ge_x$ nanocomposites are investigated in this section. Elastic constants and linear thermal expansion coefficients of Si and $Si_{1-x}Ge_x$ nanocomposites are shown in Figs. 4.3 and 4.4, respectively. In these two figures, x is the atomic percentage of Ge and $x = 0$ is corresponding to bulk Si. Figure 4.3 shows the relation between elastic constants and x. As x increases, the elastic constants decrease linearly due to the lower elastic constants of Ge. With x increasing from 0 to 0.2 (i.e. 20%), the elastic constants decrease by 6.3%, 8.2% and 5.0% for C_{11}, C_{12} and C_{44}, respectively. The atomic percentage of Ge has a significant effect on the linear thermal expansion coefficient, as shown in Fig. 4.4. Comparing $Si_{0.8}Ge_{0.2}$ nanocomposite with the bulk Si, 25.6% and 15.2% increase of the thermal expansion coefficient are observed at 300 K and 800 K, respectively. This result can be attributed to the large difference in thermal expansion coefficients between Si and Ge.

Figure 4.5 shows strain and temperature dependent phonon thermal conductivity of single crystal Si between 300-800 K calculated from Eq. (2.17). A maximum 2% plane strain is considered here. In Figs. 4.5-4.7, the strains are corresponding to $F_{11} = F_{22} = 0.98$, $F_{12} = F_{21} = 0$ for compressive strain and $F_{11} = F_{22} = 1.02$, $F_{12} = F_{21} = 0$ for tensile strain. It is shown in Fig. 4.5 that the compressive strain increases the bulk phonon thermal conductivities by about 23% while the tensile strain introduces about 20% decrease in the temperature range we consider here. As temperature increases, strain effect decreases slightly. The phonon thermal conductivities of the

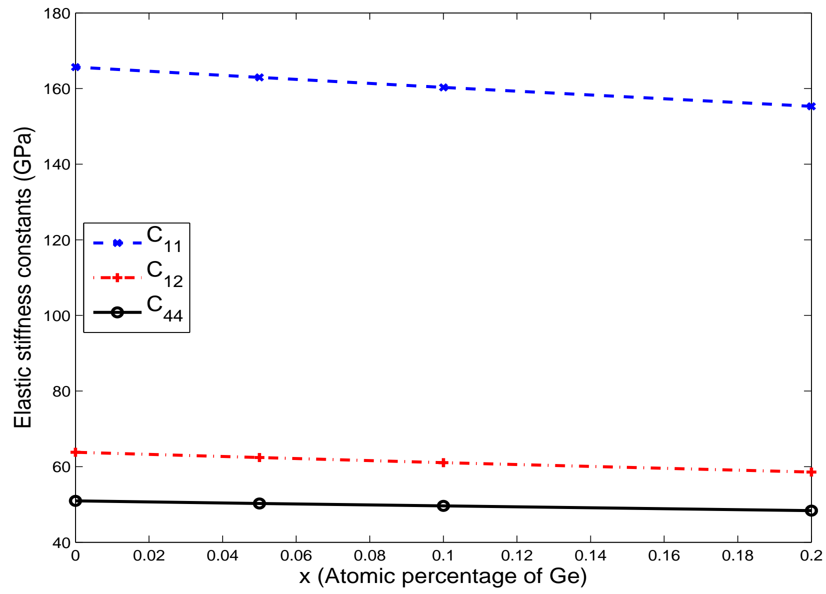

Figure 4.3: Elastic constants of $Si_{1-x}Ge_x$.

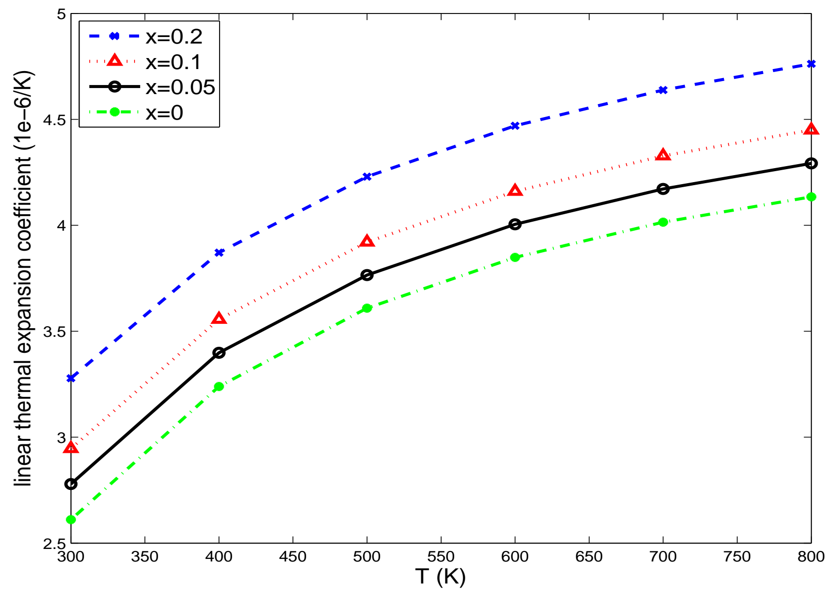

Figure 4.4: Linear thermal expansion coefficient of $Si_{1-x}Ge_x$ between 300-800 K.

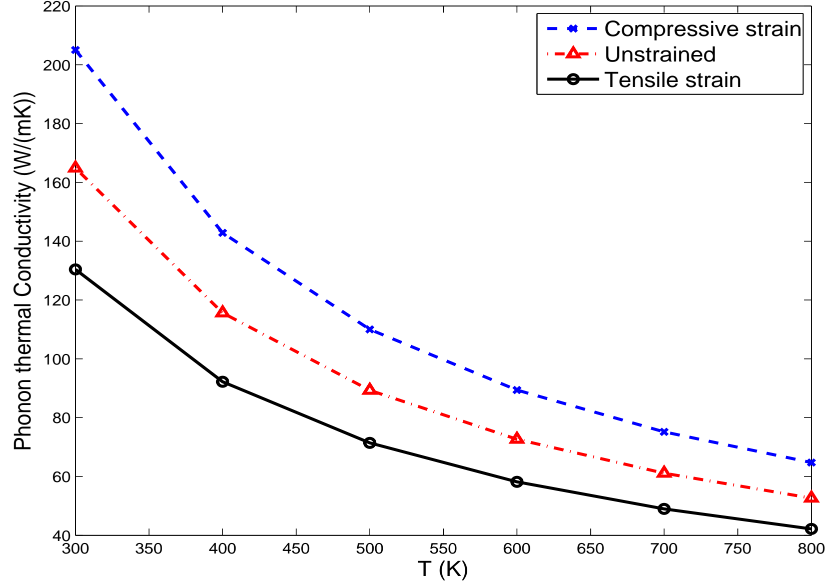

Figure 4.5: Strain and temperature dependent phonon thermal conductivity of bulk Si between 300-800 K.

single crystal Si decrease as temperature increases. Similar behavior is observed in the phonon thermal conductivity of bulk Ge (not shown here).

Figure 4.6 shows the phonon thermal conductivity of a $Si_{0.8}Ge_{0.2}$ nanocomposite calculated from Eq. (2.37) as a function of strain and temperature. In this nanocomposite the embedded Ge nanowires are assumed to have 10 nm $\times$ 10 nm cross-sections. Similar to the bulk Si case, a compressive/tensile strain increases/decreases the phonon thermal conductivity of $Si_{0.8}Ge_{0.2}$ nanocomposite. However, the phonon thermal conductivity variation due to the strains ($<$10%) is much smaller than that in bulk Si. A decrease in the phonon thermal conductivity with increasing temperature is also observed. Once again, the phonon thermal conductivity variation in the $Si_{0.8}Ge_{0.2}$ nanocomposite from 300 K to 800 K is much less than that in the bulk Si, indicating the dominance of interface scattering over the Umklapp scattering.

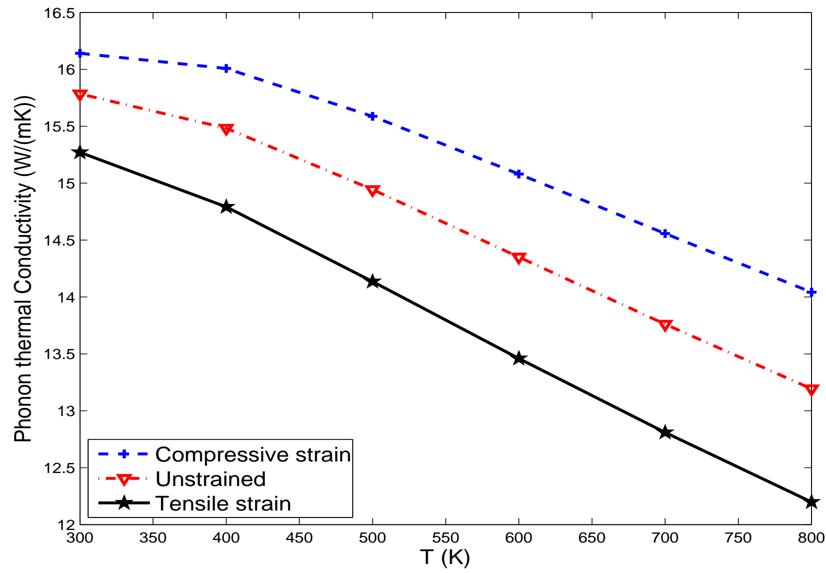

Figure 4.6: Strain and temperature dependent phonon thermal conductivity of $Si_{0.8}Ge_{0.2}$ nanocomposite between 300-800 K.

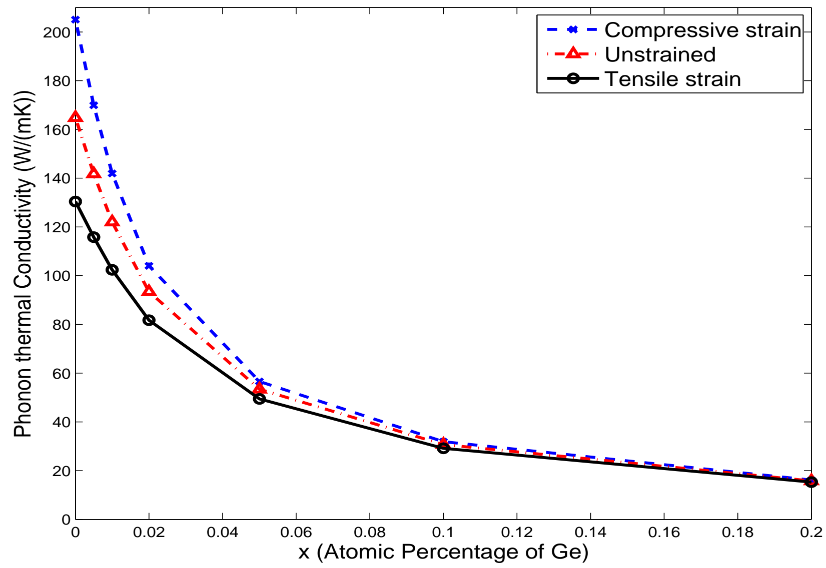

Figure 4.7: Variation of phonon thermal conductivity of $Si_{1-x}Ge_x$ nanocomposites at 300 K with respect to the atomic percentage of Ge.

Next we calculate the phonon thermal conductivity as a function of strain and atomic percentage of Ge. For the rest of this section, we fix the cross-section of the Ge nanowire inclusions to be 10 nm × 10 nm in a unit cell as shown in Fig. 3.7 and adjust the atomic percentage of Ge by varying the size of the unit cell, L_{Si}. Again, $x = 0$ is corresponding to bulk Si. As shown in Fig. 4.7, at 300 K the phonon thermal conductivity decreases quickly with growing atomic percentage of the Ge nanowire. When the interface scattering becomes significant as the volume fraction of Ge increases, the strain effect on the phonon thermal conductivity becomes less obvious.

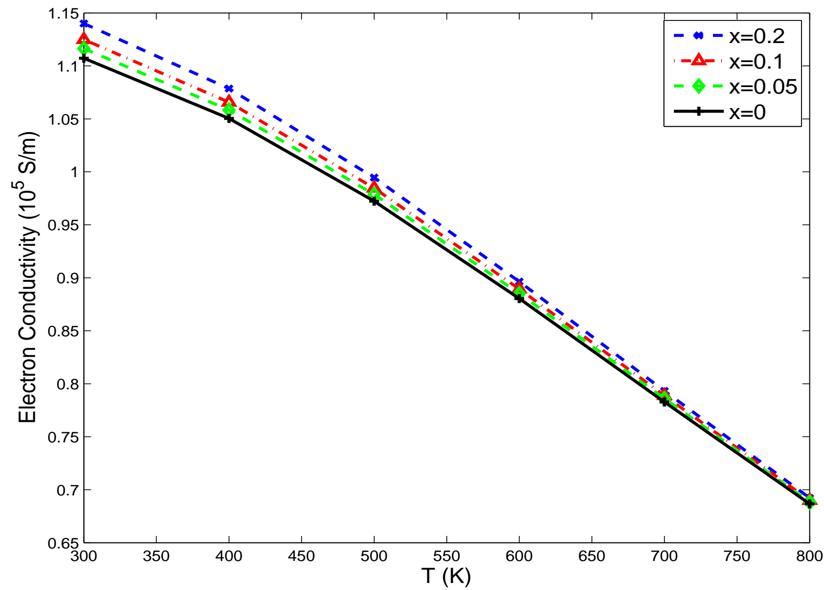

Figure 4.8: Temperature dependent electrical conductivity of $Si_{1-x}Ge_x$ nanocomposites for different atomic percentage of Ge.

Figure 4.8 gives the electrical conductivities of doped bulk Si and $Si_{1-x}Ge_x$ nanocomposites as a function of temperature for different atomic percentage of Ge. The curve with $x = 0$ represents electrical conductivity of doped bulk Si. The electrical conductivity results show that, while electrical conductivity decreases as

temperature increases, the difference between bulk Si and Si/Ge nanocomposites is small, especially at high temperatures. This implies that, in the nanocomposites considered here, grain boundary (interface) scattering of electrons is not significant. From the results shown in Figs. 4.7 and 4.8, it is clear that, due to the large decrease of phonon thermal conductivity in the nanocomposites, the electrical to thermal conductivity ratio of Si/Ge nanocomposites is much higher than that of bulk Si or Ge materials.

4.4.2 Thermal and mechanical performance of TAs

In this section, by using the multi-scale model described in Chap. 4.3, we perform computational analysis of nanocomposite thermal actuators. We consider a V-shaped and a U-shaped nanocomposite TAs. Their geometry parameters shown in Fig. 4.1 are listed in Table 4.1.

4.4.2.1 V-shaped thermal actuator

As shown in Fig. 4.1 (a), the two ends of the V-shaped TA are fixed. The temperature at the two ends is maintained at 300 K. Under a given current going through the TA, the temperature distribution along the length of the V-shaped TA beam is computed. Figure 4.9 shows the variation of temperature distribution with respect to the length of the nanocomposite part, L_c, and the atomic percentage x in $Si_{1-x}Ge_x$ for a current of 27 mA (i.e., current density is $56.25 \times 10^6 A/m^2$ when the thickness of the beam is $30\mu m$). The curve with $L_c = 0$ and $x = 0$ is the temperature distribution when the nanocomposite is not used. In comparison, beams containing Si/Ge nanocomposites obtain higher temperatures with the same input current. It is shown in the figure that there is a rapid temperature increase in the

Table 4.1: Geometry parameters used for the calculation of V-shaped and U-shaped thermal actuators.

Parameters	V-shaped TA	U-shaped TA
L (μm)	600	240
L_1 (μm)		210
L_2 (μm)		9
L_c (μm)	40, 80, 120, 160, 200	20, 40, 80, 120
W (μm)	16	37
w_1 (μm)		4
w_2 (μm)		4
w_3 (μm)		25.5
θ ($degree$)	1	
thickness (μm)	30	20

nanocomposite region. The elevated temperature is maintained with a relatively small variation in the Si region of the beam. Comparing the curves with the same x, it is shown that increasing the length of the nanocomposite part extends the region of rapid temperature increase, resulting a higher temperature in the middle Si region. Comparing the curves with the same L_c, it can be observed in Fig. 4.9 that increasing atomic percentage of Ge in the Si/Ge nanocomposites is equivalent to increasing the rate of temperature change in the nanocomposite region, resulting again a higher temperature in the middle Si region. This is due to the reduction of the phonon thermal conductivity with increasing x, as shown in Fig. 4.7, and thus the increase of electrical to thermal conductivity ratio. From Eq. (4.3), it is obvious that a large temperature increase will give a large actuation displacement. Figure 4.10 shows the tip displacement of the V-shaped TA as a function of L_c and x. Among the

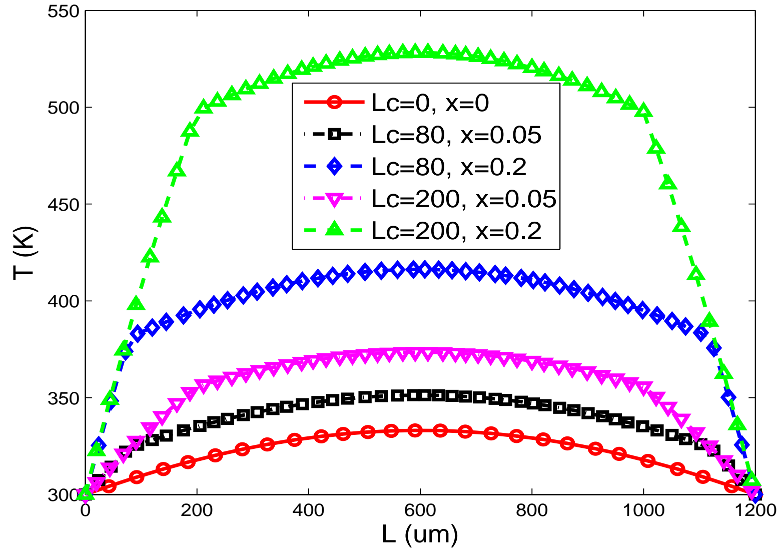

Figure 4.9: Temperature distribution variation of V-shaped thermal actuator with respect to the length of the nanocomposite part and the atomic percentage of Ge in $Si_{1-x}Ge_x$.

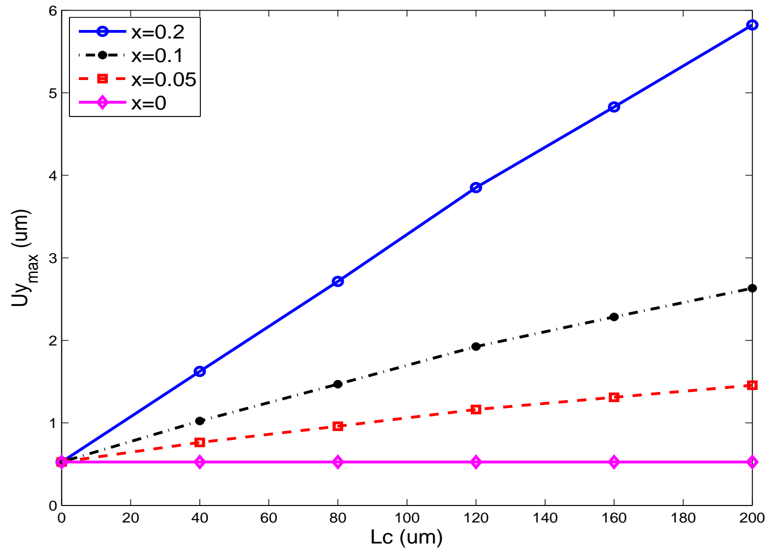

Figure 4.10: Tip displacement of V-shaped thermal actuator as a function of the length of the nanocomposite part and the atomic percentage of Ge in $Si_{1-x}Ge_x$.

results shown in Fig. 4.10, the maximum tip displacement reaches $5.8\mu m$ when the nanocomposite $Si_{0.8}Ge_{0.2}$ with a length $L_c = 200\mu m$ is used. Compared to the tip displacement of $0.53\mu m$ for the pure Si beam, an 10-fold displacement increase is obtained.

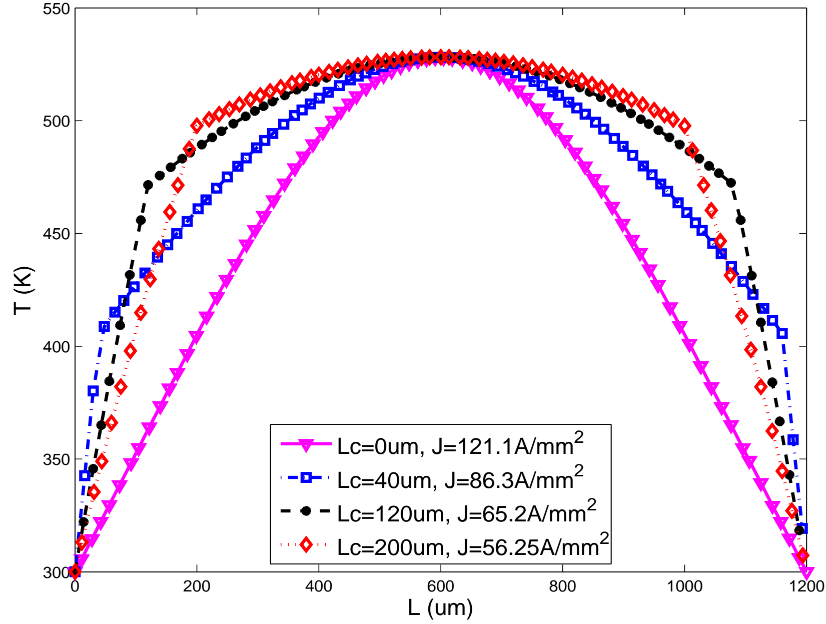

Figure 4.11: Variation in temperature distribution along V-shaped thermal actuator beam with respect to the length of $Si_{0.8}Ge_{0.2}$ nanocomposite.

As discussed previously, a very high temperature may not be desirable in practice. An allowable temperature is typically imposed for the safe operation of the TAs. For this reason, the maximum temperature in the beam is enforced to be 528 K. For different combinations of L_c and x of the $Si_{1-x}Ge_x$ nanocomposites, the input current density is adjusted so that the maximum temperature in the beam is 528 K for all cases. Figs. 4.11 and 4.12 show the temperature distribution and the tip displacement of the TA, respectively, when $Si_{0.8}Ge_{0.2}$ nanocomposite is used. As shown in Fig. 4.11,

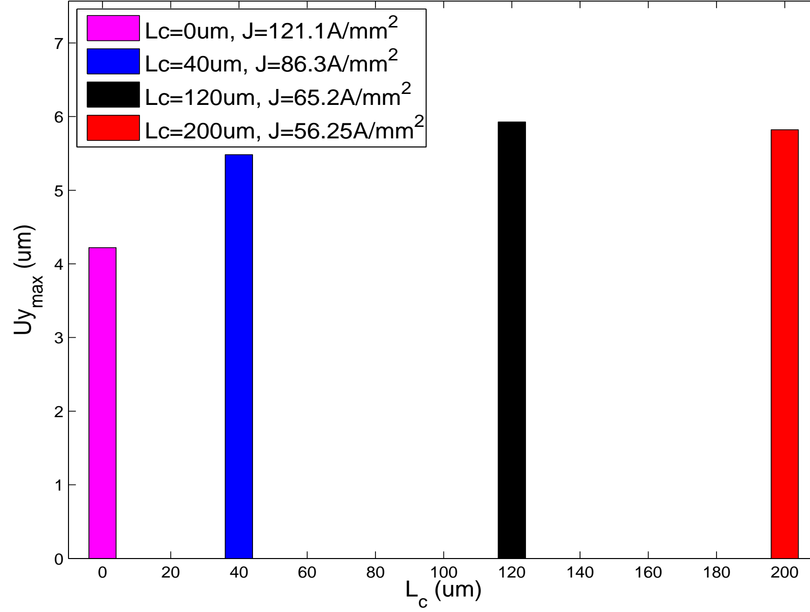

Figure 4.12: Maximum displacement of V-shaped thermal actuator for different length of $Si_{0.8}Ge_{0.2}$ nanocomposite.

when the length of the nanocomposite region, L_c, increases, to keep the maximum temperature the same, the current must be reduced. However, even with a reduced current density the temperature in the Si region still becomes higher for a larger L_c. Note that the current density represents the power consumption in this case. The tip displacements shown in Fig. 4.12 indicate that, compared to the pure Si thermal actuator, the maximum tip displacement is increased by about 40% and the power consumption is decreased by about 50% when the nanocomposite $Si_{0.8}Ge_{0.2}$ with a length $L_c = 200\mu m$ is used.

Next we fix the size of the Si/Ge nanocomposite in the TA beam and investigate the effect of the composition of the nanocomposite material. Figures 4.13 and 4.14 show the temperature distribution and the tip displacement of

the TA for different atomic percentage of Ge in the $Si_{1-x}Ge_x$ nanocomposites. Again, for the same maximum temperature, a larger atomic percentage of Ge gives a larger temperature increase in the beam. A larger tip displacement can be achieved with a smaller power consumption.

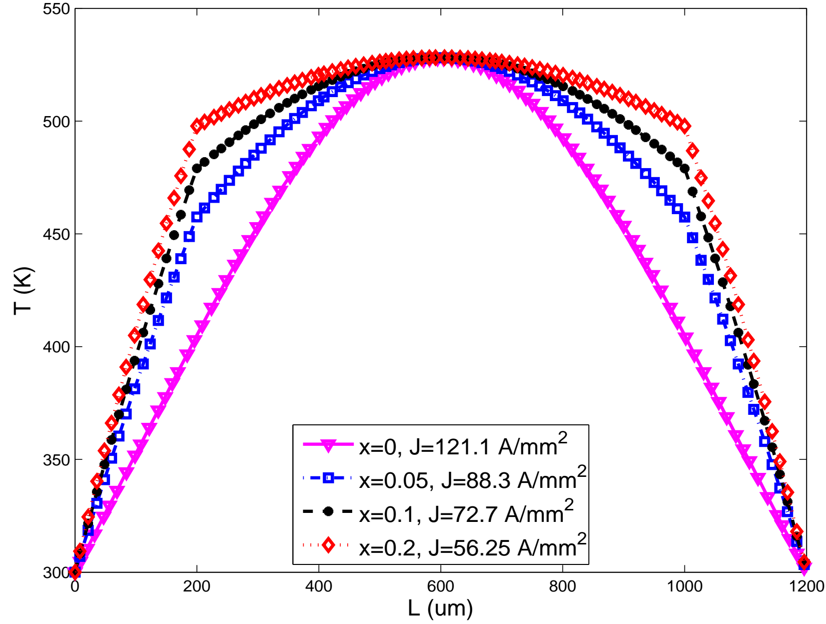

Figure 4.13: Temperature distribution along V-shaped thermal actuator beam for different atomic percentage of Ge in $Si_{1-x}Ge_x$ ($L_c = 200\mu m$).

Figure 4.15 shows the undeformed (black) and deformed (red) beam of V-shaped TAs. The deformation is obtained when the $Si_{0.8}Ge_{0.2}$ nanocomposites with a length of $L_c = 200\mu m$ is used in TA beams with a current of 27 mA passing the beam. In order to make the deformation clear, both x and y direction deformation has been enlarged 50 times. This figure shows that thermal expansion caused by Joule heating generates in-plane deflection in a V-shaped TA and the tip has the largest deformation.

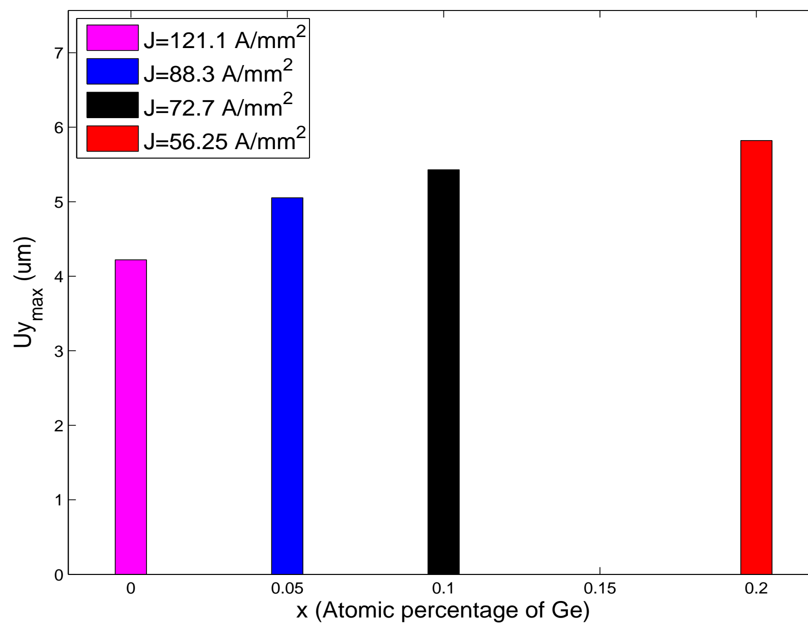

Figure 4.14: Maximum displacement of V-shaped thermal actuator for different atomic percentage of Ge in $Si_{1-x}Ge_x$.

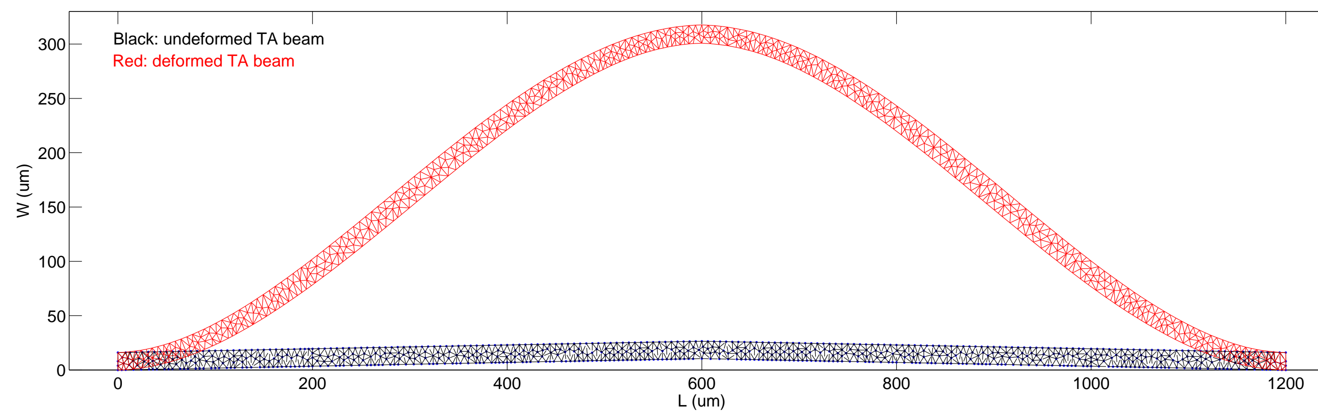

Figure 4.15: Deformed and undeformed beams of V-shaped thermal actuator (deformation has been scaled up by a factor of 50).

4.4.2.2 U-shaped thermal actuator

The performance of Si/Ge nanocomposites in a U-shaped TA (Fig. 4.1 (b)) is also investigated. The two ends of the TA are fixed. The nanocomposite material is placed at the end of the upper (hot) beam. The temperature at the two ends is fixed at 300 K. Figure 4.16 shows the temperature distribution along the hot beam for different L_c and x in $Si_{1-x}Ge_x$ when the current is fixed at 27 mA. Similar to the V-shaped TA, the nanocomposite generates a higher temperature along the hot beam with the same input current. With the atomic percentage of Ge held fixed, a longer nanocomposite region produces a higher temperature along the length of the beam, leading to a larger thermal expansion of the beam. With the length of the nanocomposite region held fixed, a higher atomic percentage of Ge in the Si/Ge nanocomposite also gives a higher temperature along the length of the beam. Note that the kinks in the temperature distributions are due to the difference of the electrical to thermal conductivity ratio between the Si and Si/Ge nanocomposite regions. The large temperature increase shown in Fig. 4.16 translates into a large actuation displacement shown in Fig. 4.17. Note that, for the U-shaped TA, the largest displacement occurs at the lower-right corner of the TA structure. Among the results shown in Fig. 4.17, the maximum displacement reaches $1.7\mu m$ when the nanocomposite $Si_{0.8}Ge_{0.2}$ with a length of $L_c = 120\mu m$ is used. Compared to the maximum displacement of $0.24\mu m$ without using nanocomposites, an 7-fold displacement increase is obtained. In the analysis of U-shaped TA with a fixed maximum temperature, similar behaviors and conclusions are obtained as shown in the V-shaped TA case. For the sake of brevity, the results are not shown here.

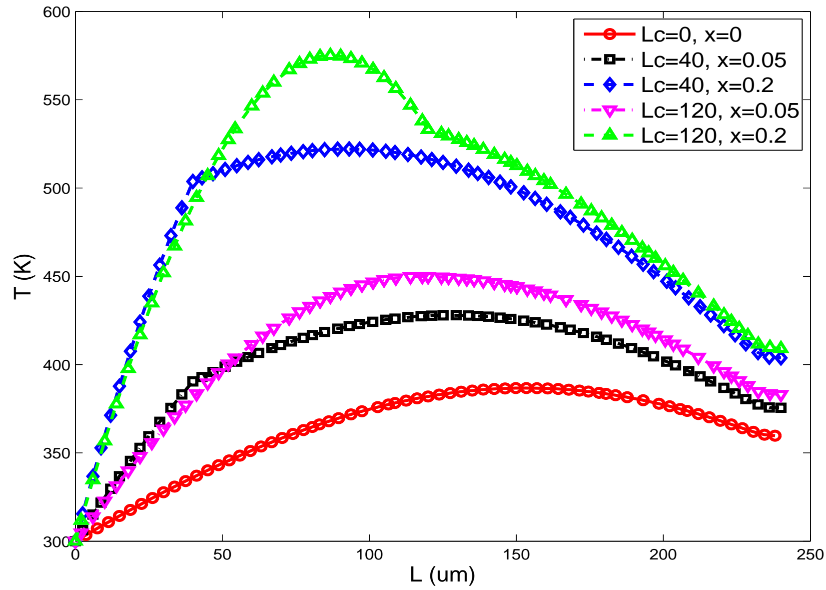

Figure 4.16: Variation of the temperature distribution along the upper beam of U-shaped thermal actuator with the length of Si/Ge nanocomposite and Ge atomic percentage.

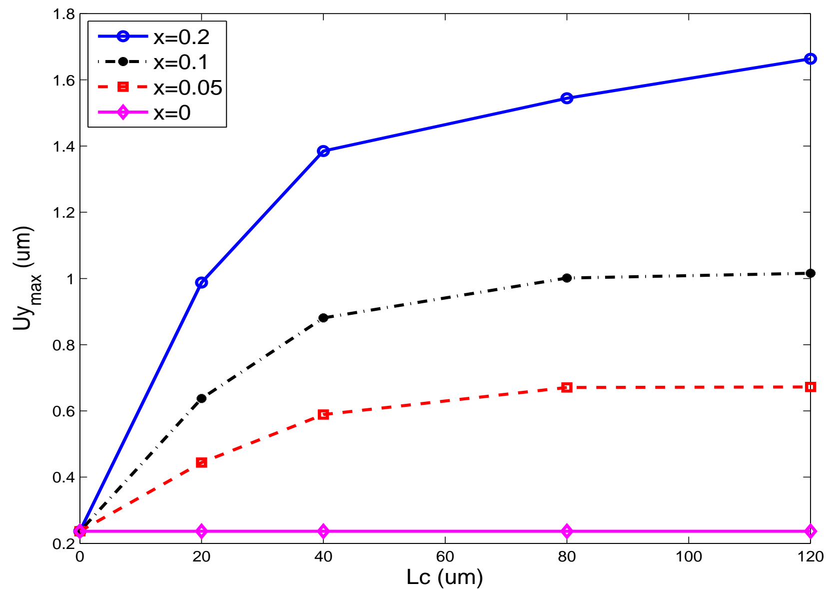

Figure 4.17: Maximum vertical displacement of U-shaped thermal actuator as a function of the length of Si/Ge nanocomposite for different Ge atomic percentages.

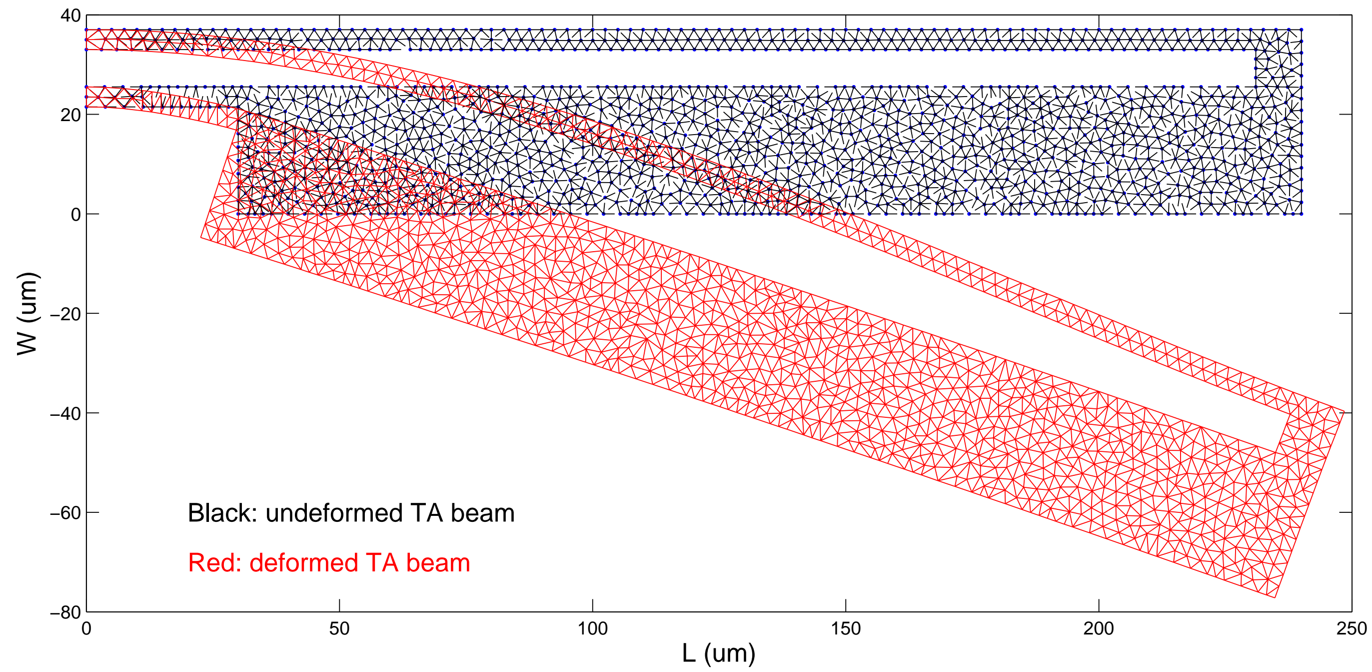

Figure 4.18: Deformed and undeformed beams of U-shaped thermal actuator (deformation has been scaled up by a factor of 50).

Again, the undeformed (black) and deformed (red) beam of U-shaped TAs is shown here in Fig. 4.18. The deformation is obtained when the $Si_{0.8}Ge_{0.2}$ nanocomposites with a length of $L_c = 80\mu m$ is used in U-shaped TA beams with a current of 27 mA passing the beam. Again, to show the deformed shape of the TA clearly, the actual deformation is scaled up by a factor of 50. This figure shows that thermal expansion caused by Joule heating generates in-plane y-direction deflection in a U-shaped TA and the free end has the largest deformation.

4.5 Summary

In this chapter, we introduce a concept of thermal actuation using nanocomposites. To demonstrate the effectiveness of nanocomposite based thermal actuators, we develop a top-down quasicontinuum multi-scale model for computational analysis of the nanocomposite based thermal actuators. Numerical results indicate that incorporating Si/Ge nanocomposites in thermal actuators can significantly increase their energy efficiency and mechanical performance. For a given input current, the Si/Ge nanocomposites can increase the actuation displacement of V-shaped and U-shaped TAs by as much as 10-fold. With a fixed maximum temperature, inclusion of nanocomposites enable the TAs to achieve a larger actuation displacement with less power consumption. In addition, parametric studies show that the size of the nanocomposite region and atomic percentage of the material components have significant effects on the overall performance of the actuators.

CHAPTER 5

CONCLUSIONS

Theoretical and computational models to investigate strain effect on thermal and electron transport properties of Si/Ge nanocomposite materials are developed in this thesis. Based on these models, strain effect on thermoelectric figure of merit of Si/Ge nanocomposite materials and devices is studied. In addition, we propose to use nanocomposites in thermal actuators to enhance their performance and develop a model to analyze the multi-scale, multi-physics problem.

Strain effect on the phonon thermal conductivities in Si/Ge nanocomposites is analyzed by a model combining lattice dynamics and phonon BTE. For a given strain condition, mechanical strain is translated to crystal lattice deformation by using the Cauchy-Born rule. Strain dependent scattering properties of Si and Ge calculated from lattice dynamics with Tersoff empirical interatomic potential are used in BTE to obtain strain dependent effective phonon thermal conductivity of nanocomposites. Ballistic transport within one material and diffuse scattering between Si-Ge interface are employed in BTE, while BTE is numerically solved on an unstructured triangular mesh using the finite volume method. Nanocomposites

with different Si nanowire cross-sections are also investigated. The results show that the phonon thermal conductivity of the nanocomposites can be significantly decreased by a tensile strain, or increased by a compressive strain. With the same length change, hydrostatic strain produces a larger variation in phonon thermal conductivity than uniaxial strain. In addition, it is shown that with the same atomic percentage, the cross-sectional shape makes little difference to the thermal conductivity except at very small characteristic lengths of the Si nanowire.

The strain effect on electrical properties of the Si/Ge nanocomposites are modeled by an analytical model derived from the BTE under the relaxation-time approximation with strain induced energy shift and effective mass variation calculated from deformation potential theory and $\mathbf{k} \cdot \mathbf{p}$ method. Based on the above two models, strain effect on figure of merit is investigated in n-type Ge wire-Si host nanocomposite materials. Our calculations show that uniaxial tensile strain along $\langle 100 \rangle$ direction enhances dimensionless figure of merit in the tension direction in the 300-800 K temperature range, while biaxial tensile strain along [100] and [010] directions decreases it parallel to tensions at low temperatures and increases it at high temperatures. Numerical results indicate that dimensionless figure of merit is decreased by shear strain, compressive uniaxial strain and compressive biaxial strain. When electron concentration is $10^{19} cm^{-3}$, 1% uniaxial tensile strain increases the dimensionless figure of merit of $Si_{0.8}Ge_{0.2}$ nanocomposites by 14% at 800 K.

Due to the large reduction of thermal conductivity and small electrical conductivity variation in nanocomposites, we propose to use nanocomposites in micro thermal actuators to allow a higher temperature increase in a large region of the actuator beams, leading to significantly increased actuation distance. A multi-scale, multi-physics model is developed to simulate the thermo-mechanical

response of nanocomposite based thermal actuators. In the multi-scale model, the thermo-mechanical response of the actuator due to Joule heating is modeled using classical continuum theories, while the thermal and electrical properties of doped Si and Si/Ge nanocomposite materials are obtained from atomistic level descriptions. An iterative procedure is carried out between the calculations at the two length scales until a self-consistent solution is obtained. Numerical results reveal that thermal actuators' energy efficiency and mechanical performance can be significantly improved by incorporating Si/Ge nanocomposites in them. In addition, parametric studies indicate that the overall performance of the actuators is significantly affected by the size of the nanocomposite region and atomic percentage of the material components.

BIBLIOGRAPHY

[1] Y. Xia, P. Yang, Y. Sun, Y. Wu, B. Mayers, B. Gates, Y. Yin, F. Kim, and H. Yan. One-dimensional nanostructures: Synthesis, characterization, and applications. *Advanced Materials*, 15(5):353–389, 2003.

[2] A. S. Arico, P. Bruce, B. Scrosati, J.-M. Tarascon, and W. V. Schalkwijk. Nanostructured materials for advanced energy conversion and storage devices. *Nature Materials*, 4:366–377, 2005.

[3] R. J. Gehr and R. W. Boyd. Optical properties of nanostructured optical materials. *Chemistry of Materials*, 8(8):1807–1819, 1996.

[4] P. T. Hammond. Form and function in multilayer assembly: New applications at the nanoscale. *Advanced Materials*, 16(15):1271–1293, 2004.

[5] G. Joshi, H. Lee, Y. Lan, X. Wang, G. Zhu, D. Wang, R. W. Gould, D. C. Cuff, M. Y. Tang, M. S. Dresselhaus, G. Chen, and Z. Ren. Enhanced thermoelectric figure-of-merit in nanostructured p-type silicon germanium bulk alloys. *Nano Letters*, 8(12):4670–4674, 2008.

[6] E. T. Thostenson, C. Li, and T.-W. Chou. Nanocomposites in context. *Composites Science and Technology*, 65(3-4):491–516, 2005.

[7] Z.-M. Dang, B. Xia, S.-H Yao, M.-J. Jiang, H.-T. Song, L.-Q. Zhang, and D. Xie. High-dielectric-permittivity high-elasticity three-component nanocomposites with low percolation threshold and low dielectric loss. *Applied Physics Letters*, 94(4):042902, 2009.

[8] S. Rezanejad and M. Kokabi. Shape memory and mechanical properties of cross-linked polyethylene/clay nanocomposites. *European Polymer Journal*, 43(7):2856–2865, 2007.

[9] R. Yang and G. Chen. Thermal conductivity modeling of periodic two-dimensional nanocomposites. *Physical Review B*, 69:195316, 2004.

[10] A. Haque, M. Shamsuzzoha, F. Hussain, and D. Dean. S2-glass/epoxy polymer nanocomposites: Manufacturing, structures, thermal and mechanical properties. *Journal of Composite Materials*, 37(20):1821–1837, 2003.

[11] I.-H. Kim and Y. G. Jeong. Polylactide/exfoliated graphite nanocomposites with enhanced thermal stability, mechanical modulus, and electrical conductivity. *Journal of Polymer Science Part B: Polymer Physics*, 48(8):850858, 2010.

[12] B. Poudel, Q. Hao, Y. Ma, Y. Lan, A. Minnich, B. Yu, X. Yan, D. Wang, A. Muto, D. Vashaee, X. Chen, J. Liu, M. S. Dresselhaus, G. Chen, and Z. Ren. High-thermoelectric performance of nanostructured bismuth antimony telluride bulk alloys. *Science*, 320(5876):634–638, 2008.

[13] F. Hussain, M. Hojjati, M. Okamoto, and R. E. Gorga. Review article: Polymer-matrix nanocomposites, processing, manufacturing, and application: An overview. *Journal of Composite Materials*, 40(17):1511–1575, 2006.

[14] R. A. Hule and D. J. Pochan. Polymers nanocomposites for biomedical applications. *MRS Bulletin*, 32:354–358, 2007.

[15] M. Song, C. Pan, C. Chen, J. Li, X. Wang, and Z. Gu. The application of new nanocomposites: Enhancement effect of polylactide nanofibers/nano-TiO_2 blends on biorecognition of anticancer drug daunorubicin. *Applied Surface Science*, 255(2):610–612, 2008.

[16] C. Li, E. T. Thostenson, and T.-W. Chou. Sensors and actuators based on carbon nanotubes and their composites: A review. *Composites Science and Technology*, 68(6):1227–1249, 2008.

[17] W. Xie, J. He, H. J. Kang, X. Tang, S. Zhu, M. Laver, S. Wang, J. R. D. Copley, C. M. Brown, Q. Zhang, and T. M. Tritt. Identifying the specific nanostructures responsible for the high thermoelectric performance of $(Bi,Sb)_2Te_3$ nanocomposites. *Nano Letters*, 10(9):3283–3289, 2010.

[18] Y.-H. Yun, V. Shanov, M. J. Schulz, S. Narasimhadevara, S. Subramaniam, D. Hurd, and F. J. Boerio. Development of novel single-wall carbon nanotube-epoxy composite ply actuators. *Smart Materials and Structures*, 14(6):1526, 2005.

[19] *http://www.scorec.rpi.edu/MSEN/.*

[20] *http://saturn.jpl.nasa.gov/photos/imagedetails/index.cfm?imageId=1943.*

[21] *http://www.greencar.com/articles/waste-exhaust-heat-generates-electricity-cars-efficient.php.*

[22] W. A. Wong, D. J. Anderson, K. L. Tuttle, and R. C. Tew. Status of NASA's advanced radioisotope power conversion technology research and development. *AIP Conference Proceedings*, 813(1):340–347, 2006.

[23] E. F. Thacher, B. T. Helenbrook, M. A. Karri, and C. J. Richter. Testing of an automobile exhaust thermoelectric generator in a light truck. In *Proceedings of the Institution of Mechanical Engineers, Part D: Journal of Automobile Engineering*, volume 221, 2007.

[24] G. Mahan, B. Sales, and J. Sharp. Thermoelectric materials: New approaches to an old problem. *Physics Today*, 50(3):42–47, 1997.

[25] F. J. DiSalvo. Thermoelectric cooling and power generation. *Science*, 285(5428):703–706, 1999.

[26] L. E. Bell. Cooling, heating, generating power, and recovering waste heat with thermoelectric systems. *Science*, 321(5895):1457–1461, 2008.

[27] H. J. Goldsmid. *Thermoelectric Refrigeration*. Plenum Press, New York, 1964.

[28] G. Chen, M. S. Dresselhaus, G. Dresselhaus, J.-P. Fleurial, and T. Caillat. Recent developments in thermoelectric materials. *International Materials Reviews*, 48(1):45–66, 2003.

[29] R. Venkatasubramanian. Phonon blocking electron transmitting superlattice structures as advanced thin film thermoelectric materials. *Semiconductors and Semimetals*, 71:175–201, 2001.

[30] G. Chen and A. Shakouri. Heat transfer in nanostructures for solid-state energy conversion. *Journal of Heat Transfer*, 124(2):242–252, 2002.

[31] R. Venkatasubramanian, E. Siivola, T. Colpitts, and B. O'Quinn. Thin-film thermoelectric devices with high room-temperature figures of merit. *Nature*, 413(6856):597–602, 2001.

[32] B. Zhang, J. He, X. Ji, T. M. Tritt, and A. Kumbhar. Controlled two-dimensional coated nanostructures for bulk thermoelectric composites. *Applied Physics Letters*, 89(16):163114, 2006.

[33] R. Hickey, M. Kujath, and T. Hubbard. Heat transfer analysis and optimization of two-beam microelectromechanical thermal actuators. *Journal of Vacuum Science Technology*, 20:971–974, 2002.

[34] M. S. Baker, R. A. Plass, T. J. Headley, and J. A. Walraven. Final report: Compliant thermo-mechanical MEMS actuators LDRD #52553, SAND2004-6635. Technical report, Sandia National Laboratories, Albuquerque, NM, 2004.

[35] W. P. Sassen, V. A. Henneken, M. Tichem, and P. M. Sarro. Contoured thermal V-beam actuator with improved temperature uniformity. *Sensors and Actuators, A: Physical*, 144(2):341–347, 2008.

[36] A. R. Abramson, C.-L. Tien, and A. Majumdar. Interface and strain effects on the thermal conductivity of heterostructures: A Molecular Dynamics study. *Journal of Heat Transfer*, 124(5):963–970, 2002.

[37] D. A. Broido, M. Malorny, G. Birner, N. Mingo, and D. A. Stewart. Intrinsic lattice thermal conductivity of semiconductors from first principles. *Applied Physics Letters*, 91(23):231922, 2007.

[38] W. Zhang, T. S. Fisher, and N. Mingo. The atomistic Green's function method: An efficient simulation approach for nanoscale phonon transport. *Numerical Heat Transfer, Part B: Fundamentals*, 51(4):333–349, 2007.

[39] K.-M. Lee, T. Weissgarber, and B. Kieback. Microstructural and chemical properties of AlN-Cu nanocomposite powders prepared by planetary ball milling. *Journal of Materials Science*, 39(16-17):5235–5238, 2004.

[40] Y. Yang, M. C. Gupta, J. N. Zalameda, and W. P. Winfree. Dispersion behaviour, thermal and electrical conductivities of carbon nanotube-polystyrene nanocomposites. *Micro and Nano Letters*, 3(2):35–40, 2008.

[41] R. W. Keyes and R. J. Sladek. Piezo-thermal conductivity effect in germanium. *Physical Review*, 125(2):478–483, 1962.

[42] L. J. Challis and S. C. Haseler. The effect of uniaxial stress on the thermal conductivity of p-Ge. *Journal of Physics C: Solid State Physics*, 11(23):4681–4694, 1978.

[43] A. Ramdane, B. Salce, and L. J. Challis. Stress dependence of the thermal conductivity of Cr-doped GaAs. *Physical Review B*, 27(4):2554–2557, 1983.

[44] K. C. Sood and M. K. Roy. Phonon conductivity of doped germanium under uniaxial stress in the [110] direction. *Physical Review B*, 46(12):7486–7495, 1992.

[45] T. Borca-Tasciuc, W. Liu, J. Liu, T. Zeng, D. W. Song, C. D. Moore, G. Chen, K. L. Wang, M. S. Goorsky, T. Radetic, R. Gronsky, T. Koga, and M. S. Dresselhaus. Thermal conductivity of symmetrically strained Si/Ge superlattices. *Superlattices and Microstructures*, 28(3):199–206, 2000.

[46] R. C. Picu, T. Borca-Tasciuc, and M. C. Pavel. Strain and size effects on heat transport in nanostructures. *Journal of Applied Physics*, 93(6):3535–3539, 2003.

[47] J. M. Ziman. *Electrons and Phonons*. Oxford University Press, 1960.

[48] S. V. J. Narumanchi, J. Y. Murthy, and C. H. Amon. Boltzmann transport equation-based thermal modeling approaches for hotspots in microelectronics. *Heat and Mass Transfer*, 42(6):478–491, 2006.

[49] J. Tersoff. Empirical interatomic potential for silicon with improved elastic properties. *Physical Review B*, 38(14):9902–9905, 1988.

[50] D. W. Brenner. Empirical potential for hydrocarbons for use in simulating the chemical vapor deposition of diamond films. *Physical Review B*, 42(15):9458–9471, 1990.

[51] F. H. Stillinger and T. A. Weber. Computer simulation of local order in condensed phases of silicon. *Physical Review B*, 31(8):5262–5271, 1985.

[52] J. Tersoff. Modeling solid-state chemistry: interatomic potentials for multicomponent systems. *Physical Review B*, 39(8):5566–5568, 1989.

[53] H. Zhao, Z. Tang, G. Li, and N. R. Aluru. Quasiharmonic models for the calculation of thermodynamic properties of crystalline silicon under strain. *Journal of Applied Physics*, 99(6):064314, 2006.

[54] M. Born and K. Huang. *Dynamical theory of crystal lattices*. Clarendon Press, Oxford, 1954.

[55] G. A. Slack. The thermal conductivity of nonmetallic crystals. *Solid State Physics*, 34:1–71, 1979.

[56] B. L. Huang and M. Kaviany. Structural metrics of high-temperature lattice conductivity. *Journal of Applied Physics*, 100(12):123507, 2006.

[57] G. Chen. Thermal conductivity and ballistic-phonon transport in the cross-plane direction of superlattices. *Physical Review B*, 57(23):14958–14973, 1998.

[58] G. Chen. Size and interface effects on thermal conductivity of superlattices and periodic thin-film structures. *Journal of Heat Transfer*, 119(2):220–229, 1997.

[59] A. Majumdar. Microscale heat conduction in dielectric thin films. *Journal of Heat Transfer*, 115(1):7–16, 1993.

[60] G. Chen. Nonlocal and nonequilibrium heat conduction in the vicinity of nanoparticles. *Journal of Heat Transfer*, 118(3):539–545, 1996.

[61] G. D. Raithby. Discussion of the finite-volume method for radiation, and its application using 3D unstructured meshes. *Numerical Heat Transfer, Part B: Fundamentals*, 35:389–405, 1999.

[62] E. H. Chui, G. D. Raithby, and P. M. J. Hughes. Prediction of radiative transfer in cylindrical enclosures with the finite volume method. *Journal of Thermophysics and Heat Transfer*, 6(4):605–611, 1992.

[63] M. Y. Kim, S. W. Baek, and J. H. Park. Unstructured finite-volume method for radiative heat transfer in a complex two-dimensional geometry with obstacles. *Numerical Heat Transfer, Part B: Fundamentals*, 39(6):617–635, 2001.

[64] J. Y. Murthy and S. R. Mathur. Finite volume method for radiative heat transfer using unstructured meshes. *Journal of Thermophysics and Heat Transfer*, 12:313–321, 1998.

[65] J. C. Chai, H. S. Lee, and S. V. Patankar. Finite volume method for radiation heat transfer. *Journal of Thermophysics and Heat Transfer*, 8(3):419–425, 1994.

[66] S. V. J. Narumanchi, J. Y. Murthy, and C. H. Amon. Submicron heat transport model in silicon accounting for phonon dispersion and polarization. *Journal of Heat Transfer*, 126(6):946–955, 2004.

[67] S. W. Baek, M. Y. Kim, and J. S. Kim. Nonorthogonal finite-volume solutions of radiative heat transfer in a three-dimensional enclosure. *Numerical Heat Transfer, Part B: Fundamentals*, 34(4):419–437, 1998.

[68] D. Baillis and J. Randrianalisoa. Prediction of thermal conductivity of nanostructures: Influence of phonon dispersion approximation. *International Journal of Heat and Mass Transfer*, 52(11-12):2516–2527, 2009.

[69] J. Zou and A. Balandin. Phonon heat conduction in a semiconductor nanowire. *Journal of Applied Physics*, 89(5):2932–2938, 2001.

[70] P. Flubacher, A. J. Leadbetter, and J. A. Morrison. The heat capacity of pure silicon and germanium and properties of their vibrational frequency spectra. *Philosophical Magazine*, 4(39):273–294, 1959.

[71] C. Kittel. *Introduction to Solid State Physics*. Wiley, 2005.

[72] L. J. Porter, S. Yip, M. Yamaguchi, H. Kaburaki, and M. Tang. Empirical bond-order potential description of thermodynamic properties of crystalline silicon. *Journal of Applied Physics*, 81(1):96–106, 1997.

[73] P. Chantrenne, J. L. Barrat, X. Blase, and J. D. Gale. An analytical model for the thermal conductivity of silicon nanostructures. *Journal of Applied Physics*, 97(10):104318, 2005.

[74] C. J. Glassbrenner and G. A. Slack. Thermal conductivity of silicon and germanium from 3°K to the melting point. *Physical Review*, 134(4A):A1058–A1069, 1964.

[75] L. J. Porter, J. F. Justo, and S. Yip. The importance of Grüneisen parameters in developing interatomic potentials. *Journal of Applied Physics*, 82(11):5378–5381, 1997.

[76] V. M. Glazov, A. S. Pashinkin, and M. S. Mikhailova. Heat capacity of silicon in the range 350-770 K. *Scandinavian Journal of Metallurgy*, 30:388–390, 2001.

[77] D. A. Wright. Thermoelectric properties of bismuth telluride and its alloys. *Nature*, 181:834, 1958.

[78] X. W. Wang, H. Lee, Y. C. Lan, G. H. Zhu, G. Joshi, D. Z. Wang, J. Yang, A. J. Muto, M. Y. Tang, J. Klatsky, S. Song, M. S. Dresselhaus, G. Chen, and Z. F. Ren. Enhanced thermoelectric figure of merit in nanostructured n-type silicon germanium bulk alloy. *Applied Physics Letters*, 93(19):193121, 2008.

[79] Y. Xu and G. Li. Strain effect analysis on phonon thermal conductivity of two-dimensional nanocomposites. *Journal of Applied Physics*, 106(11):114302, 2009.

[80] M. Chu, Y. Sun, U. Aghoram, and S. E. Thompson. Strain: A solution for higher carrier mobility in nanoscale MOSFETs. *Annual Review of Materials Research*, 39(1):203–229, 2009.

[81] Y. Sun, S. E. Thompson, and T. Nishida. *Strain Effect in Semiconductors: Theory and Device Applications*. Springer Science+Business Media, LLC, 2010.

[82] A. J. Minnich, H. Lee, X. W. Wang, G. Joshi, M. S. Dresselhaus, Z. F. Ren, G. Chen, and D. Vashaee. Modeling study of thermoelectric SiGe nanocomposites. *Physical Review B*, 80(15):155327, 2009.

[83] T. Vogelsang and K. R. Hofmann. Electron mobilities and high-field drift velocities in strained silicon on silicon-germanium substrates. *IEEE Transactions on Electron Devices*, 39(11):2641–2642, 1992.

[84] T. Vogelsang and K. R. Hofmann. Electron transport in strained Si layers on $Si_{1-x}Ge_x$ substrates. *Applied Physics Letters*, 63(2):186–188, 1993.

[85] N. W. Ashcroft and N. D. Mermin. *Solid State Physics*. Brooks/Cole, 1976.

[86] M. E. Levinshtein, S. L. Rumyantsev, and M. S. Shur, editors. *Properties of advanced semiconductor materials: GaN, AlN, InN, BN, SiC, SiGe*, chapter 6, pages 149–187. John Wiley & Sons, Ltd., 2001.

[87] M. M. Rieger and P. Vogl. Electronic-band parameters in strained $Si_{1-x}Ge_x$ alloys on $Si_{1-y}Ge_y$ substrates. *Physical Review B*, 48:14276–14287, 1993.

[88] I. Balslev. Influence of uniaxial stress on the indirect absorption edge in silicon and germanium. *Physical Review*, 143(2):636–647, 1966.

[89] I. Goroff and L. Kleinman. Deformation potentials in silicon. III. effects of a general strain on conduction and valence levels. *Physical Review*, 132(3):1080–1084, 1963.

[90] E. Ungersboeck, S. Dhar, G. Karlowatz, V. Sverdlov, H. Kosina, and S. Selberherr. The effect of general strain on the band strucutre and electron mobility of silicon. *IEEE Transactions on Electron Devices*, 54:2183–2190, 2007.

[91] K. Uchida, T. Krishnamohan, K.C. Saraswat, and Y. Nishi. Physical mechanisms of electron mobility enhancement in uniaxial stressed MOSFETs and impact of uniaxial stress engineering in ballistic regime. In *2005 IEEE International Electron Devices Meeting*, pages 129 –132, dec. 2005.

[92] V. Sverdlov, E. Ungersboeck, H. Kosina, and S. Selberherr. Effects of shear strain on the conduction band in silicon: An efficient two-band k · p theory. In *2007 IEEE 37th European Solid State Device Research Conference*, pages 386 –389, sept. 2007.

[93] V. Sverdlov, T. Windbacher, and S. Selberherr. Mobility enhancement in thin silicon films: Strain and thickness dependences of the effective masses and non-parabolicity parameter. In *2008 IEEE Simulation of Semiconductor Processes and Devices*, pages 145 –148, sept. 2008.

[94] G. Chen. *Nanoscale energy transport and conversion: a parallel treatment of electrons, molecules, phonons, and photons*. Oxford University Press, 2005.

[95] A. Minnich. Modeling the thermoelectric properties of bulk and nanocomposite thermoelectric materials. Master thesis, Massachusetts Institute of Technology. Department of Mechanical Engineering., 2008.

[96] Y. I. Ravich, B. A. Efimova, and V. I. Tamarchenko. Scattering of current carriers and transport phenomena in lead chalcogenides. *Physica Status Solidi (B): Basic Solid State Physics*, 43:11–33, 1971.

[97] M. Lundstrom. *Fundamentals of Carrier Transport*. Cambridge University Press, Cambridge, UK, 2000.

[98] W. Zawadzki and W. Szymańska. Elastic electron scattering in InSb-type semiconductors. *Physica Status Solidi (B)*, 45:415–432, 1971.

[99] A. Rahman, M. S. Lundstrom, and A. W. Ghosh. Generalized effective-mass approach for n-type metal-oxide-semiconductor field-effect transistors on arbitrarily oriented wafers. *Journal of Applied Physics*, 97(5):053702, 2005.

[100] J. P. Dismukes, L. Ekstrom, E. F. Steigmeier, I. Kudman, and D. S. Beers. Thermal and electrical properties of heavily doped Ge-Si alloys up to 1300°K. *Journal of Applied Physics*, 35(10):2899–2907, 1964.

[101] M. Wagner. *Simulation of Thermoelectric Devices*. PhD thesis, Vienna University of Technology, 2007.

[102] J. H. Comtois and V. M. Bright. Applications for surface-micromachined polysilicon thermal actuators and arrays. *Sensors and Actuators, A: Physical*, 58:19–25, 1997.

[103] L. Que, J.-S. Park, and Y. B. Gianchandani. Bent-beam electrothermal actuators-part I: Single beam and cascaded devices. *Journal of Microelectromechanical Systems*, 10(2):247–254, 2001.

[104] Q.-A. Huang and N. K. S. Lee. Analysis and design of polysilicon thermal flexure actuator. *Journal of Micromechanics and Microengineering*, 9(1):64–70, 1999.

[105] O. Sigmund. Design of multiphysics actuators using topology optimization. *Computer Methods in Applied Mechanics and Engineering*, 190:6577–6627, 2001.

[106] D. Yan, A. Khajepour, and R. Mansour. Design and modeling of a MEMS bidirectional vertical thermal actuator. *Journal of Micromechanics and Microengineering*, 14(7):841, 2004.

[107] S. C. Chen and M. L. Culpepper. Design of contoured microscale thermomechanical actuators. *Journal of Microelectromechanical Systems*, 15(5):1226–1234, 2006.

[108] N. D. Mankame and G. K. Ananthasuresh. Comprehensive thermal modelling and characterization of an electro-thermal-compliant microactuator. *Journal of Micromechanics and Microengineering*, 11(5):452, 2001.

[109] Z. Tang, H. Zhao, G. Li, and N. R. Aluru. Finite-temperature quasicontinuum method for multiscale analysis of silicon nanostructures. *Physical Review B*, 74(6):064110, 2006.

[110] H. Guckel, J . Klein, T. Christenson, K. Skrobis, M . Laudon, and E. G. Lovell. Thermo-magnetic metal flexure actuators. In *5th Technical Digest., IEEE Solid-State Sensor and Actuator Workshop*, pages 73–75, 1992.

[111] Z. Hashin and S. Shtrikman. A variational approach to the theory of the elastic behaviour of multiphase materials. *Journal of the Mechanics and Physics of Solids*, 11(2):127–140, 1963.

[112] R. Hill. Theory of mechanical properties of fibre-strengthened materials–III. self-consistent model. *Journal of the Mechanics and Physics of Solids*, 13(4):189–198, 1965.

[113] L. J. Walpole. On the overall elastic moduli of composite materials. *Journal of the Mechanics and Physics of Solids*, 17(4):235–251, 1969.

[114] T. Mori and K. Tanaka. Average stress in matrix and average elastic energy of materials with misfitting inclusions. *Acta Metallurgica*, 21(5):571–574, 1973.

[115] T. Chen, G. J. Dvorak, and Y. Benveniste. Mori-Tanaka estimates of the overall elastic moduli of certain composite materials. *Journal of Applied Mechanics*, 59(3):539–546, 1992.

[116] Y. Benveniste, G. J. Dvorak, and T. Chen. On diagonal and elastic symmetry of the approximate effective stiffness tensor of heterogeneous media. *Journal of the Mechanics and Physics of Solids*, 39(7):927–946, 1991.

[117] G. J. Dvorak and Y. Benveniste. On transformation strains and uniform fields in multiphase elastic media. *Proceedings of the Royal Society of London, Series A: Mathematical and Physical Sciences*, 437(1900):291–310, 1992.

[118] T. Reiter, G. J. Dvorak, and V. Tvergaard. Micromechanical models for graded composite materials. *Journal of the Mechanics and Physics of Solids*, 45(8):1281–1302, 1997.

[119] R. Hill. Theory of mechanical properties of fibre-strengthened materials: I. elastic behaviour. *Journal of the Mechanics and Physics of Solids*, 12(4):199–212, 1964.

[120] J. J. Wortman and R. A. Evans. Young's modulus, shear modulus, and poisson's ratio in silicon and germanium. *Journal of Applied Physics*, 36:153–156, 1965.

[121] N. Ono, K. Kitamura, K. Nakajima, and Y. Shimanuki. Measurement of Young's modulus of silicon single crystal at high temperature and its dependency on boron concentration using the flexural vibration method. *Japanese Journal of Applied Physics*, 39(Part 1, No. 2A):368–371, 2000.

[122] J. R. Gladden, G. Li, R. Adebisi, S. Firdosy, T. Caillat, and V. Ravi. High-temperature elastic moduli of bulk nanostructured n- and p-type silicon germanium. *Physical Review B*, 82(4):045209, 2010.

[123] T. Reiter and G. J. Dvorak. Micromechanical models for graded composite materials: II. thermomechanical loading. *Journal of the Mechanics and Physics of Solids*, 46(9):1655–1673, 1998.

[124] G. A. Slack and S. F. Bartram. Thermal expansion of some diamondlike crystals. *Journal of Applied Physics*, 46(1):89–98, 1975.

[125] Y. Okada and Y. Tokumaru. Precise determination of lattice parameter and thermal expansion coefficient of silicon between 300 and 1500 K. *Journal of Applied Physics*, 56(2):314–320, 1984.

[126] R. R. Reeber and K. Wang. Thermal expansion and lattice parameters of group IV semiconductors. *Materials Chemistry and Physics*, 46(2-3):259–264, 1996.